

Parameter optimization for Dynamic Line Scan Thermography.

Thesis submitted in fulfilment of the requirements for the degree of Doctor in Applied Engineering (Doctor in de Toegepaste Ingenieurswetenschappen) at the University of Antwerp.

Ing. Simon Verspeek



University of Antwerp

Supervisors
Prof. dr. G. Steenackers
Prof. dr. X. Maldague

Antwerpen, 2023

Faculty of Applied Engineering
Electromechanics

Parameter optimization for Dynamic Line Scan Thermography.

Thesis submitted in fulfilment of the requirements for the degree of
Doctor in Applied Engineering (Doctor in de Toegepaste
Ingenieurswetenschappen)
at the University of Antwerp.

Ing. Simon Verspeek

Antwerpen, 2023

Supervisors
Prof. dr. G. Steenackers
Prof. dr. X. Maldague

Jury

Chairman

Prof. dr. S. De Rammelaere, University of Antwerp, Belgium

Supervisors

Prof. dr. G. Steenackers, University of Antwerp, Belgium

Prof. dr. X. Maldague, Université Laval, Québec

Members

dr. B. Ribbens, University of Antwerp, Belgium

Prof. dr. R. Penne, University of Antwerp, Belgium

Prof. dr. A. Osman, Hochschule für Technik und Wirtschaft des Saarlandes,
Germany

Prof. dr. K. Van Den Abeele, Catholic University of Leuven, Belgium

Prof. dr. D. Angelis, Free University of Brussels, Belgium

Contact

Ing. Simon Verspeek

University of Antwerp

Faculty of Applied Engineering

Invilab Research Group

Groenenborgerlaan 171 2020 Antwerpen, België

W: Invilab.be

M: simon.verspeek@uantwerpen.be

© 2023 Ing. Simon Verspeek

All rights reserved.

Acknowledgements

I would like to extend my profound appreciation to my esteemed advisors, Professor Gunther Steenackers and Professor Xavier Maldague, whose invaluable guidance and unwavering support have been instrumental in my successful journey through the complexities of doctoral research. Their profound knowledge and steadfast belief in my capabilities have significantly contributed to the culmination of this PhD.

Furthermore, I wish to express my sincere gratitude to my esteemed colleagues, whose professional camaraderie and personal friendships have enriched my academic experience. Both within and beyond the professional sphere, we have shared moments of significance. I hold in high regard the contributions of Robin Baetens and Bart Ribbens, who have consistently provided me with invaluable advice and a receptive ear. The transformation of professional relationships into cherished friendships has enhanced my workplace environment immeasurably. Therefore, I would also like to thank my friends who provided the necessary distraction and enjoyable moments during the execution of this doctoral journey.

To my family, I am indebted for their unwavering support throughout this demanding academic journey. Their unwavering faith in my abilities and the opportunities they have provided me to pursue this doctoral endeavor have been foundational to my scholarly aspirations.

Last but not least, I extend my heartfelt gratitude to my partner, whose unyielding support has been unwavering, even when it necessitated late-night work sessions, weekend commitments, and interruptions during vacations. Her understanding and encouragement have provided me with strength and resilience during challenging times.

In summary, the successful culmination of this PhD is a collaborative achievement, and I am profoundly thankful to all who have contributed to this endeavor. Your guidance, support, and camaraderie have transformed this academic journey into a fulfilling and rewarding experience. Thank you for your unwavering commitment to my success.

List of Abbreviations

IR	Infrared
FOV	Field Of View
DLST	Dynamic Line Scan Thermography
FEM	Finite Element Model
NDT	Non-Destructive Testing
VisNIR	Visible-Near Infrared
SWIR	Short Wave Infrared
MWIR	Mid Wave Infrared
LWIR	Long Wave Infrared
MES	Mehler Engineering + Service GmbH
GP	Gaussian Process
SE	Squared Exponential
ARD	Automatic Relevance Determination
US	Uncertainty Sampling
IVR	Integrated Variance Reduction
RMSE	Root Mean Square Error
DOF	Design Of Experiments
AI	Artificial Intelligence
GBVF	Gray Body View Factor
RBF	Radial Basis Function
MPI	Magnetic Particle Inspection
UT	Ultrasonic Testing
ECT	Eddy Current Testing
IRT	Infrared Thermography
RGB	Red Green Blue
HSI	Hyperspectral Imaging
UV	Ultraviolet

NUC	Non Uniformity Correction
FFT	Fast Fourier Transform
PCA	Principle Component Analysis

List of Publications

First Author

- Verspeek, S., Peeters, J., Ribbens, B., Steenackers, G. (2018). Excitation source optimisation for active thermography. *Proceedings*, 2(8), 1–7. <https://doi.org/10.3390/ICEM18-05325>
- Verspeek, S., Ribbens, B., Maldague, X., Steenackers, G. (2020). Optimisation of a heat source for infrared thermography measurements : comparison to mehler engineering + service-heater. *Applied Sciences*, 10(4), 1–10. <https://doi.org/10.3390/APP10041285>
- Verspeek, S., Gladines, J., Ribbens, B., Maldague, X., Steenackers, G. (2021). Dynamic line scan thermography optimisation using response surfaces implemented on PVC flat bottom hole plates. *Applied Sciences*, 11(4). <https://doi.org/10.3390/APP11041538>
- Verspeek, S., De Boi, I., Maldague, X., Penne, R., Steenackers, G. (2022). Dynamic line scan thermography parameter design via Gaussian process emulation. *Algorithms*, 15(4), 1–13. <https://doi.org/10.3390/A15040102>
- Verspeek, S., Ribbens, B., Maldague, X., Steenackers, G. (2022). Spot weld inspections using active thermography. *Applied Sciences*, 12(11), 1–12. <https://doi.org/10.3390/APP12115668>

Supporting Author

- Steenackers, G., Peeters, J., Verspeek, S., Ribbens, B. (2018). From thermal inspection to updating a numerical model of a race bicycle : comparison with structural dynamics approach. *Applied Sciences*, 8(2). <https://doi.org/10.3390/APP8020307>
- Peeters, J., Verspeek, S., Sels, S., Bogaerts, B., Steenackers, G. (2018). Optimised dynamic line scanning thermography for aircraft structures. *QIRT 2018 : 14th Quantitative Infrared Thermography Conference*, 687–695. <https://doi.org/10.21611/QIRT.2018.077>
- Peeters, J., Verspeek, S., Sels, S., Bogaerts, B., Steenackers, G. (2019). Optimized dynamic line scanning thermography for aircraft structures. *Quantitative Infra Red Thermography Journal*. <https://doi.org/10.1080/17686733.2019.1589824>
- Sels, S., Verspeek, S., Ribbens, B., Bogaerts, B., Vanlanduit, S., Penne, R., Steenackers, G. (2019). A CAD matching method for 3D thermography of complex objects. *Infrared Physics and Technology*, 99, 152–157. <https://doi.org/10.1016/J.INFRARED.2019.04.014>

- Sels, S., Bogaerts, B., Verspeek, S., Ribbens, B., Steenackers, G., Penne, R., Vanlanduit, S. (2020). 3D defect detection using weighted principal component thermography. *Optics and Lasers in Engineering*, 128, 1–6.
<https://doi.org/10.1016/J.OPTLASENG.2020.106039>
- Verstockt, J., Verspeek, S., Thiessen, F., Tondu, T., Tjalma, W. A., Brochez, L., Steenackers, G. (2021). Dynamic Infrared Thermography (DIRT) in biomedical applications : DIEP flap breast reconstruction and skin cancer. *AITA - Advanced Infrared Technology Applications : Proceedings of the 16th International Workshop on Advanced Infrared Technology Applications 2021, 26-28 October, 2021, Venice, Italia*, 8(1), 1–5.
<https://doi.org/10.3390/ENGPROC2021008003>
- Heirmans, R., Moor, D., Verspeek, S., Vrieze, D., Ribbens, B., Vanneste, M., Steenackers, G. (2021). Improving quality inspection of textiles by an augmented RGB-IR-HS-AI approach. 8(1), 1–4.
<https://doi.org/10.3390/ENGPROC2021008021>
- Verstockt, J., Verspeek, S., Thiessen, F., Tjalma, W. A., Brochez, L., Steenackers, G. (2022). Skin cancer detection using infrared thermography : measurement setup, procedure and equipment. *Sensors*, 22(9), 1–21.
<https://doi.org/10.3390/S22093327>
- Hillen, M., Sels, S., Ribbens, B., Verspeek, S., Janssens, K., Van der Snickt, G., Steenackers, G. (2023). Qualitative Comparison of Lock-in Thermography (LIT) and Pulse Phase Thermography (PPT) in Mid-Wave and Long-Wave Infrared for the Inspection of Paintings. *Applied Sciences*, 13(7), 1–13.
<https://doi.org/10.3390/APP13074094>

Abstract

Performing non-destructive inspections is widely used to evaluate objects for structural integrity. Infrared (IR) thermography is a common technique in the field of non-destructive testing. Both active and passive thermography are used to inspect objects depending on the type of defect to be inspected. Passive thermography is often used to determine the health of objects that generate heat during operation (e.g. a transformer, a motor, circuit boards, ...). Deviant heating patterns may indicate anomalies in the samples to be inspected. Active thermography on the other hand is based upon upsetting the equilibrium of the object by means of inducing a thermal wave. Active thermography is often used as non-destructive technique because of its advantages in comparison to others such as ultrasound testing, X-ray radiography, visual inspections etc. IR thermography is a fast, safe, contactless and full-field measurement technique to perform inspections. It has shown to be reliable in many applications and therefore more and more industrial companies and researchers show interest in exploring the field of thermographic inspections. Some disadvantages of thermography make it hard to implement the technique as a plug and play technique. The main disadvantage is the fact that an expert skilled in the art is needed to optimise the measurement setup and prescribe the needed parameters in order to perform accurate and efficient measurements. Another important drawback of the thermal inspections performed nowadays is the size limit of objects to be inspected. IR thermography is often performed keeping the sample stationary in the field of view (FOV) of the used camera. Research has been performed in order to inspect larger samples using dynamic line scan thermography (DLST), whereby a heat source and camera tandem moves relative to the specimen to be inspected. Performing measurements using DLST not only requires an expert skilled in thermography, but even one who has expertise in dynamic inspections. Since more parameters have an influence on the result, it becomes much harder to predict the optimal setup parameters.

This thesis focuses on providing an insight in the influence of the different parameters used in dynamic line scan measurements and using the acquired knowledge to predict an optimal parameter set.

First, a concise explanation of thermography will be given, explaining the working principle of the technology and describing different techniques that can be used in order to perform IR inspections. Second, the focus lies on the measurement-setup itself. In order to predict the most suitable parameter set, it is necessary to ensure the optimal working of all individual components. Afterwards, different techniques are investigated to perform parameter predictions and finally a novel method is presented to accurately align the images of the translating object. The proposed techniques are validated using industrial applications.

In order to enable the optimisation of the parameter set used for dynamic line scan thermography, an optimal measurement setup had to be defined. There exist line heating sources specifically for DLST measurements, but there were still some improvements possible. Therefore a new line heating source was developed using ray-tracing software. The second goal of this thesis was to generate an insight

in the correlation between different parameters of a dynamic inspection. This knowledge enables inspectors to predict possible parameters to perform dynamic measurements without the need of trial and error testing for longer periods of time. Getting insight in the working principle requires a lot of data and would therefore require an enormous amount of measurements. This procedure would be too time-consuming and expensive, resulting in seeking refuge in a finite element (FEM) simulation. The simulation resembles the DLST working principle making it possible to generate data relatively fast. Starting from this data, several methods are investigated to predict the optimal parameter set for dynamic line scan thermography measurements. The used techniques vary from established techniques such as response surface methodology to newer techniques such as artificial intelligence and Gaussian processes. The outcome of the different optimisation techniques is validated using experimental measurements. At first the focus was specifically on predicting the optimal parameter set for DLST based on finding one defect with specific properties. However, techniques investigated in later stages of this thesis, also prove interesting to offer an answer to questions where multiple solutions can be found and focus more on supporting the inspector in selecting a suitable parameter set.

Finally the captured images have to be aligned in order to be able to perform post-processing. Existing methods require a synchronisation between the movement of the sample and the frame rate of the thermal camera. The technique in this thesis enables sub pixel shifting without the need of synchronisation.

The knowledge obtained in this thesis can offer an insight in the working principle of dynamic line scan thermography and enables the user to define an optimal parameter set for thermal inspections of samples that do not fit the field of view of the camera.

Contents

I	Introduction	1
1	Introduction	3
1.1	Research context	3
1.2	What is thermography?	4
1.3	Passive thermography	6
1.4	Active thermography	7
1.4.1	Mechanical thermography	8
1.4.2	Inductive thermography	9
1.4.3	Flash thermography	9
1.4.4	Lock-in thermography	10
1.4.5	Pulse thermography	11
1.4.6	Dynamic Line scan thermography	11
1.5	Focus and outline of the thesis	13
1.5.1	Research focus	13
1.5.2	Main innovations	14
1.5.3	Thesis outline	14
II	Applications	17
2	Spot weld inspections using active thermography.	19
2.1	Introduction	19

2.2	Materials and Methods	20
2.2.1	Excitation methods	21
2.3	Results	23
2.3.1	Lock-in Thermography using light heating	24
2.3.2	Pulse Thermography using light heating	26
2.3.3	Inductive Thermography	28
2.4	Discussion	32
2.5	Conclusion	33
III	Setup optimization	35
3	Excitation source optimization for active thermography.	37
3.1	Introduction	37
3.2	Methodology	39
3.2.1	Requirements	39
3.2.2	Geometry	39
3.2.3	Simulation	44
3.3	Results	47
3.4	Conclusions	49
IV	Parameter optimization	50
4	DLST optimization using Response Surfaces implemented on PVC flat bottom hole plates.	51
4.1	Introduction	52
4.2	Materials and Methods	54
4.2.1	Finite element simulation	54
4.2.2	Response surface Parameters	56

4.2.3	Response surfaces	61
4.3	Results	64
4.4	Discussion	68
4.5	Conclusion	70
5	DLST optimisation: comparison Reinforcement Learning and Response Surfaces.	71
5.1	Introduction	72
5.2	Finite Element Simulation	73
5.2.1	Finite Element Model	73
5.2.2	Expressions	75
5.2.3	Journal File	76
5.3	Matlab	76
5.3.1	Result Sampling	77
5.3.2	Top Surface Filtering	78
5.3.3	Top Surface Resampling	78
5.4	Reinforcement Learning	79
5.4.1	Reward	80
5.4.2	Training	80
5.5	Discussion	81
5.6	Conclusion	82
6	Thermography Parameter Design via Gaussian Process Emulation	83
6.1	Introduction	84
6.2	Materials and Methods	86
6.2.1	Data generation	86
6.2.2	Gaussian processes	87
6.2.3	Active learning	88

6.3	Results	90
6.3.1	Model performance	91
6.3.2	Parameter Design	94
6.4	Discussion	98
6.5	Conclusion	100
7	A novel line scan algorithm for unsynchronised dynamic measurements.	101
7.1	Introduction	101
7.2	Materials and Methods	104
7.2.1	Algorithm	105
7.3	Results	110
7.3.1	IR camera	111
7.3.2	UV camera	112
7.3.3	HSI camera	114
7.4	Discussion and Conclusion	116
V	Conclusion	119
8	General conclusion and future work.	121
8.1	General conclusion	121
8.2	Future Work	124

Part I

Introduction

Chapter 1

Introduction

This chapter is divided in five sections which will handle the prior knowledge needed for the rest of this thesis. The first section will place the research in a general context. The second section explains the working principle of thermography and describes different methods of performing thermography. The third section focuses on the use of passive thermography while the fourth section will elaborately elucidate different active thermography principles. The last section will describe the need of the research in this manuscript and the benefit of it.

1.1 Research context

Since several decades safety became more and more important in all kinds of fields such as safety regulations at work, safety precautions in cars, etc. Due to the increasing world population, transportation has grown immensely and in order to reduce the increasing carbon footprint, salvation was sought in the use of lightweight composite materials. In order to further reduce the CO_2 emissions, the focus is no longer only on the transportation sector. Recycling and extending the lifespan of objects is becoming more important in the fight against climate change. Considering that safety and recycling are both very important, it is necessary to be able to assess the structural integrity of a structure or object. Conventionally structural integrity was evaluated by manufacturing additional samples that would be submitted to destructive tests. Performing destructive inspections however is not sustainable since more objects have to be manufactured and consequently more resources and energy was used. It is particularly pernicious for single-piece manufacturing, since double the number of parts must be produced in order to subject one to destructive testing. Furthermore it is impossible to assess the integrity of a sample with the purpose of reusing it. Therefore the inspection method shifted towards non-destructive testing (NDT) in the last decades with techniques such as ultrasonic testing, magnetic particle inspection, eddy-current testing, radiography, infrared thermography, etc. In this work there is only focused on the use of thermographic inspections.

1.2 What is thermography?

Infrared thermography, often called IR thermography or shortly thermography, is an optical inspection technique that captures thermal radiation. This radiation is situated in the electromagnetic spectrum between 0.4 and 14 μm as represented in Figure 1.1. Infrared rays can be further divided in several categories: Visible-Near infrared (VisNIR) between 0.4 and 1.4 μm , Short Wave infrared (SWIR) ranging from 1.4 to 2.5 μm , Mid Wave infrared (MWIR) starting at 2.5 μm and extending to 7 μm and Long Wave infrared (LWIR) beginning at 7 μm and ending at 14 μm . The category of infrared rays emitted by an object is determined according to Wien's Displacement Law:

$$\lambda_{peak} = \frac{b}{T_{object}} \quad (1.1)$$

where λ_{peak} is the calculated wavelength in μm , b (Wien's displacement constant) is approximately equal to 2898 $\mu\text{m}\cdot\text{K}$ and T_{object} is the temperature of the object to be inspected in Kelvin. Wien's law is accurately applicable in a range above very low (close to absolute zero) and below extremely high temperatures (temperature of stars). However the equation is most frequently applied between 100 nm and 10 μm or in other words in the corresponding temperature range between 300 K and 28000 K. Using Equation 1.1 it can be clearly seen that radiation emitted by objects around ambient temperature (300 K) will have wavelengths in the Long Wave infrared spectrum.

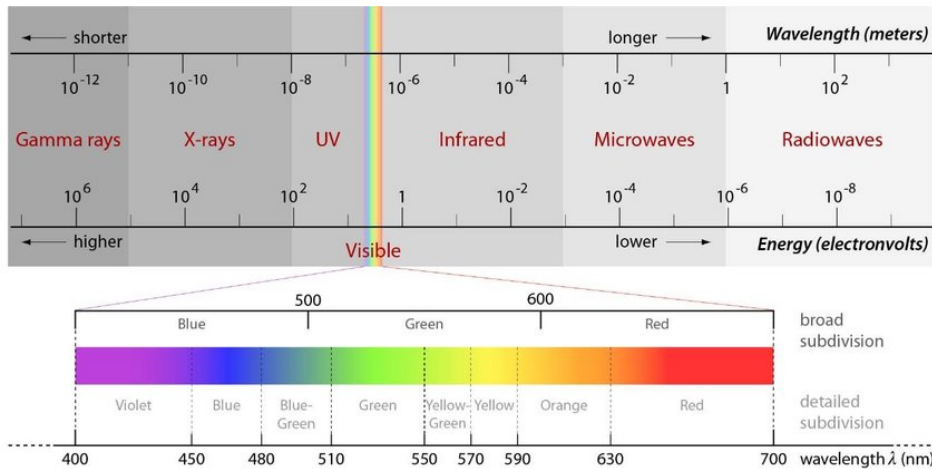


Figure 1.1: Overview of the electromagnetic spectrum. Infrared rays have wavelengths between 0.4 and 14 μm . [1]

The use of thermal cameras found its origin in military applications since an in-

frared detector translates the incident infrared radiation to temperature information making it possible to perform non-contact inspections of the thermal properties of an object. IR thermography enables the detection of human beings, animals and every object that emits heat in pitch-black circumstances as can be seen in Figure 1.2.



Figure 1.2: Examples of images taken with an infrared camera. a) use of IR thermography to detect wildlife during night [2], b) thermal inspection of a solar panel to search for defects.

Infrared thermography can be performed in different manners depending on the used approach, excitation source, excitation style and measurement configuration. A visualisation can be seen in Figure 1.3. The various parameters will be discussed extensively in following sections.

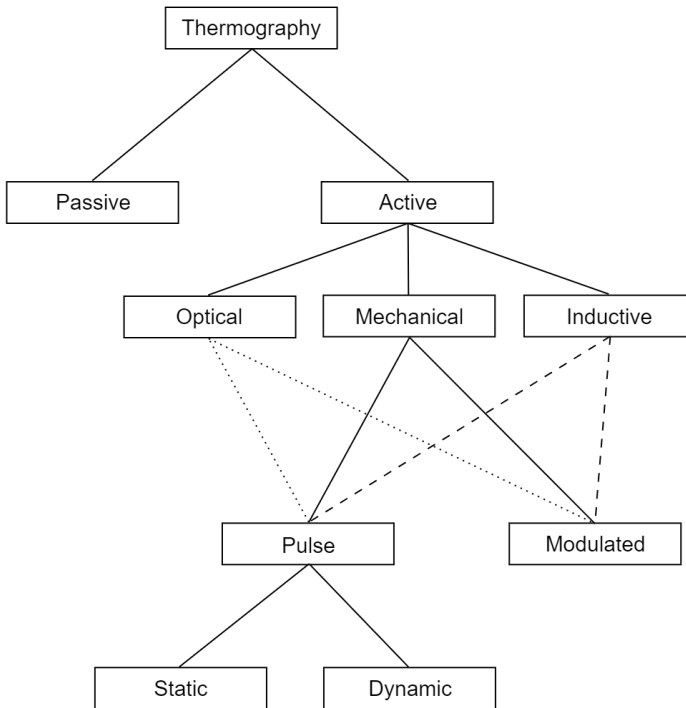


Figure 1.3: Visual representation of different thermography techniques [3].

1.3 Passive thermography

The first division that can be made in performing IR thermography is based on the used approach. Every object above absolute zero (0 K) will emit infrared radiation according to its temperature. Using a thermal camera it is possible to detect objects during situations where other cameras such as an RGB camera for example could not offer information. As shown in Figure 1.2 infrared thermography can be used to monitor wildlife during night. Since this approach relies on the radiation solely depending on the temperature of an object, no external excitation is needed. Therefore the inspections are performed in nearly steady state conditions. Performing passive thermography however is only possible if the contrast in thermal radiation of the object and the surroundings is large enough. This technique is commonly used in wildlife monitoring, hunting, search & rescue operations, inspection for building insulation, inspection of electrical facilities, etc [4, 5, 6]. However passive thermography can also be used to perform inspections during manufacturing such as weld inspections [7] or during load testing [8].

1.4 Active thermography

The second approach of performing infrared inspections is active thermography. As the name states, this technique uses an active excitation to induce a thermal contrast in the object to be inspected. Unlike the steady state inspections of passive thermography, active thermography relies on the transient thermal response of the sample on the excitation. Using this transient behavior it is possible to detect anomalies within the structure. The induced thermal wave starts at the surface of the sample to be inspected and travels through the material. Inspecting sound objects (objects without an internal defect) using active thermography would result in even heating and cooling of the whole sample, assuming the material possesses isotropic thermal properties. However, a defect in the sample will result in a visible hotspot on the recorded surface as can be seen in Figure 1.4.

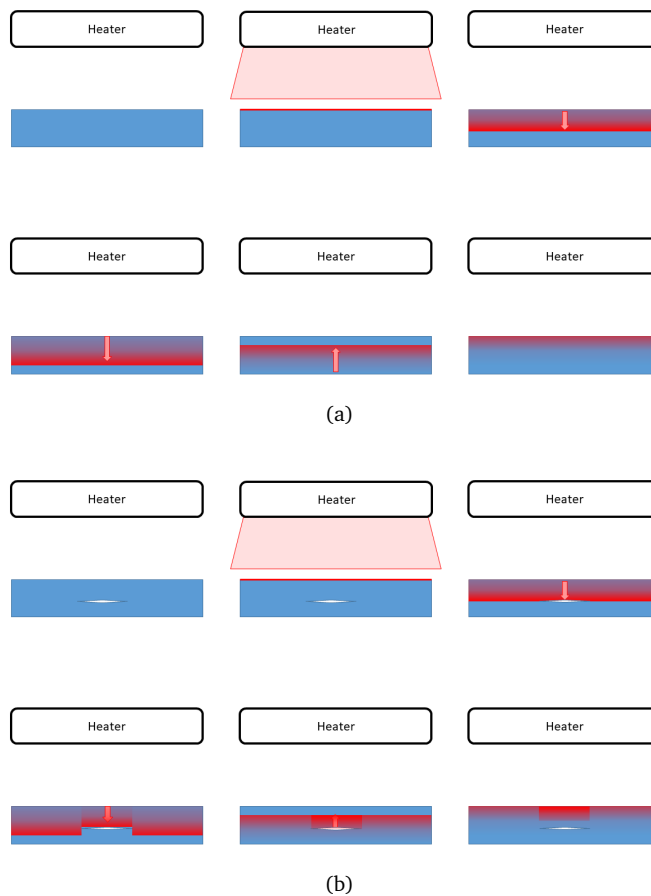


Figure 1.4: The induced thermal wave propagates through the sample to be inspected. a) Sound objects will heat and cool evenly. b) Defects in samples will result in a hotspot on the inspected surface.

The use of active thermography is widely recognized as a reliable, fast and contactless method of performing non-destructive testing [9, 10, 11, 12]. Since active thermography is used in several domains and on samples of different properties, the excitation method is very dependent on the application. As can be seen in Figure 1.3 a subdivision can be made according to the used excitation source (optical, mechanical and inductive). The most accessible excitation method is through the use of an optical source since this can be obtained by using widely available halogen lamps. There exist commercially available lamps specifically designed for active thermography in order to ensure an optimal heating, but these are not required in order to get an adequate measurement [13]. Performing inductive and mechanical thermography require the purchase of specific equipment in order to excite the object to be inspected.

Independently of the used excitation source, the manner in which the excitation is applied differs according to the performed measurement technique. The excitation can be performed using pulse excitation or modulated excitation as can be seen in Figure 1.5.

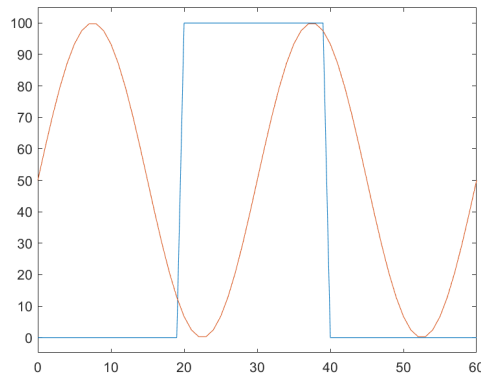


Figure 1.5: Visualisation of pulse (blue) and modulated (red) excitation signals over a period of one minute. The excitation power varies between 0 and 100 %. Pulse excitation uses a block wave during a certain amount of time, while modulated signals are continuous during the entire measurement. The frequency and pulse lengths can be adapted to the desired heating power during a measurement.

1.4.1 Mechanical thermography

Mechanical thermography is better known as vibrothermography or ultrasonic thermography. The sample is excited through ultrasonic mechanical vibrations. The defect induces friction in the sample, resulting in generated heat. This heat diffuses to the surface and is recorded by the thermal camera. There is some discussion whether this inspection method is non-destructive since there is a possibility that the defect enlarges due to the movement and friction in the sample to be inspected. A major advantage of this inspection technique is that the mechan-

ical energy is directly transformed into heat around the defect while the sound areas are not affected. Ultrasonic thermography is often used to investigate the integrity of joints [14] and delaminations [15].

1.4.2 Inductive thermography

Inductive thermography uses an inductive source to excite the sample to be inspected, therefore this method is only suitable for conductive materials. An inductive coil is placed near the surface of the sample to be inspected. Induction heating can be performed using both front and back heating as can be seen in Figure 1.6. The distance between the coil and the sample has a significant influence on the induced heating of the sample. Placing the induction coil closer to the conductive sample will increase the heating for the same amount of heating power. This technique is often used to inspect welds [16] and detect cracks [17].

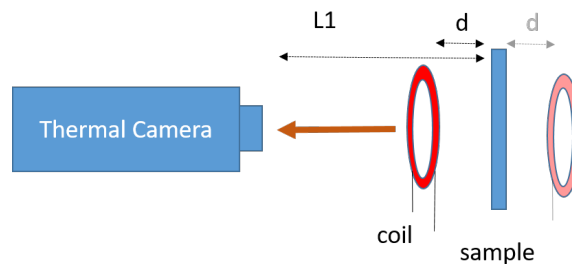


Figure 1.6: Visualisation of induction thermography whereby a sample is heated using an induction coil. The coil can be placed between the thermal camera and the sample (front heating) or behind the sample (back heating).

1.4.3 Flash thermography

The first method in the subdivision of the optical excitation method is flash thermography. This technique often uses Xenon flash lamps in order to induce a short pulse of high-power light. The light pulse can be described as a dirac pulse. The short amount of exciting the sample will limit the heating of the sample to be inspected. Since the stimulus is short, the induced thermal wave will not penetrate the object really deep. Therefore this technique is often used to inspect artwork [18, 19]. Flash excitation can also be used to inspect materials with high thermal conductance like metals. Exciting these materials for a longer amount of time will heat the whole sample minimizing the temperature difference between the sound area and the region of interest. Since the excitation relies on a powerful burst of light, these measurements can not be performed without extensive safety precautions. In case someone would look into the lamps on time of flashing it could make the person going blind. The measurement setup resembles the visualization

in Figure 1.7 with the only difference that the halogen lamps are replaced with Xenon flash lamps.

1.4.4 Lock-in thermography

Lock-in thermography relies on modulated heating signals in order to excite the sample to be inspected. In general the induced wave is a sine-modulated signal described by a chosen amplitude and frequency. In order to perform accurate lock-in measurements, it is essential that the excitation signal and the camera are synchronised properly. Since the excitation signal is a sine wave, the induced thermal wave will also be a sine wave and is in phase with the original signal. However a defect in the sample will reflect the thermal wave and will result in a reflected sine wave out of phase with the original signal. If there are no defects the back of the sample will reflect the induced signal wave and will result in the reflected wave. Lock-in thermography measurements are typically processed using a Fast Fourier Transform in order to create both amplitude and phase images during evaluation. The phase shift between the emitted heat wave and the reflected heat wave can be used to estimate the depth of the detected defect [20]. Another advantage of the phase images can be found in the nearly insensitivity to non-uniform heating. Amplitude images on the other hand experience less influence of noise, resulting in higher contrast images [21]. The chosen frequency and amplitude of a lock-in thermography inspection are very important in order to perform decent measurements. The amplitude determines the total heat induced in the sample and therefore it is essential to keep the application in mind. For artwork inspections for example the temperature difference as a result of heating can not exceed several degrees Celcius. The frequency on the other hand defines the maximum penetration depth of the thermal sine wave. High frequent sine waves will only penetrate the sample a small amount while long frequencies penetrate much deeper. The maximal depth at which a defect can be discovered using lock-in thermography is described by the thermal diffusion depth μ of a material. The maximal penetration depth can be calculated using Equation 1.2.

$$z = C_1 * \sqrt{\frac{\mu}{\pi * f_b}} \quad (1.2)$$

with f_b the blind frequency, C_1 a constant with typically a value equal to 1.82 and $\mu = \frac{\kappa}{C_p * \rho}$. It is possible to always heat the sample using a low frequency sine wave in order to ensure that defects at different depths can be detected. This however would make it unnecessarily time-consuming since typically two periods are used during lock-in thermography measurements.

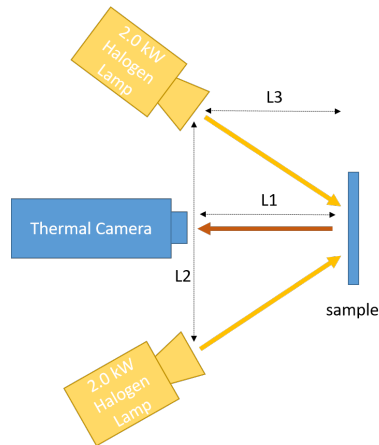


Figure 1.7: Measurement setup to perform active thermography using optical heat sources. The heating lamps can both be placed in a front heating setup as well as in back heating. The distances shown can be configured as wished depending on the application. In our lab two lamps are used from the OTVis system. [13]

1.4.5 Pulse thermography

Besides lock-in thermography, it is also possible to perform inspections using pulse optical heating. The measurement setup is identical to the setup in Figure 1.7. A pulse wave, also called block wave, is used to induce a thermal excitation in the sample to be inspected. A representation of a pulse wave can be seen in Figure 1.5. The excitation signal is constrained by the amplitude and the duration chosen depending on the application. A linear correlation can be found between the surface temperature of the object and the combination of these parameters. A higher amplitude will result in more power being delivered to the surface of the object and therefore the surface will heat up faster compared to a smaller amplitude. Measurements with a longer heating duration on the other hand will allow the thermal wave to propagate slower through the sample limiting the surface temperature. Therefore it is very important to keep the dimensions and the maximum use temperature of the object to be inspected in mind. Pulse thermography is the most popular method of performing active thermography inspections because of its simplicity and fast operation.

1.4.6 Dynamic Line scan thermography

All techniques mentioned above are performed in static conditions. The measurements are considered to be static if the sample, camera and heating source are stationary with respect to one another. Performing static inspection, there are some disadvantages that have to be kept in mind. Objects to be inspected have

to fit in the field of view (FOV) of the thermal camera, therefore the dimensions are limited. It is possible to place the camera at a larger distance of the sample, but this would reduce the spatial resolution and thereby the chance of detecting a defect. A rule of thumb states that the diameter of a defect needs to be at least covering a 3x3 square grid as can be seen in Figure 1.8. This is adopted to ensure that measurements cannot be confused with noise and to allow for a temperature gradient across an object. Consequently a camera with a higher resolution can detect smaller defects when positioned at an equivalent height in comparison to a camera with a lower resolution.

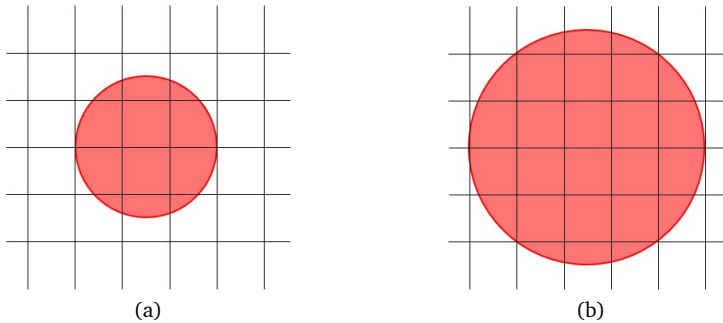


Figure 1.8: Representation of a general rule of thumb whereby the area of a defect has to be at least covering a 3x3 square grid of pixels in order to be able to detect the defect. a) Visualisation of a defect that will not be objectively detectable. b) This defect will be detectable since it is larger than a 3x3 square grid of pixels.

In order to be able to inspect larger objects using active thermography, salvation can be sought in Dynamic Line Scan Thermography (DLST). Dynamic Line Scan Thermography can be seen as performing pulse thermography, with the main difference that the sample has a relative translation to the heating source and the thermal camera. The optical heating source used during DLST is a line heating device since it is advantageous to minimize the heating area in order to maximize the power density (W/cm^2) on the sample to be inspected. The line heating device is placed in tandem with the thermal camera and move relatively to the object. The object is heated in parts while moving and therefore the heating of a specific part can be seen as pulse heating whereby the amplitude is defined by the power density of the heating and the duration is determined by the translation speed.



Figure 1.9: Representation of heating during Dynamic Line Scan Thermography. From the point of view of a location on the samples surface, the heating can be considered as pulse heating.

Active thermography is still a recent non-destructive technique and therefore an expert skilled in the field is still needed in order to determine the optimal parameters for an inspection. Dynamic Line Scan Thermography is a subdivision of active thermography and is still a challenging task even for experts in active thermography. In comparison to static thermographic inspections, DLST measurements are depending on much more parameters. These parameters will be thoroughly explained in Part 3 of this doctoral thesis.

1.5 Focus and outline of the thesis

1.5.1 Research focus

Since active thermography and Dynamic Line Scan Thermography (DLST) in particular, is still a recent technique and an expert skilled in the field is needed to predict the measurement parameters, this technique is not yet widely incorporated in industry. Therefore this research will focus on optimizing DLST on both the hardware as the software part of it. The objectives of this research are stated as followed:

1. Define a relationship between the different parameters used in Dynamic Line Scan Thermography. In order to achieve this, a finite element simulation was performed and fed with multiple parameter sets. A correlation is sought between the different parameters and between a set of input parameters and the resulting surface temperature above a defect.
2. Use the gained knowledge and performed simulations to generate a response surface to get a better knowledge and define optimal parameter sets depending on a set of fixed parameters.
3. Benchmark the response surface generation to new developed techniques in order to find the most efficient way to predict the optimal parameter set for a partially defined set of parameters. Investigating the possibility to use the recent techniques to discover interesting insights in DLST measurements.

1.5.2 Main innovations

The main innovations of this thesis can be found in the optimization techniques used and the knowledge gained regarding dynamic line scan thermography. This thesis explored various methods, including the use of Reinforcement Learning and Bayesian emulation, to predict optimal parameter sets to perform dynamic line scan thermography. Particularly, the use of Bayesian emulation has shown great promise, as it not only predicts optimal parameter combinations but also provides straightforward answers to industrially relevant questions. It allows a layperson to quickly assess whether a specific combination will yield useful results. An additional significant outcome of this research is a better understanding of the influence of various parameters in the measurement process. It has been found that the distance between the camera and the heat source, in combination with the movement speed, has the most significant impact on the extent to which a defect is visible. If these parameters are chosen in the right proportion, the required amount of heating energy can be kept to a minimum without sacrificing contrast in the thermal images. To further reduce the amount of energy, a line emitter was designed, which, through its elliptical shape and additional reflectors, focuses the required heat into a narrow region.

1.5.3 Thesis outline

The thesis is structured in four main parts: Introduction, Thermography applications, Setup Optimization and Parameter Optimization. The first part places the research in a general context, explains the basics of thermography needed for this manuscript and the need for the research is clarified. The second main part will explain some additional thermography measurements that have occurred during my research in order to expand my expertise in hands-on thermography measurements as well. Part three elaborates the need of an optimized line heating source and describes the research performed to design an optimized line heater. The fourth main part handles the software optimization of predicting the optimal parameter set based on some predefined variables. These optimizations happened using response surface methodology, reinforcement learning and bayesian optimization. The techniques are compared to each other based on the amount of simulations needed to train a model that is capable of predicting the optimal parameter set for Dynamic Line Scan Thermography inspections. Since DLST measurements are dynamic measurements, it is not possible to process them in exactly the same way as static measurements. It is necessary to reshape the data and therefore a novel technique is explained in the third part as well. The most important innovations are explained in the third part of this manuscript as this handles the parameter optimization. Among the optimization methods a comparison is made between new methodologies and widely known ones. A visualisation of the outline of this thesis can be seen in Figure 1.10.

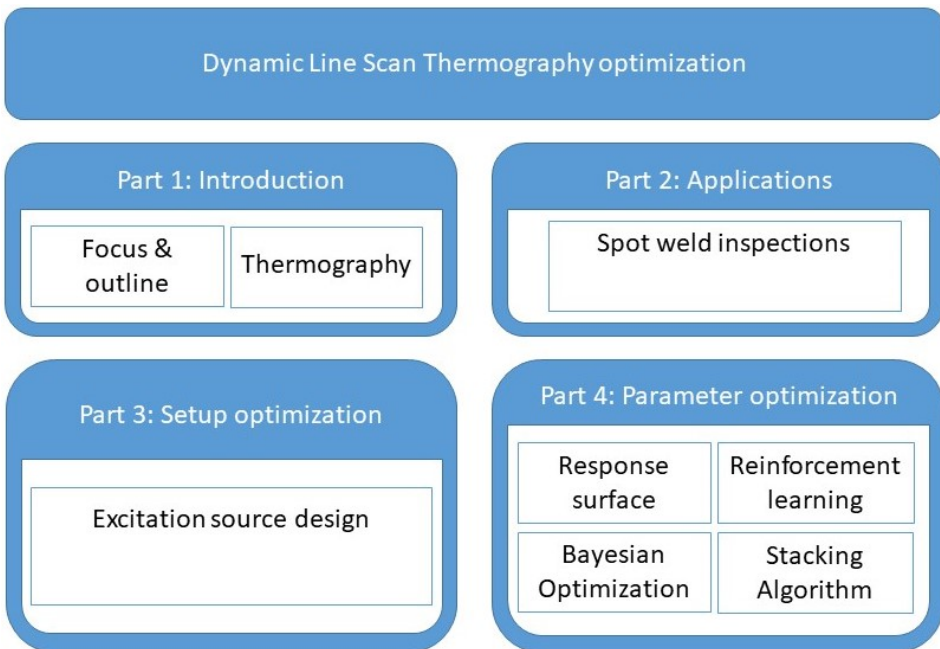


Figure 1.10: Visual representation of the outline of this manuscript. The main innovations are situated in part four.

Part II

Applications

Spot weld inspections using active thermography.

The second Part of this doctoral thesis discusses the use of active thermography to inspect spot welds using different excitation methods. A comparison is made between optical heating and induction heating performed both in front and back heating in order to find the most optimal solution for in-situ inspections within the manufacturing process. The spot welds were inspected with the goal of determining whether they were completely closed and whether a material change had occurred inside the weld. This chapter is published in MDPI Applied Sciences as "Spot weld inspections using active thermography" [22].

2.1 Introduction

Performing quality inspections during manufacturing has increased enormously in the last decades and more and more manufacturers discover the use of non-destructive inspection methods. Using non-destructive testing it is no longer needed to manufacture additional parts in order to submit them to destructive inspections. Those inspections are performed in a variety of fields such as aircraft construction, metal structure manufacturing, composite manufacturing, etc. Several different techniques are being used in order to examine the structural integrity of the manufactured parts. Amosov et al. [23] performed ultrasonic testing on riveted joints in aviation construction, Deepak et al. [24] compared different non-destructive inspection techniques to assess the quality of welded joints and Jasiuniene et al. [14] performed ultrasonic testing on complex titanium and carbon fibre composite joints. It is proven that non-destructive testing can offer a reliable inspection method in order to investigate the structural integrity of materials and joints. In the automotive industry many spot welds are used to combine parts together. On average the body work of a car alone consists already of 5000 spot welds [25]. Nowadays the quality of the spot weld is investigated using destructive research resulting in many disadvantages. If the quality of the spot weld is not sufficient

a larger batch of spot welds will be disapproved since not every single spot weld can be tested. Therefore car manufacturers search for alternative solutions in non-destructive inspections. An easy inspection method can be found in visual inspections, however these examinations can only be performed by someone skilled in the art. An alternative can be found in penetrant testing. This technique is suitable to detect cracks, but is not capable of showing defects inside the material. Besides penetrant testing, another surface examination technique can be found in eddy current testing [16, 26, 27]. Performing subsurface inspections is possible using ultrasonic testing, but an extreme accuracy is needed to place the transducer in the middle of the spot weld. Performing visual surface inspection of spot welds is not sufficient since a spot weld can look decent, but no internal structure change has occurred. As explained in [28] a proper spot weld contains multiple sections. The weld nugget has a different internal structure in comparison to the region around it. Therefore it is important to inspect the surface of a spot weld as well as the internal structure. An alternative approach can be found in active thermography for non-destructive inspections [28, 17, 11]. Several efforts have been performed regarding the use of active thermography for spot weld inspections [29, 30, 31, 32]. Scientific research often focuses on the ability to inspect spot welds using a specific measurement setup. Runnelmalm and Appelgren [16] and Jonietz [32] perform thermography using light sources as external heating, Kastner [30] and Schlichting [31] combine thermography with laser excitation. However in a manufacturing process not every measurement technique can be used. It is for instance possible to inspect spot welds using laser thermography, but due to safety issues it is not suitable to be used in the production hall without extensive safety precautions. This study focuses on finding the most optimal measurement setup to perform active thermography inspections during the manufacturing process. Multiple excitation methods are described in this chapter divided in several paragraphs based on the used heating method. For each measurement setup a variety of parameters is tested and compared. Besides a variation in excitation parameters, a comparison between two post-processing techniques is performed for each excitation type. The used measurement setups can be found in Section 2 Materials and Methods. Section 3 describes the influence of the different parameter sets and post-processing techniques.

2.2 Materials and Methods

Nine different samples are inspected using different active thermography techniques in order to find the best inspection method. The samples are divided into two groups: A and B. The A-series exists of four samples with the same thickness (2.5 mm) and one sample that is 3.15 mm thick. All samples of series B have a thickness of 2.5 mm. An RGB image of the samples can be seen in Figure 2.1. The A-series samples are used to find the best measurement setup for the inspection of spot welds using active thermography. The B-series will function as a validation set to test the best suitable measurement method.



Figure 2.1: Nine samples, divided into two series. The A-series consists of four samples with a thickness of 2.5 mm (1-4) and sample 5A is 3.15 mm thick. The B-series only consists of four samples with a thickness of 2.5 mm. The spot weld highlighted by the blue cross is the inspected spot weld for each sample.

The parameters used to weld the samples can be found in Table 2.1.

The camera used for these experiments is a FLIR X6540sc with a 25 mm lens. This cooled camera has a spectral range between 1.5 and 5.5 μm and a thermal sensitivity smaller than 25 mK. The thermal camera is mounted on a tripod and placed in front of the sample.

2.2.1 Excitation methods

Different excitation techniques are used in order to find the optimal measurement setup for spot-weld inspections. The used techniques can be divided by the heating mechanics used: light heating and inductive heating. Heating the samples using

Sample	1A	2A	3A	4A	5A	1B	2B	3B	4B
Current [kA]	8	6	3.5	5	16	8	6	3.5	5
Weldtime [ms]	400	200	600	200	300	400	200	600	200
Force [kN]	3	2.6	3	3.5	2.8	3	2.6	3	3.5

Table 2.1: Parameters used to weld the samples.

halogen lamps is performed using lock-in thermography and pulse thermography.

2.2.1.1 Light heating

Two halogen lamps of 1.8 kW each are used as heating source. These lamps are from the brand Edevis and can be found online as the OTvis system. The lamps are mounted on a tripod and placed on either side of the thermal camera. The measurement setup for the light heating experiments can be found in Figure 2.2 and the according parameter values are discussed in Table 2.2.

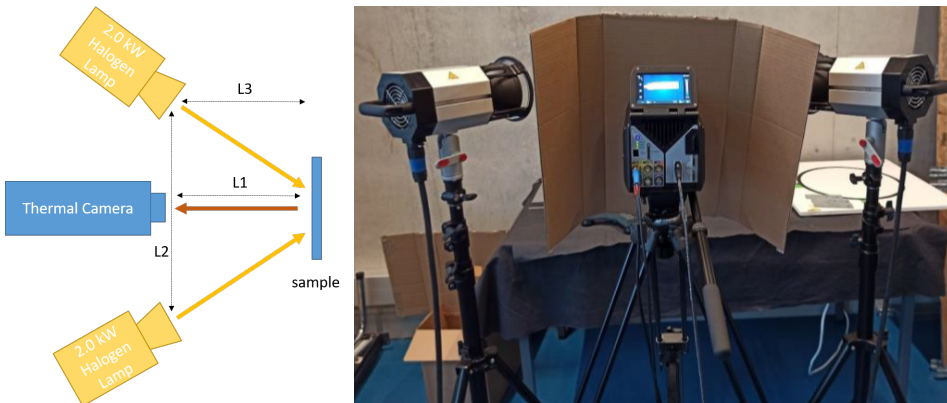


Figure 2.2: Visualisation of the measurement setup used for light heating experiments. The left image is a schematic representation of the setup and the right image is taken during measurements. The cardboard is placed in front of the thermal camera to prevent radiation emitted by the camera reflecting on the sample to be inspected. Since the thermal camera generates heat itself, the camera can become visible in the captured thermograms. Using the cardboard as a barrier this adverse effect is removed.

2.2.1.2 Induction heating

The measurements performed in this manuscript using induction heating are performed using a 1.5 kVA Leon LIH-15 heater. The heating energy is transferred

Parameter	Value
Distance camera - sample 'L1' [m]	0.44
Distance lamp - lamp 'L2' [m]	0.88
Distance lamp - sample 'L3' [m]	0.44
Angle lamp - camera [°]	45

Table 2.2: Parameters used during light heating measurements. A representation of the parameters can be found in Figure 2.2.

to the sample through an induction coil containing two windings. The induction heating device is mounted using a clamp at the desired location and distance next to the sample to be inspected. The sample is heated using inductive step heating. The pulse duration can be found in Table 2.6. A visualisation of the measurement setup can be seen in Figure 2.3.

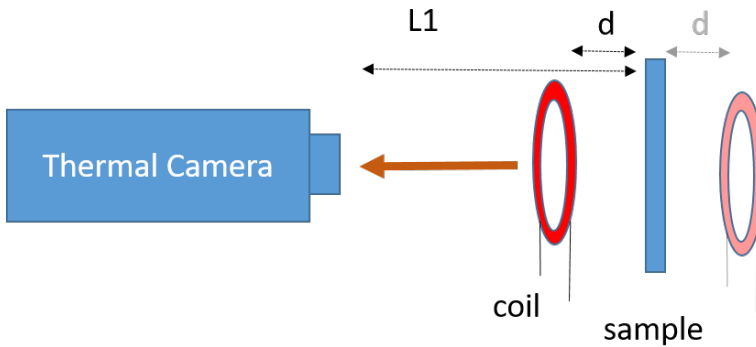


Figure 2.3: Schematic overview of the measurement setup used for induction thermography measurements. Both front and back heating have been performed. The parameter values can be found in Table 2.3.

Table 2.3: Parameter values used during induction heating measurements for the inspection of spot welds. A visual representation of the parameters can be found in Figure 2.3.

Parameter	Front induction heating	Back induction heating
Distance camera - sample 'L1' [m]	0.053	0.055
Distance sample - coil 'd' [m]	0.03	0.025

2.3 Results

Due to welding, the metallic parts are connected together resulting in a place where the heat can be distributed through more material. In addition the internal

structure of the metal has changed in welds that are properly performed. Using infrared thermography a difference in heat transfer can be observed between the welded area and the rest of the sample. The welded regions will show a different cooling down in comparison to the non welded regions. This difference can be emphasized using post-processing. The difference in internal structure of a decent weld will also result in a difference in cooling down and can again being emphasized using post-processing. A more thorough explanation on why thermography can be used to inspect spot welds can be found in [32]. In this research 75 samples are generated in three different categories: stick welds, optimal nugget size and splash limit. Consecutively thermal measurements were performed in order to investigate whether it is possible to differentiate the samples of each category. The results were positive, however the measurements were performed using flash thermography and therefore were not suitable to perform in-situ.

The results of the different heating techniques and post-processing are shown and discussed below. The results are divided into different sections depending on the used excitation method.

2.3.1 Lock-in Thermography using light heating

Since lock-in thermography is based on sinusoidal excitation, the optimal amplitude and frequency combination has to be found in order to increase the contrast of the interesting regions. The amplitude corresponds to the amount of energy injected in the sample to be inspected, the frequency on the other hand determines the time within which the heating energy is injected into the sample. A lower frequency results in a longer heating time. Multiple experiments have been performed on one sample in order to find suitable parameter combinations. These experiments have shown that a lower frequency (e.g. 0.05 Hz) resulted in better images. Higher frequencies (e.g. 1.4 Hz) generated noisy thermograms. The influence of the amplitude was determined as well and a minimal amplitude of 2200 W was needed to be able to perform analyses on the thermal data. For each sample two parameter combinations have been used. The used parameter sets can be found in Table 2.4.

Table 2.4: Parameter combinations used for the inspection of each sample using lock-in thermography. The number of periods is kept constant at a value of two and the amplitude is kept constant at 2900 W. Only two periods are used since research has shown that the use of two periods results in adequate measurements and more periods have no significant improvement.

	Parameter set 1	Parameter set 2
Frequency [Hz]	0.05	0.4
Amplitude [W]	2900	2900
Number of periods	2	2

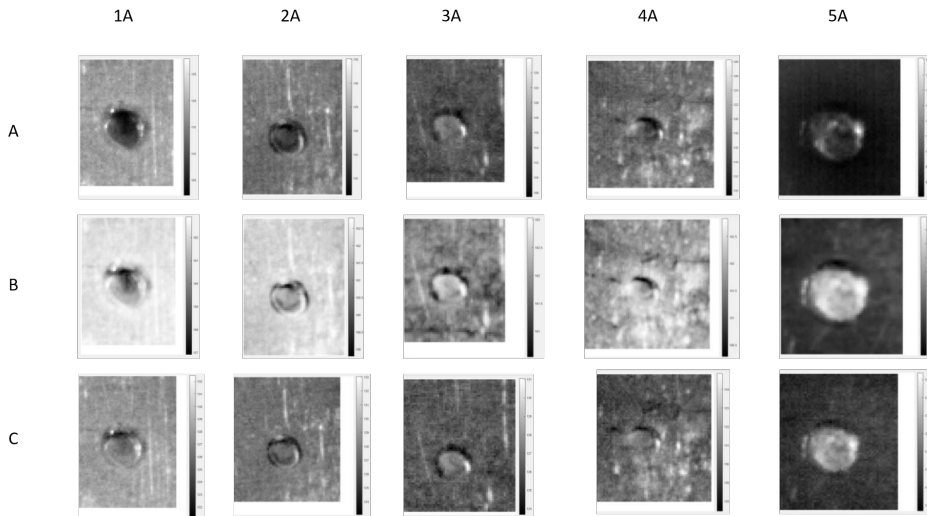


Figure 2.4: Amplitude images taken from Fast Fourier Analysis for the different samples during three measurements. Experiment A is performed using an excitation frequency of 0.05 Hz and a Fourier frequency of 0.025 Hz, experiment B uses an excitation frequency of 0.05 Hz and a Fourier frequency of 0.05 Hz and during experiment C the samples were excited using a frequency of 0.4 Hz and analysed using a Fourier frequency of 0.2 Hz. Only the most interesting images are shown out of the large data sets.

The experiments are analysed using both Fast Fourier Transform (FFT) and Principle Component Analysis (PCA). PCA is based on singular value decomposition and the goal of this technique is to reduce the amount of variables while losing the least amount of relevant information. FFT on the other hand is based on the approximation of the data through the sum of harmonic waves. The phase and amplitude can be calculated from this approximation. A thorough explanation on both post processing techniques can be found in [33] and [34]. Investigating the FFT images in Figure 2.4, it is visible that samples 1A, 2A and 3A show a closed circular shape around the spot weld and 4A only shows a part of the circle. The images of sample 5A doesn't suffice to make a conclusions about the shape of the spot weld. Another interesting aspect of a spot weld is the internal material structure inside the spot weld. Spot welds should have a different internal structure in comparison to the material around it. In samples 1A, 2A and 5A, a different thermal behaviour can be detected inside and outside the spot weld what a different material structure might suggest. In sample 3A and 4A this phase shift is not visible. Besides the Fourier analysis, PCA is performed in order to generate relief images. The first five principle components are calculated for each measurement and the most characterising image is chosen in order to inspect the spot weld. The remaining power In the PCA images of samples 1A and 2A the circular shape of the spot weld is visible. Sample 2A has the most clear circle shape. Sample 3A is less visible in the PCA in comparison to the FFT analysis, but the circle around the

spot weld is still visible. Sample 4A has no closed boundary and sample 5A shows a capricious relief. The images can be seen in Figure 2.5.

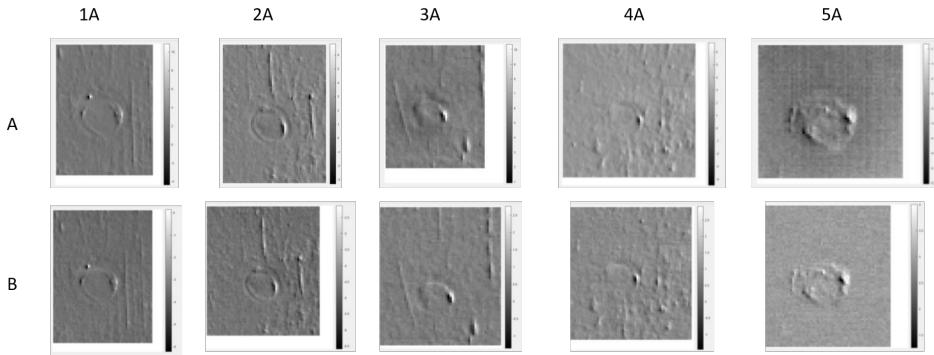


Figure 2.5: Images taken from the Principle Component Analysis of the five samples during two experiments. The excitation frequency of experiment A is 0.05 Hz and the frequency of B is 0.4 Hz. The images serve as an indication on the shape of the spot weld. The boundary of the weld itself shows clearly and therefore it is possible to investigate whether or not the boundary is completely closed. Samples 1A, 2A and 3A show a closed boundary, while 4A only shows a partially closed boundary and the inspection of sample 5A does not show a clear closed boundary.

2.3.2 Pulse Thermography using light heating

The second light heating technique investigated in this manuscript is pulse heating. The measurement setup is visualised in Figure 2.2 and the parameters corresponding to 'L1', 'L2' and 'L3' can be found in Table 2.2. In order to investigate the influence of the pulse duration, each sample is subjected to experiments using different parameter sets. The amplitude is constant with a value of eight, which is similar to the measurements using lock-in thermography. The parameter sets used during the pulse thermography measurements can be found in Table 2.5.

Table 2.5: Parameter combinations used during the pulse thermography measurements. The value of the amplitude is kept constant at 2900 W in order to ensure an adequate heating intensity.

	Parameter set 1	Parameter set 2
Amplitude [W]	2900	2900
Pulse duration [s]	1	3

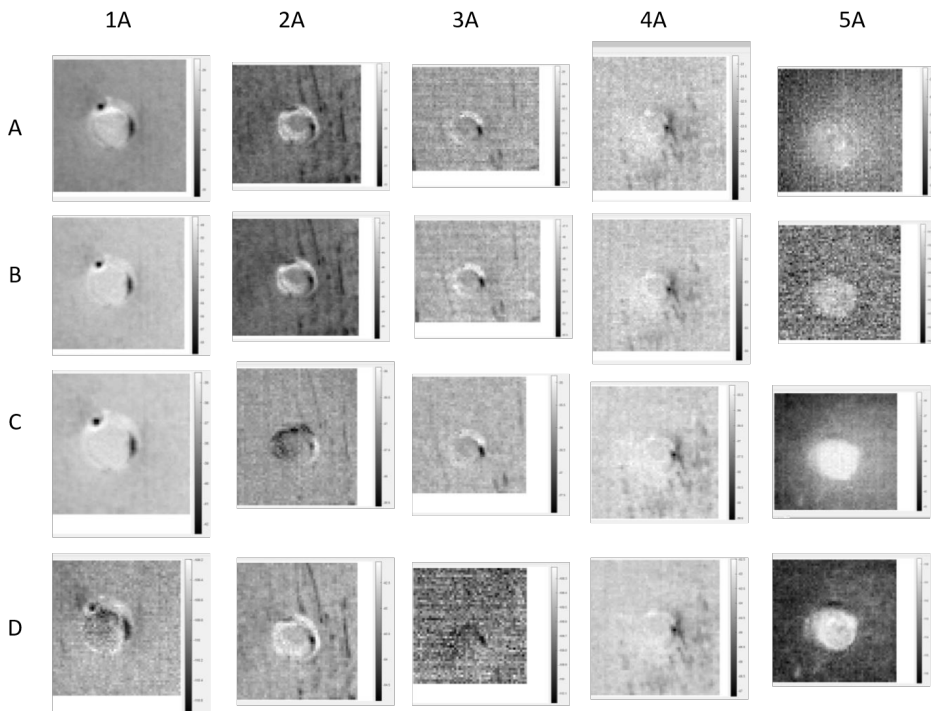


Figure 2.6: Amplitude images taken from the fast Fourier transform analysis performed on pulse thermography data. Experiment A is performed using a pulse duration of 1s and a Fourier frequency of 0.038 Hz. Experiment B has a pulse duration of 1s as well and analysed using a Fourier frequency of 0.076 Hz. A pulse duration of 3s is used for experiments C and D, the used Fourier frequencies are 0.035 Hz and 0.142 Hz.

Figure 2.6 visualises the results of the FFT analyses of the pulse thermography inspections. Similar results can be observed between experiments using a pulse duration of 1 and 3 seconds for samples 1A, 2A and 3A, however a longer pulse time leads to better results regarding samples 4A and 5A. Both sample 1A and 2A show a clear visible circle around the spot weld and a different thermal behaviour between the region inside and outside the weld can be distinguished. The black regions inside the spot weld of sample 1A shows a distinct phase shift, while in sample 2A this phase shift is not visible. Sample 3A has a visible circular shape as well, but there is no phase difference between the region inside the weld and the region around it. This might mean that the weld is not optimal since no change in metallic internal structure has occurred. Similar to the lock-in measurements, sample 4A doesn't show a contour of the spot weld. In the images of sample 5A, a difference can be seen between the inside and outside of the spot weld, but there is no clear boundary visible. Besides FFT analyses, principle component analyses have been performed on the pulse thermography data. The results of this processing can be seen in Figure 2.7.

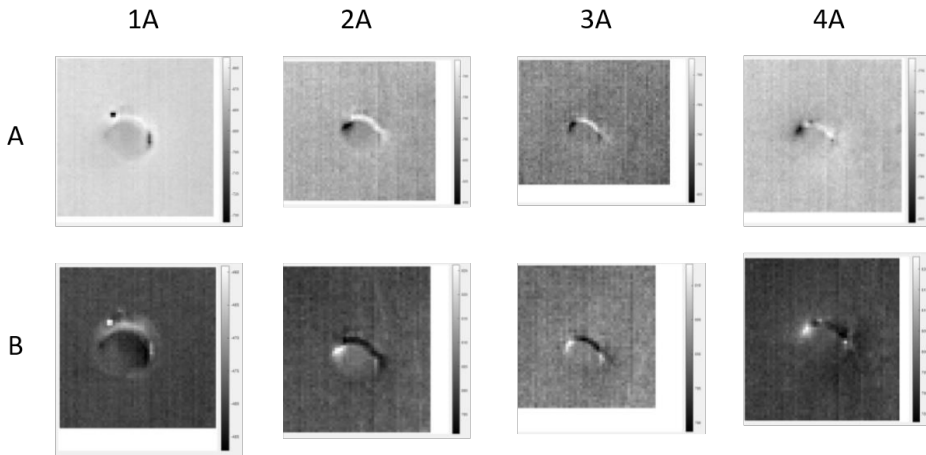


Figure 2.7: Results of the PCA processing of the pulse thermography data. The first five principle components are calculated and afterwards the most pronounced images are selected. Experiment A is conducted using an amplitude of 2900 W and a pulse duration of 1 second. Experiment B is conducted using the same amplitude and a pulse duration of 3 seconds. There is no data for sample 5A since the processing did not result in useful information. Sample 4A shows a similar result to previous results, namely no closed boundary can be detected. Samples 1A, 2A and 3A result in clear closed boundaries.

2.3.3 Inductive Thermography

The five samples of the A-series are subjected to induction thermography measurements. The inspections are performed both in front and back heating and for each heating method three heating times are compared. The heating times can be found in Table 2.6.

Table 2.6: Parameters used during inductive thermography of spot welds. Each sample of the A-series is inspected using these parameters.

	Parameter set 1	Parameter set 2	Parameter set 3
Induction time front heating [s]	5	10	19
Induction time back heating [s]	4	8	15

The thermal data captured during the experiments of sample series A, using induction heating are only processed using PCA since the FFT processing did not lead to useful images. Snapshots taken from the PCA on the data captured during front heating induction are shown in Figure 2.8.

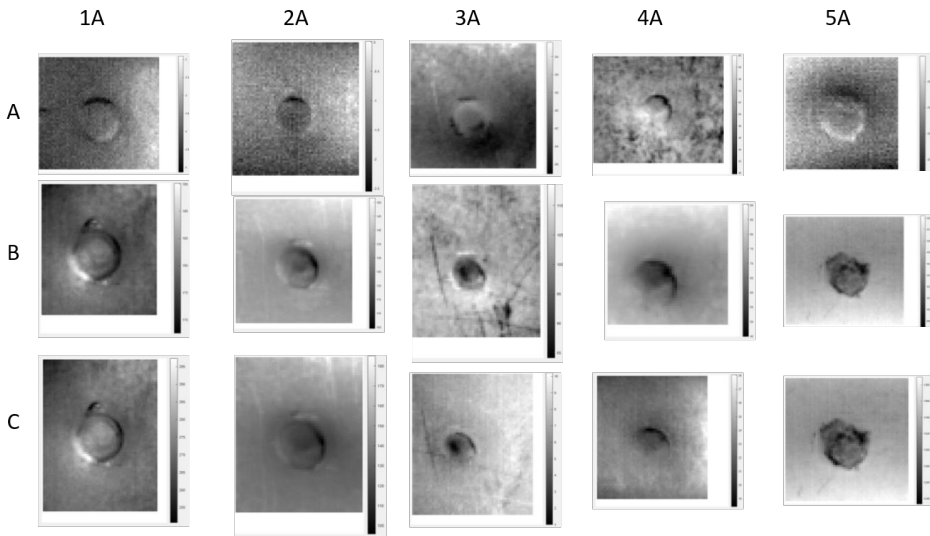


Figure 2.8: Images taken from the Principle Component Analysis performed on the thermal data captured using induction heating of the front side of the sample. Only the first five principle components are calculated and afterwards the most pronounced images are selected. Experiment A is performed using an induction time of 5 seconds, experiment B has an induction time of 10 seconds and the sample was heated for 19 seconds in experiment C.

Besides front heating, the back of each sample is heated during three experiments. The induction times for each experiment are again noted in Table 2.6. The thermal data is only processed using PCA since FFT did not result in useful images.

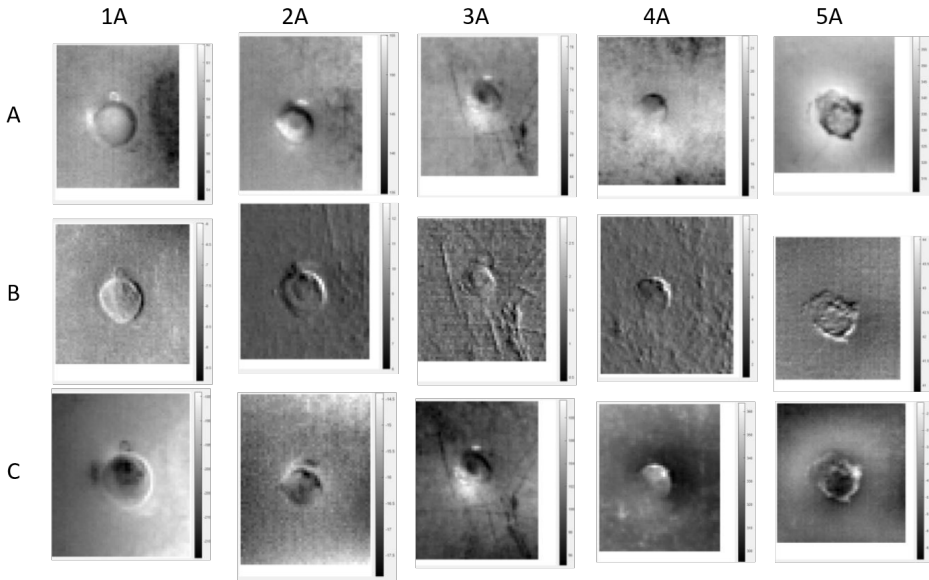


Figure 2.9: Processed data images from experiments performed using back heating. During experiment A an induction time of 4 seconds is used, during experiment B this was 8 seconds and experiment C is performed using 15 seconds of heating. The data is a selection of images out of the first five principle components.

Since induction thermography is a fast technique and it results in qualitative images, only this technique will be used for the inspection of the remaining four B samples. The optimal parameters found during the experiments of series A can be found in Table 2.7. These parameters will be used in the inspection of the samples of the B series. In contrast to the processing of the A series, the thermal data of the B series is processed using FFT and PCA. Both techniques resulted in decent quality images for this series. The results of the FFT processing of the front heating of the samples can be seen in Figure 2.10 and the PCA results can be found in Figure 2.11. The processed images related to back heating the sample can be seen in Figures 2.12 and 2.13.

	Front induction heating	Back induction heating
Excitation time [s]	19	15
Distance coil - sample [m]	0.03	0.04

Table 2.7: Best parameters found during the measurements on the A-series samples. The samples of the B-series are inspected using these parameters.

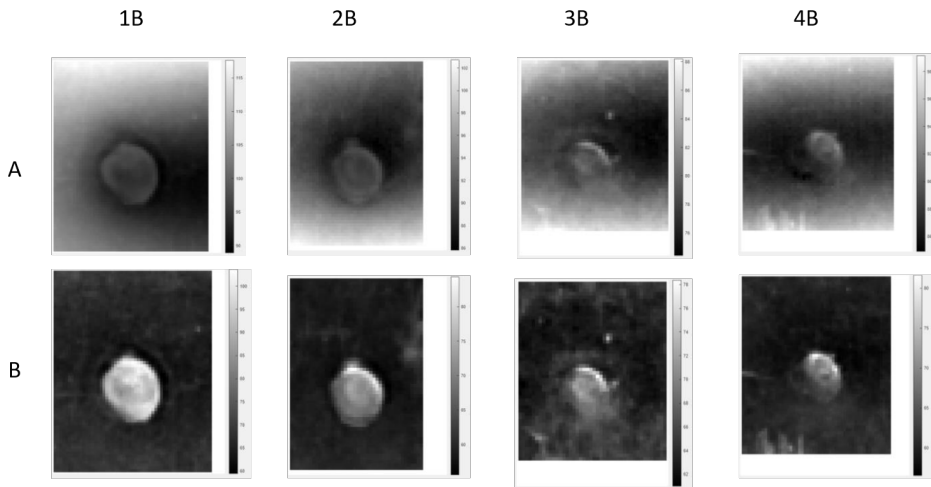


Figure 2.10: Amplitude images from the FFT processing of the thermal data captured using induction heating from the front side of the B-series samples. Row A show the phase images of the measurements using a excitation duration of 19 seconds and row B visualises the amplitude images.

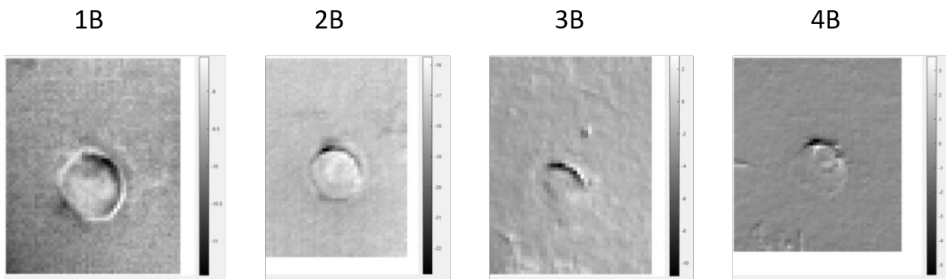


Figure 2.11: Snapshots taken from the Principle Component Analysis of the thermal data of front induction heating. The most pronounced images are shown out of the calculated first five principle components.

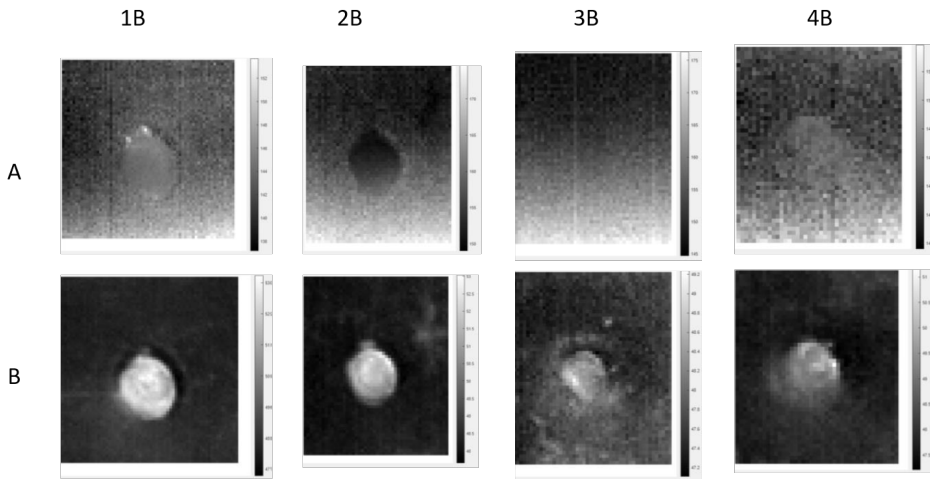


Figure 2.12: FFT results of the B series samples heated from the back during 15 seconds. Row A shows the phase images and row B the amplitude images. The phase images are not sufficient enough to make a conclusion about the spot welds, however the amplitude images show a clear difference between the region inside and outside the spot weld.

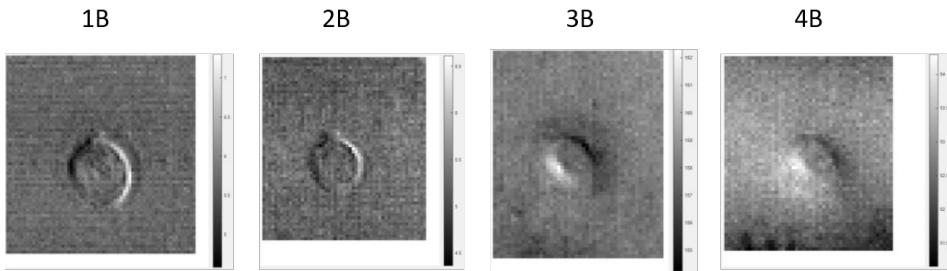


Figure 2.13: Results of the Principle Component Analysis of the B series samples heated from the back. From the raw data the first five principle components are calculated and the most pronounced image is selected afterwards.

2.4 Discussion

In this study a comparison is performed between different active thermography techniques in order to find the most suitable solution for the inspection of spot welds. The samples were heated using light heating and induction heating and processed applying both Fast Fourier Transform and Principle Component Analysis. As light heating excitation both lock-in thermography and pulse thermography are investigated. For each excitation method multiple parameter sets have been

explored such as: frequency variations for lock-in thermography and variations in pulse duration for pulse thermography. For each parameter five different settings are tested for both front and back heating in order to find the most adequate measurement setup. Induction heating showed to be the most suitable technique for spot weld inspections since it results in clear data images and low inspection times. Improving the measurements using induction thermography can be possible by minimizing the distance between the coil and the sample and increase the amount of windings of the excitation coil. Both front and back heating resulted in good quality images in inductive thermography, making it possible to be used in the manufacturing process. In decent spot welds a clear contour can be detected and the region inside the circular boundary has a different thermal behavior in comparison to the material around the spot weld. Considering the samples used in this research, we conclude that samples 1A, 2A, 1B and 2B are the only valid spot welds.

2.5 Conclusion

The aim of this research was to determine the best method to perform infrared thermography during car manufacturing. Several heating techniques are not suitable to use in a manufacturing process without extensive changes such as safety precautions. Since a car body is a complex shape it is not always possible to inspect the welds using back heating, therefore a solution had to be found using only front heating. An additional requirement was found in the use of robotic inspection. In order to minimize the necessity of a human inspector, it should be possible to perform the inspections automatically using a robot. Keeping these requirements in mind, the best inspection method can be found in inductive thermography. These measurements can be performed using only front heating and the camera and heating device can be mounted on the same robot. Using induction thermography for the inspection of spot welds it is possible to determine if the different characteristics that determine a good weld are present or not. A proper spot weld should show a distinguishable circular shape with a closed boundary and a different thermal behaviour inside and outside the welded regions. Boundaries that are not fully closed or have an irregular shape indicate that parts of the weld are not fully melt together or the weld puddle has blown out. It is not sufficient to evaluate a spot weld only on the shape of the weld itself. In order to deliver the needed strength the welded materials have to melt into each other inside the welding region. Therefore it is necessary to determine whether the internal structure of the weld has changed in comparison to the surrounding area. Further investigations can be made to the induction heating in order to minimize the needed heating time. Improvements could be found in optimizing the distance between the induction spools and the sample and by increasing the amount of loops in the induction coil. In future work the use of artificial intelligence will also be investigated in order to automatically classify spot welds.

We would like to thank Volvo Ghent for providing the samples used in this manuscript.

Part III

Setup optimization

Excitation source optimization for active thermography.

Before investing time and effort in optimizing the measurement parameters, one must be certain that the individual components are performing adequately. Since the movement of the sample is the key feature of Dynamic Line Scan Thermography, it is important to optimize the components that are specifically related to the movement. The movement can be achieved using a robot, cobot, conveyor belt, translation stage, etc. which are widely used and highly optimized components. The heating on the other hand is often performed using ordinary halogen lamps since commercially available line heaters are significantly more expensive. This chapter will discuss the optimization of a line heating device This chapter is published in MDPI Applied Sciences as "Optimisation of a heat source for infrared thermography measurements : comparison to mehler engineering + service-heater." [35]

3.1 Introduction

Non-destructive testing is globally progressing in the world of material inspections. The purpose of these tests is to inspect the structural integrity of objects without damaging the product itself. Until today, extra products needed to be produced to put them through destructive tests. Those non-destructive evaluations provide a swift, reliable and cost-effective manner to investigate objects without harming their purpose [36, 37].

There exist two types of infrared thermography based on the source of the evaluated temperatures. Every object exceeding absolute zero (0 K) emits infrared radiation. In passive thermography, the measured temperature differences are solely dependent on the emissivity and the temperature of the object to be inspected. Active thermography depends on exciting the test object using an external source in order to measure the temperature change between the heating and cooling phase. Multiple excitation sources exist in active thermography based on different heating

techniques such as halogen lamps, flash lamps, laser heating ultrasonic excitation, microwaves, eddy currents excitation, etc. In order to choose the right source to perform infrared measurements, one should consider the advantages and disadvantages of each source. Laser heating makes it possible to heat only small regions. Halogen lamps on the other have the advantage to heat the specimen in a cheaper and safer way.

Halogen lamps are widely used in infrared thermography because of the cost and broad wavelength spectrum. A disadvantage of using halogen lamps is the large heating region of the object to be inspected. One could try to minimise the heated region by using a slit allowing only a part of the heating energy to leave the reflector of the heating source. With the aid of a slit, the rays outside the desired heating area are blocked and a loss of possible heating energy occurs. One can see that the amount of blocked rays should be minimised. Additionally, diffraction causes the available rays to diverge out of the aperture further reducing the heating energy density. Figure 3.1 displays two preliminary set-ups that are used in our lab to minimise the heated region.



Figure 3.1: Two experimental set-ups are displayed as they are used in our lab: **(Left)** empirical test-setup for Dynamic Line Scan Thermography on a conveyor belt. A wooden plate wrapped in aluminium foil was mounted underneath a patio heater. In the middle of the plate, a slit with desired width and length was cut in order to create the reflector shape. **(Right)** cylindrical reflector constructed to concentrate the radiation in a narrow line. This heater is used in dynamic measurements as a hand-held heater. Starting from a hollow tube a slit was milled with the desired width in order to create the reflector shape. Both setups use a thin slot to minimise the heated region. Only the electromagnetic radiation passing through the slit will heat up the specimen to be inspected. Other rays will be blocked and thereby a large amount of energy is wasted.

Designing an optimised reflector could offer a safe and cost-effective heating source when combined with a halogen tube lamp. It could be a great substitute for using laser excitation and could facilitate the further development of Dynamic Line Scan Thermography. To increase the temperature difference between the heating and cooling down of the object, the available heating power of the halogen lamp needs to be concentrated in a small region. Concentrating the power enables the possibility to deliver more excitation power in a small time period. This results in a powerful heating. The heating source approximates rather flash excitation than

long step heating.

Several studies are performed in order to focus electromagnetic radiation in order to produce heat. Almost all these applications are powered by sunlight and use parabolas in order to focus the radiation in a single point [38, 39, 40]. According to the reflecting property of a parabola, rays originating in the focal point of the parabola will be reflected parallel to each other. Lee et al. [41, 42] investigated the possibility to use parabolic and elliptical mirrors to generate local heating of high-strength steels. Unvala and Maries [43] checked the heating peculiarities of a tungsten halogen lamp combined with an elliptical reflector shape. Using a 1 kW heating source, a heated region of 2 cm with heating temperatures of 1200 °C were generated.

We propose an approach to merge the local heating of laser heating with the safety of tungsten halogen tube lamps. A lamp reflector is designed using ray tracing software in order to achieve the focused power.

3.2 Methodology

3.2.1 Requirements

The heat source should meet several predefined requirements: the focus length is defined at about 10 cm based on the dimensions of the commercially available Mehler Engineering Services (MES)-heater [44]. The radiation will be focused into a small region at this distance from the emitting light source. Secondly, the used source should be a tungsten halogen lamp, also known as a halogen lamp. Tungsten halogen tube lamps are safe to use in almost all conditions and they are universally accessible. Furthermore, the heated region has to be as small as possible and we intend to concentrate a minimum of 80 % of the heat radiation. The more the radiation is focused into a smaller region, the less energy is needed to provide the same energy density. Radiation focusing can be performed in multiple ways: for example, using mirrors/reflectors or using lenses. Heat rays on the other hand cannot be focused using glass lenses because of the energy losses in the lenses resulting in heating the lenses. A germanium lens on the other hand is suitable for focusing heat radiation, but these are very expensive.

3.2.2 Geometry

Multiple mathematical shapes exist with all different reflection characteristics: parabola, ellipse, etc. The reflective characteristic of a parabola is confirmed by multiple studies [45, 46, 47, 48] and states that incident parallel rays are reflected to the focus point of the parabolic reflector, provided that the rays are parallel to the parabola axis. Consequently, rays originating in the focal point are always

reflected parallel to the symmetry axis of the parabola. These reflected rays automatically create a wide heated region. We intend to concentrate the radiation in a small point for every section of the reflector in order to minimise the heated region; therefore, a parabola can not be used as a reflector shape for this purpose.

Another interesting mathematical shape is an ellipse because of its reflective property and could offer a solution for our application. This reflective property is better known as the focal property of an ellipse [49]. We could mount the tungsten halogen lamp in F1 of the ellipse to focus the radiation in F2. Thanks to this approach, all radiation originating in the halogen lamp will be reflected to the heated area on the specimen (F2). Figure 3.2 visualises the different properties of a parabola and an ellipse.

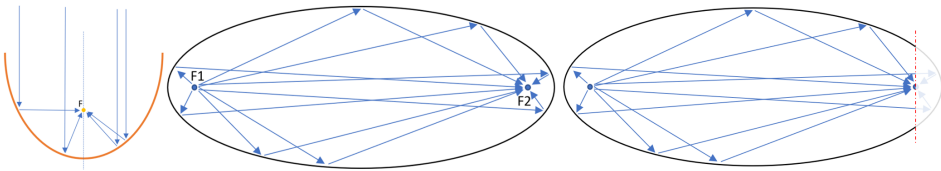


Figure 3.2: The reflecting characteristics of a parabola and an ellipse are visualised. All parallel rays entering a parabolic reflector will be focused on the focal point. Each ray leaving one focal point of the ellipse will be reflected to the other focal point of the ellipse. One can see that cutting the ellipse on the red line will result in rays not being reflected by the elliptical shape towards the second focal point.

According to the focal property of an ellipse, it is theoretically possible to focus the electromagnetic radiation on a small point as long as the elliptical shape remains closed, provided that the emitting source is concentrated on the other focal point of the ellipse. As can be seen in Figure 3.2, cutting a part of the elliptical reflector results in rays not being reflected towards the second focal point. For our application, it is not possible to keep the elliptical reflector closed in order to be able to heat the object. The radiation has to leave the reflector in order to induce a temperature increase of the sample.

Removing a part of the elliptical reflector leads to a wider radiation pattern as a result of the rays not being reflected towards the focus point. Using simple mathematics, the percentage of direct heating rays reaching the object can be calculated. In Figure 3.3, a simplified representation of the halogen tube lamp and the direct heated region of the object can be seen.

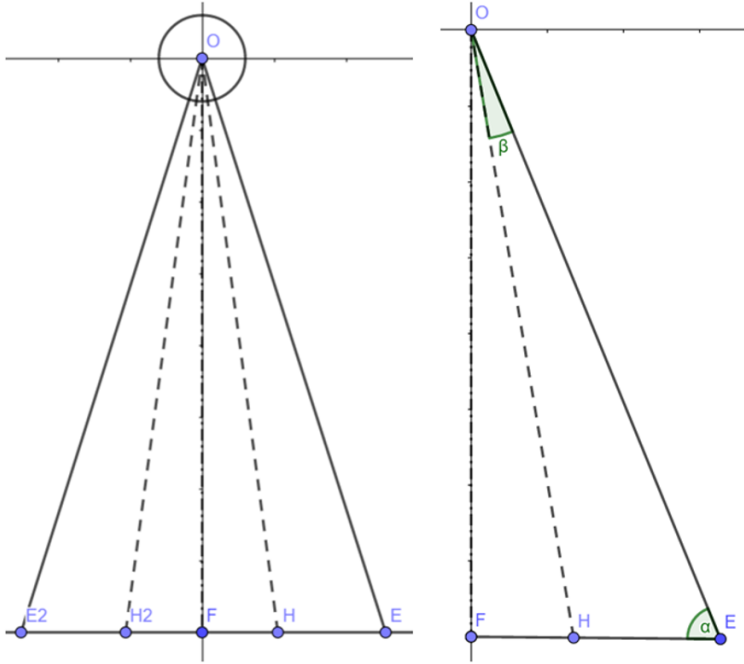


Figure 3.3: This figure shows a geometrical representation in order to calculate the amount of the radiation not being reflected by the elliptical reflector. The left image represents the complete set-up with the halogen tube lamp in point O and the focal point in point F. $\overline{E_2E}$ represents the width of the illuminated region by direct rays leaving the tube lamp. The right image can be used to determine the angles needed to calculate the unwanted illuminated area. Representation of the optimised reflector shape and the related ray trajectories.

The desired focus distance of the heat source is represented by \overline{OF} . The width of the opening in the reflector shape is called $\overline{E_2E}$ and $\overline{H_2H}$ describes the wanted illuminated region. In the right-angled triangle $\triangle OFE$ (the angle between \overline{OF} and \overline{FE} equals 90 degrees), the length of \overline{OE} can be found using Pythagoras Theorem:

$$\overline{OE}^2 = \overline{OF}^2 + \overline{FE}^2 \quad (3.1)$$

The value for α can be found using:

$$\alpha = \sin^{-1}\left(\frac{\overline{OF}}{\overline{OE}}\right) \quad (3.2)$$

The width of the total heated region equals \overline{FE} and the wanted illuminated region is presented by \overline{FH} . The length of the undesired heated region can easily be found by subtracting \overline{FH} of \overline{FE} . In triangle $\triangle OHE$, the length of \overline{OH} can be found using

the law of cosines:

$$\overline{OH}^2 = \overline{HE}^2 + \overline{OE}^2 - 2 * \overline{HE} * \overline{OE} * \cos(\alpha) \quad (3.3)$$

Therefore, the angle between \overline{OH} and \overline{OE} can be calculated applying the law of cosines a second time:

$$\overline{HE}^2 = \overline{OE}^2 + \overline{OH}^2 - 2 * \overline{OE} * \overline{OH} * \cos(\beta) \quad (3.4)$$

The area of the lamp heating the specimen outside the wanted region can be calculated by:

$$A_{\text{outside}} = \beta * r^2 \quad (3.5)$$

This area is the combination of the circular sectors in the triangles $\triangle OHE$ and $\triangle OH_2E_2$. One should note that β is in radians to calculate the area of the circular sector. The percentage of the lamp heating the specimen directly can finally be found:

$$\%_{\text{outside}} = \frac{A_{\text{outside}}}{\Pi * r^2} * 100\% = \frac{\beta}{\Pi} * 100\% \quad (3.6)$$

Ending the elliptical reflector shape at 10 cm from the top leads to an illuminated region of 2.7 cm and the wanted maximum width of the region is 1 cm. Conforming to the previous calculations, the difference between the heated and desired region of 1.7 cm equals an area of 2.68 % of our excitation source. The purpose of the research is to focus the light in a heated region of maximum 1cm. Because of the opening in the elliptical reflector shape, a circular sector of the radiating tungsten halogen tube lamp will directly heat the specimen. To assure the wanted 1-cm-wide concentrated radiation area is attained, extra reflectors are added in the reflector shape. The length and the placement of the additional reflectors can be found using simple mathematics as can be seen in Figure 3.4.

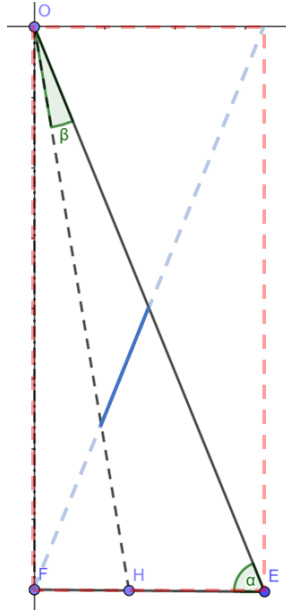


Figure 3.4: Visualization of how the additional reflectors are determined. The reflectors can be found using the diagonal of the rectangle with the height of the desired focus length and the width of half the desired heated region. The start and end point of the straight reflector are defined by the intersection of the diagonal with the line segments \overline{OH} and \overline{OE} .

Considering a rectangle with height \overline{OF} and width \overline{FE} , \overline{OE} is a diagonal in this rectangle. The other diagonal starting in point F has the same equation as the additional reflector. The reflector starts at the intersection of the diagonal and \overline{OH} and ends at the intersection of the diagonal and \overline{OE} . This way, the unwanted heated region is nullified. The characteristics of the straight reflectors are therefore dependent on the desired heating width and the width of the opening in the elliptical reflector. Figure 3.5 shows the optimised reflector geometry as result of the ray-tracing simulations. The optimisation procedure is discussed further on in this thesis. The halogen tube lamp has a diameter bigger than the focal point of the ellipse; therefore, the radiation will not originate precisely in the focal point of the ellipse. Assuming that the radiation leaves the halogen tube lamp perpendicular to the length of it, the extended rays intersect the focus of the ellipse, authorising the use of an elliptical reflector.

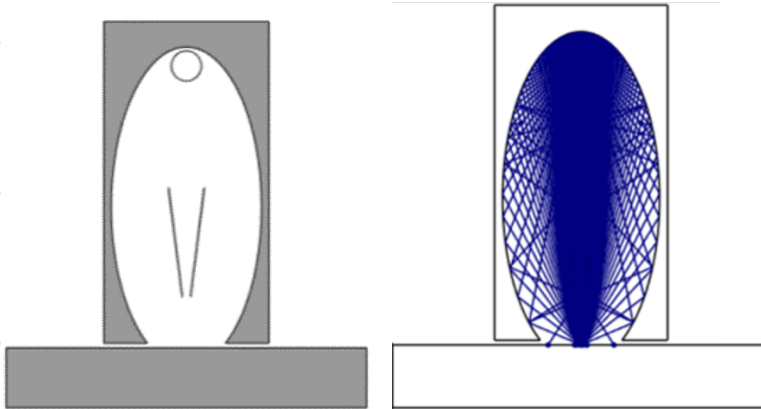


Figure 3.5: **(Left)** Optimised reflector shape established through ray-tracing simulations. The optimised heating source consists of an external reflector in the shape of an ellipse and additional straight reflectors in the middle. The halogen tube lamp is placed in the upper focal point of the ellipse. **(Right)** Ray trajectories according to ray-tracing simulation. The vast majority of the electromagnetic rays are focused in the second focal point of the ellipse. The minority that intersects with the sample outside the focal point are reflected from the additional reflectors in the heat source. The heating power coming from these rays is negligible.

3.2.3 Simulation

Designing the optimised reflector happened in multiple stages in order to divide the research into small parts. Initially, a simplified simulation model was built in COMSOL[®]. This model was used to validate all simulation parameters before starting the optimising of the reflector shape. Secondly, the ray-tracing model was combined with a batch-script to alter the parameters describing the parametric geometries. The batch-script made it possible to use parametric sweep over the parameters in order to find the reflector with the highest intensity in a pre-defined region.

The following assumptions were made in order to design an optimised geometry:

- The reflector is made of aluminium.
- The surface finish is very smooth, ensuring a reflection coefficient around 1.
- The halogen tube lamp emits electromagnetic-radiation uniform along its length.
- The heating source and reflector shape are considered to be infinite so the sides can be neglected.

3.2.3.1 Ray-Tracing Model

A 2D ray-tracing model was built in COMSOL® to find the optimal shape for a section of the reflector. A 2D simulation can be used due to the simple geometry of a halogen tube lamp. After parametrically designing the optimised section of the reflector, it can easily be extruded over the length of the halogen tube. The geometry in the simulation consists of the halogen lamp, the reflector and a specimen on which the incident radiation will be measured. Figure 3.6 shows the result of a ray-tracing simulation in ideal circumstances.

3.2.3.2 Automated Batch-Script

In order to find the optimal reflector shape, multiple shapes were examined. The curvature is described using the minor and major axis of the ellipse in order to be able to automate the exploration for the best shape. A parametric sweep is performed using a batch-script. The elliptical reflector can be described by using two parameters: the width and the height (minor and major axis). These two parameters are used during this parametric sweep. For each design, the radiation intensity is calculated in a predefined region and this value is compared to the best simulation design at that moment. The script generates a visualisation of the optimised shape, the ray trajectories and the corresponding intensities.

As a result of the focal property of an ellipse, it is necessary to assemble the heat source accurately. An additional Matlab®-script is programmed to investigate the impact of faulty assembling the optimised heat source. Multiple placement heights of the halogen tube lamp are simulated to check the error size. This error is searched for three geometries to select the most appropriate one out of the simulated designs. Those designs are also compared to three experimental heating sources. Two of them are visible in Figure 3.1. Figure 3.6 shows the output for only one placement height to compare the different reflector geometries. The benefit of the additional straight reflectors is clearly visible. Multiple placement heights are analyzed in order to investigate the impact of faulty assembly for each reflector shape.

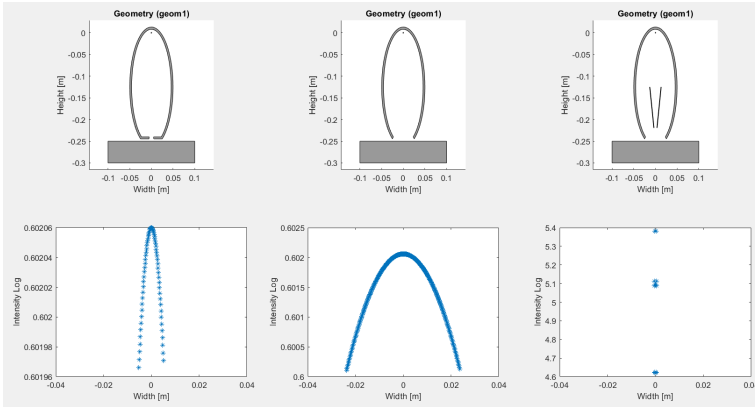


Figure 3.6: Several geometries are compared to each other. The benefit of additional straight reflectors in the optimised heating source (right) is clearly visible in comparison to the elliptical reflector shape without added reflectors (middle).

Figure 3.7 visualises the output multiple iterations of the Matlab[®]-script used to investigate the impact of a faulty assembly. The results of the optimised reflector shape are compared in order to determine how much larger the illuminated area becomes in response to bad assembly.

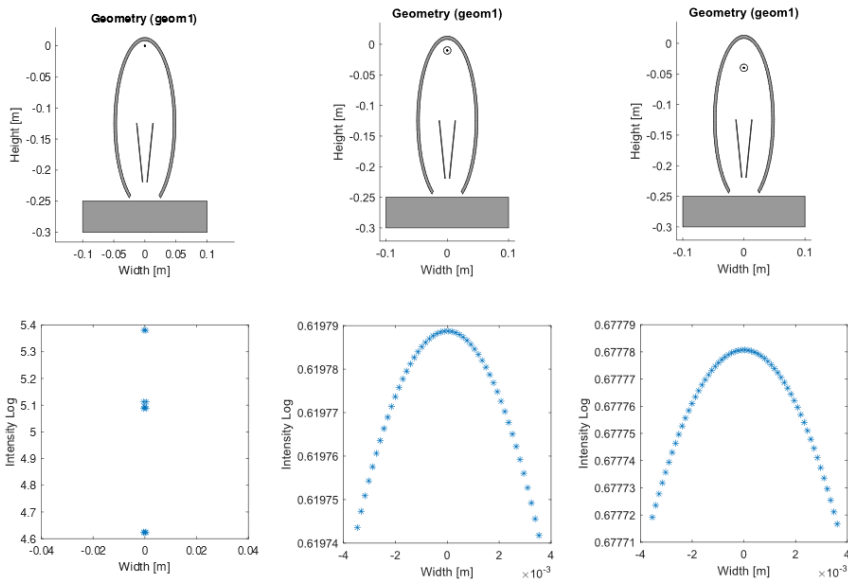


Figure 3.7: The placing height of the halogen tube lamp varies to identify the difference in heating as result of placing the lamp not exactly in the focus point of the ellipse. Faulty assembly of the heating source will result in a wider illuminated region which remains limited to a maximum of 1 cm.

3.3 Results

The result of multiple simulations is an optimised line heating source with a heated region of 4 mm wide as can be seen in Figure 3.8. Recently, our research group bought a line heater source (MES) in order to perform dynamic line thermography. We have chosen to match the dimensions of the MES-heater to the dimensions in our simulation model. This makes it easy to compare the optimised heat source to the commercially available source regarding the width of the heated region. The overall dimensions of the MES-heater are $239 \times 55 \times 125$ mm (L \times W \times H). The width of the heated region of the MES-heater is inspected using a cooled IR camera, FLIR X6540sc. According to the datasheet of the line heating source, the distance between the bottom of the housing and the specimen should be 1.5 cm. The gap is too narrow to measure the width of the heated region on the top of the object to be inspected. As an alternative, the heated region is being inspected using the IR camera in transmission: a piece of baking paper was inserted at a distance of 1.5 cm of the line heater and the camera captured the heated region. The measurement set-up can be found in Figure 3.9. The heated region of the MES line heater has a width of 1.13 cm according to the measurements (Figure 3.10). The optimised reflector on the other hand should deliver a heated width of 4 mm. One should notice that the comparison between the optimised reflector and the MES-heater only served the purpose to validate the results of the optimisation. The optimisation process, however, is generally suitable to optimise line heaters. Commercially available line heaters usually use an elliptical reflector [50, 44]. Consequently, the improvements with respect to the MES-heater should be comparable to other line heaters as well.

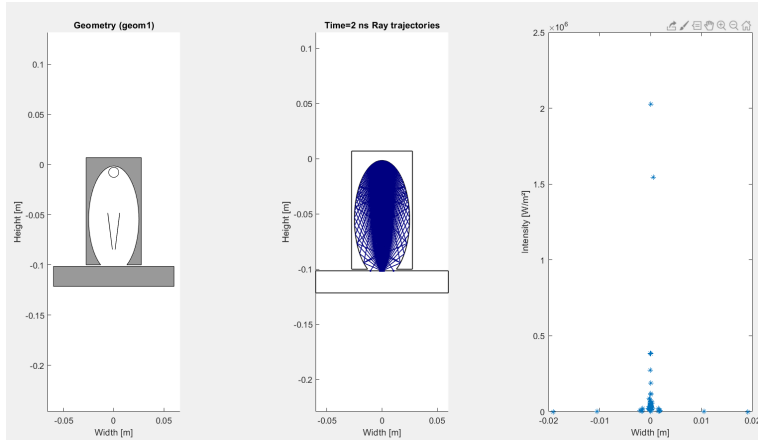


Figure 3.8: The optimised reflector shape as a result of the ray-tracing simulation can be found on the left, the rays are in the middle, and the intensity of each ray and the width of the heated region are in the right image. This reflector shape resulted in the smallest heated region and has the least adverse effects if the halogen tube lamp is placed at a non-optimal height. Other reflector shapes that were investigated are shown in Figure 3.6.



Figure 3.9: In the left picture, the MES-heater is visible in the measurement setup. The setup consists of the line heating source, a baking paper clamped between two wooden frames and the FLIR X6540sc infrared camera. The baking paper is used to investigate the heated area of the sample in transmission mode. The baking paper was placed at a distance of 1.5 cm from the bottom of the line heater as recommended in the datasheet.

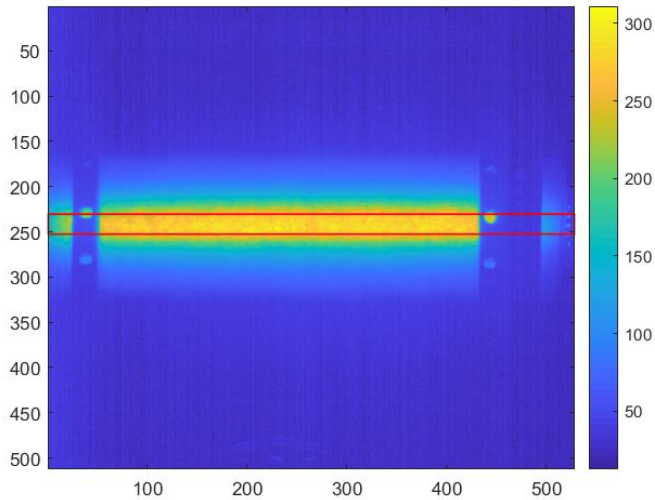


Figure 3.10: Representation of the heated region with a temperature above 250 °C. A width of 1.13 cm is calculated using a Matlab[®]-script.

3.4 Conclusions

It is possible to design a reflector in order to get a minimal heated region using an elliptical shape and additional straight reflectors. The heated region can be minimised to a width of less than 1 cm, which is similar to the heated region of a commercially available line heating source. The biggest advantage of using an optimised reflector is the ability to use widely available halogen tube lamps. An optimised line heating source is necessary in order to further optimise the process of dynamic line scan thermography. The theoretical heated region of the optimised heating source is 4 mm and the width of the commercially available source is 1.13 cm. The resulting heated region is only 35 % of the initial width leading to a better focus of the available energy and thereby a higher energy density. The MES-heater has an energy density of 44.25 [W/cm²] and the optimised heat source a density of 125 [W/cm²], which corresponds to an improvement of 282.5 %, at least theoretically. In future work, the proposed source could be experimentally developed and tested in order to compare the theoretical data with experimental data.

Part IV

Parameter optimization

DLST optimization using Response Surfaces implemented on PVC flat bottom hole plates.

The third main part of this doctoral dissertation will discuss the parameter optimization of Dynamic Line Scan Thermography using multiple techniques in several chapters. The different techniques are developed based on the desired optimization approach. Parameter optimization for detecting a specific defect is achieved using Response Surfaces (RS). This technique is well-established and therefore served as an ideal starting point to obtain insight in the correlation between the different measurement parameters. The optimization routine using Response Surfaces is explained in following chapter (chapter 4) and is published in MDPI Applied Sciences as "Dynamic line scan thermography optimisation using response surfaces implemented on PVC flat bottom hole plates" [51].

Simplified example of the Response Surface methodology:

Imagine a function $y = f(x)$ depicted by the blue line in the Figure 4.1. The objective is to approximate this blue curve using response surfaces. To achieve this, data points are sampled from the blue curve, and a curve is fitted through these points. The points are sampled at uniform intervals, with each interval corresponding to the step size between two consecutive values that the variable x can assume. The pink curve is an approximation of the blue curve that can be obtained by sampling only the pink data points. It can be observed that this approximation does not fully match the original function. On the other hand, the red curve is an approximation obtained by adding one newly sampled point, namely the red point, to the pink data points. As a result, the red curve has become a more accurate approximation of the original blue curve. As the name suggests, Response Surface Methodology uses surfaces rather than individual curves. This can be achieved by sampling in a multidimensional space instead of a 2-dimensional space.

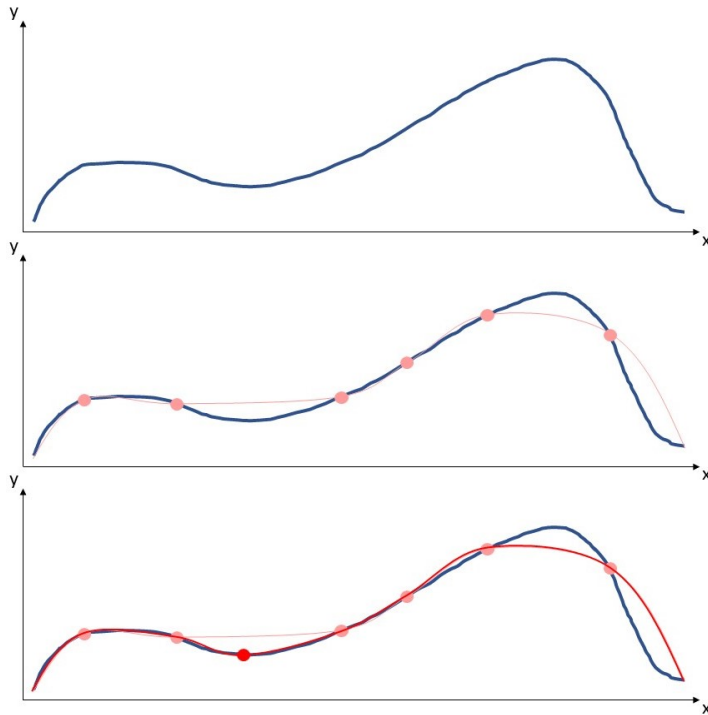


Figure 4.1: Visualisation of the Response Surface methodology. The blue function is approximated by sampling data points to learn the shape of the curve.

4.1 Introduction

Active thermography is worldwide recognised as a promising technique to perform non-destructive inspections [36]. The technology found its place in diverse domains versus before when the technique was mainly used in the aerospace industry. The main drawback of performing active thermography measurements on large samples was the fact the thermal camera or the structure had to moved in order to be able to inspect the whole object. Moving the camera or object in multiple steps is really sensitive for mistakes and therefore a solution was developed by NASA. The technique was based on the ideas of Maldague [9] and Lindberg [52] of moving the camera and heat source in tandem. When combining the heat source and the camera in a solid set-up, the heating direction, homogeneity, distance, etc are the same for every frame. Constraining the heat source and the camera together enables optimisation of the measurement set-up in an accurate way. In figure 4.2 a visualisation of a Dynamic Line Scan Thermography set-up with the most important parameters is shown.

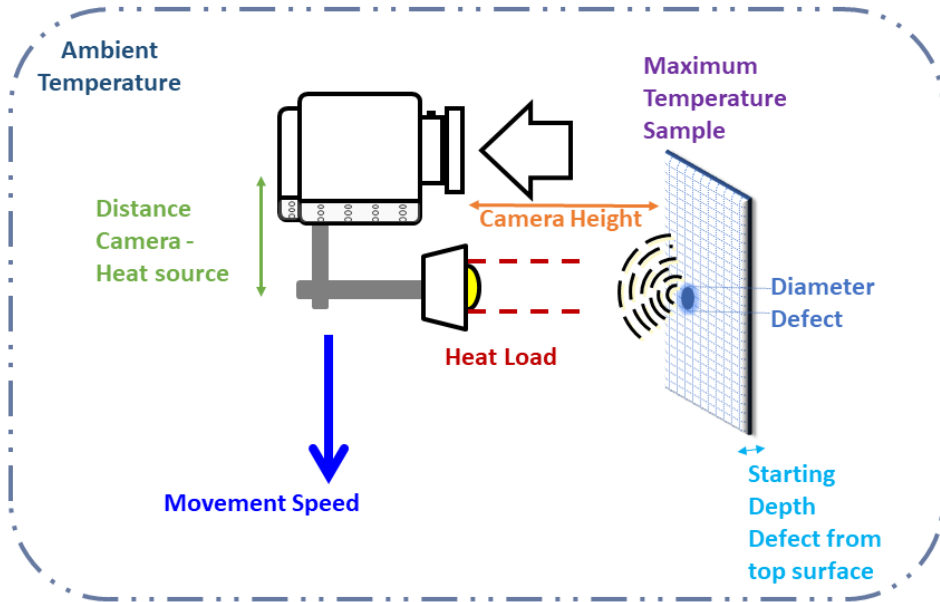


Figure 4.2: Visualisation of a Dynamic Line Scan Thermography setup with the most important parameters to be optimised. The parameters in the representation are the input parameters of the response surface, except the maximum temperature is a constraint.

Several studies have been performed in order to optimise a Dynamic Line Scan Thermography set-up. Most of this optimisation research focuses on a specific use case or a specific material group [53, 15, 54]. Dynamic Line Scan Thermography (DLST) is often linked with carbon fiber reinforced plastic parts used in the aerospace industry. The technique however is also used for different cases such as paper, wood, concrete, etc [55]. Optimising the measurement setup in order to inspect a certain sample results in showing that it is possible to use DLST. Peeters et al [54] used finite element updating in order to find the best parameter set for the sample to be inspected. The aim of this research is to provide a general optimisation routine based on response surfaces. Instead of performing an optimisation for a specific use case the correlation between the set-up variables and the measured contrast is investigated. Response surfaces are widely used in order to find an optimum while reducing the amount of computationally intensive simulations [56, 57, 58]. Performing optimizations using Response surfaces is used in a variety of applications [59, 60, 61, 62] and the use of response surfaces is still being optimised [63]. As can be seen in figure 4.2 there are a lot of parameters that influences the optimal measurement set-up for DLST. Some of these parameters can be hard to assess such as the defect diameter and the starting depth of the defect. During production, a person involved in the process can estimate the common properties of defects inside the object. The measurement set-up could be optimised for these estimated properties using a computationally expensive op-

timisation. If the estimations were faulty an additional optimisation should be performed, resulting in supplementary simulations. Each variation in a parameter results in the necessity to perform a new optimisation and therefore the use of response surfaces is justifiable. This chapter discusses the creation of the response surface used for the optimization and offers an explanation for the influence of every variable used. How the response surface is employed in this research is described in the second part of this chapter. Performing thermal inspections based on the optimised parameters is explained in part three.

4.2 Materials and Methods

4.2.1 Finite element simulation

A finite element simulation was created using Siemens Simcenter 3D. The simulation consists of a flat bottom hole plate with one circular cavity and a moving heat source above it. PVC flat bottom hole plates are widely used as standard testing samples for thermography applications.

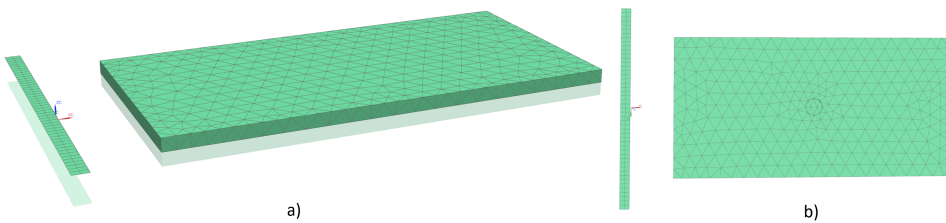


Figure 4.3: Visualisation of the finite element simulation. a) is a 3D representation from the top in order to clearly see the flat bottom hole plate and the 2D mesh for the moving heat source. b) is the bottom view of the components. The circular void is placed in the middle of the flat bottom hole plate.

4.2.1.1 Flat bottom hole plate

The flat bottom hole plate is a rectangular cuboid with following dimensions: 330 x 170 x 10mm. The dimensions are chosen in order to minimise the influence of the sides during the simulations. Edges cool down differently than the area in the middle of a sample. Since the optimisation routine focuses on dynamic measurements, a longer sample is desirable. The thickness of 10mm is chosen since it is most of the time considered as the maximum depth at which defects can be distinguished using active thermography. The dimensions of the flat bottom plate can be chosen freely since it does not influence the effect of each parameter on each other and on the contrast. Therefore the dimensions are chosen to match the dimensions of the flat bottom hole plate that is used for the experimental

Radiation	Simple radiation to environment: GBVF 1 (Gray Body View Factor)
Convection	Convection to environment: Inclined Plate, Top, Multiplier 1
Thermal Diffusivity PVC	0,08 mm ² /s

Table 4.1: Settings used in the finite element simulation.

measurements. The circular cavity is located in the middle of the plate at the bottom. The dimensions of the cavity are not fixed since these will be varied in order to create a response surface depending on the diameter and the depth of the cavity. A tetrahedral mesh is used on the flat bottom hole plate with a mesh size of 16,4mm. The material linked to the 3D mesh is PVC since this is a widely used material for testing new thermography methods. A radiation and a convection constraints are placed on the top and sides of the flat bottom hole plate since the sample lays on the bottom side. The ambient temperature is used as initial condition on the whole flat bottom hole plate.

4.2.1.2 Moving heat source

The heat source is simulated as a 2D mesh with a 'radiative heating Simulation Object' in order to mimic the heating region of a line heater. The size of the heated region is derived from the heating region of a commercially available line heater: Mehler Engineering Services [64]. The heated region has a width of 10mm at a height of 15mm above the sample to be inspected, as measured in [35]

There exist multiple approaches to simulate Dynamic Line Scan Thermography inspections. One method relies on the movement of the sample underneath the heat source. The opposite approach is to move the heat source and thermal camera over the sample to be inspected. This second method is used in the research since it is less computing intensive. The 2D mesh representing the heating region has less mesh elements than the meshed flat bottom hole plate. Each time step, the location of each moving node has to be determined and how the radiation between the heat source and the sample is affected. The movement is accomplished by using a 'Solid Motion Simulation Object' on the 2D mesh in the longitudinal direction of the flat bottom hole plate.

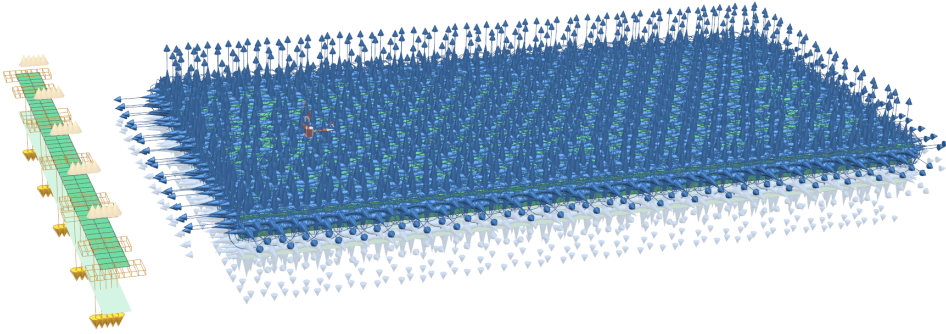


Figure 4.4: Simulation file representation including constraints and simulation objects. The radiation and convection constraint are only placed on the top and side faces of the flat bottom hole plate since the sample lays flat on the bottom surface. The ambient temperature is applied on every surface as an initial condition.

4.2.2 Response surface Parameters

In order to generate a general response surface for DLST measurements, the most important parameters are used as input parameters. The input parameters can be divided in parameters declaring the size of the defect in the flat bottom hole plate and parameters describing the measurement setup. The output parameter visualised in the response surface is the temperature difference between the temperature measured on the surface of the flat bottom hole plate above the middle of the defect and a reference temperature next to the defect. The sound area is chosen next to the defect in order to be heated at the same time as the defect. The exact location is chosen at one centimeter from the edge of the sample. Placing the reference too close to the edge of the sample will result in biased information since the side of a sample cools down differently than the region in the middle of the sample. Since the diameter of the defects is limited in the creation of the response surface, a minimal distance between the sound area and defective area is always minimal 50 mm. The temperature difference is used as the output parameter since thermographic inspections rely on the temperature contrast between defect and sound regions. Despite the temperature difference being the most important output parameter a response surface is also created from the temperature above the defect. This response surface will serve as a way to prevent the sample from reaching it's maximum use temperature.

4.2.2.1 Defect Diameter - D_{defect}

The size of a defect has a direct influence on the amount of energy being reflected towards the surface of the flat bottom hole plate. A bigger defect reflects more energy and vice versa. Figure 4.5 shows the heat propagation through material and the reflection of a heat wave on an internal defect. The energy injected in the

sample travels via conduction through the material. Therefore the energy can be seen as a thermal wave expanding in all directions. The diameter for this research varies between 6 and 50 mm.

4.2.2.2 Defect Starting Depth - d_{start}

A deeper laying defect will be less visible using active thermography than a sub-surface defect. The farther the heat wave has to travel before reflecting on a defect the smaller its energy density will be. Therefore the energy density of the heat wave reflected on the defect is strongly dependent on the defects depth. Deeper-laying defects will result in less contrast at the surface when inspected. Since the sample has a thickness of 10 the startdepth is limited to 9 mm and the minimum startdepth is 0,1 mm.

4.2.2.3 Heat Load - P_{heat}

The heat load has a direct influence on the contrast in thermograms caused by a defect in the object to be inspected. Since the induced heat has to travel through the sample towards the defect, be reflected and travel back to the surface, more induced heat will result in more reflected energy. The value of the heat load lays between 100 and 1000 W.

4.2.2.4 Source Velocity - v_{source}

The movement speed of the heating source has a dual influence on the contrast caused by the defect. On the one hand the source velocity has a connection to the available time for a specific region of the sample to be heated, on the other hand the movement pace is linked to the optimal moment to inspect the object with the infrared camera. The heat wave originating from the induced energy needs a certain amount of time to reach the defect and reflect towards the top surface of the object to be inspected. The needed period is solely dependent on the depth of the defect and on the material properties of the sample. Using an inadequate tempo will result in measuring the temperature while the heat wave has not yet reached the surface or while the heat wave has reached the surface a decent time before. The source velocity is demarcated between 5 and 20 mm/s.

4.2.2.5 Distance Between Heat Source and Thermal Camera - $d_{heat-cam}$

The second mentioned influence of the source velocity can be minimised by implementing an additional parameter: the distance between heat source and thermal camera. The optimal distance between the heat source and the thermal camera is

dependent on the movement speed of the heat source relative to the sample to be inspected and the starting depth of the defect measured from the top surface. A visual representation can be found in Figure 4.5. The optimal spacing between the heat source and the camera is the distance where the time needed for a sample section to travel from the heat source towards the camera equals the required time for the heat wave to travel through the sample, reflect on the defect and return to the surface. Equation 4.1 represents this constraint. The minimal distance is 50 mm and the maximum distance is 600 mm for this research.

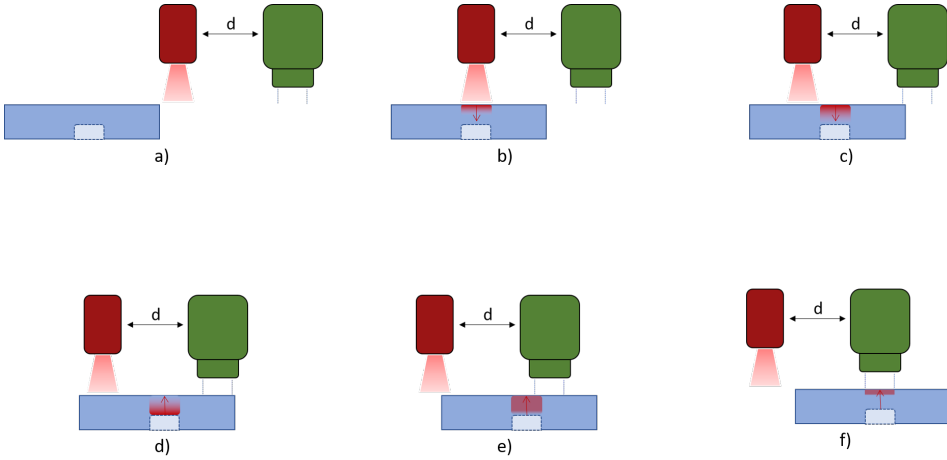


Figure 4.5: The distance between the heat source and the thermal camera has an utterly importance in maximising the temperature difference between a sound region and a defect region. The heat wave injected in the sample to be inspected needs an amount of time to reach the defect and to reflect towards the surface. This period is dependent on the depth of the defect and the material properties. A visualisation of the travelling heat wave in an optimised scenario can be seen in multiple steps starting at a) and ending in f).

In an optimised occasion the time needed for the heat wave to propagate through the sample twice is equal to the time calculated by:

$$t_h = \frac{d_{heat-cam}}{v_{source}} \quad (4.1)$$

where t_h represents the time needed for the heat wave to reach the defect and reflect to the surface, $d_{heat-cam}$ the distance between the heat source and the camera and v_{source} the velocity of the heat source relative to the sample.

4.2.2.6 Height Thermal Camera - d_{height}

The distance measured from the sensor of the thermal camera to the surface of the sample to be inspected is represented by the height of the thermal camera. This parameter has no influence on the temperature difference of the sample surface, but it is utterly important while performing thermal inspections. In order to be able to measure a defect accurately, the size of the hotspot has to be at least 3 pixels in diameter. This rule of thumb results in a correlation between the height of the thermal camera and the minimal size of the detectable defect. This parameter can be calculated using the Field Of View of the camera as well as using the focal length of the lens. In this research the focal length is used, the calculation using the Field Of View (FOV) can be found in [54].

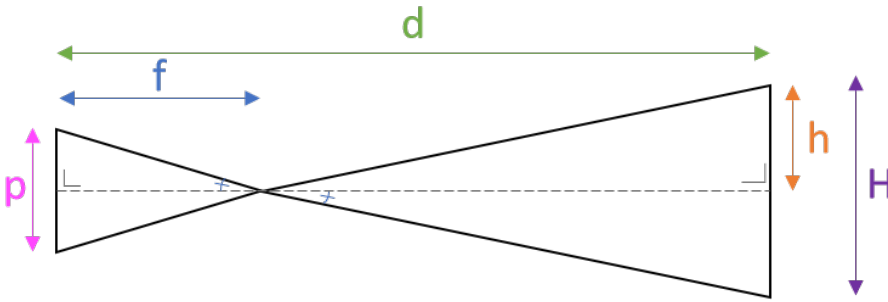


Figure 4.6: Schematic representation used to calculate the minimum defect diameter in order to be detectable for a certain camera height d . Using the detector pitch of the camera and the focal length of the lens the region recorded by one single pixel H can be calculated.

As can be seen in Figure 4.6 we can use opposite angles in order to describe the correlation between the pixel pitch p and the minimal size of a defect at a certain camera height d .

$$h = d * \frac{p}{2f} \quad (4.2)$$

with h the size of the inspected region by half a pixel, p the pixel pitch and f the focal length of the lens. Since we are interested in the dimensions of a region captured by one whole pixel the calculated size h has to be doubled.

$$H = 2 * h \quad (4.3)$$

In order to determine the minimal dimensions of a defect to be detectable at a certain camera height one should know how many pixels are needed in order to

perform a decent thermography measurement. A rule of thumb indicates that a defect has to be bigger than a square of 3 x 3 pixels, therefore the diameter of a round hole has to be at least 3 times the region measured by a single pixel.

$$D \geq 3 * H \quad (4.4)$$

Combining equation 4.2 and equation 4.4 results in following equation:

$$D \geq 6 * d * \frac{p}{f} \quad (4.5)$$

with D the minimal diameter of a defect in order to be detectable for the camera at height d_{height} above the sample to be inspected.

4.2.2.7 Ambient Temperature - $T_{ambient}$

The ambient temperature has an influence on the measured temperatures during the thermography inspections. There is no direct correlation with the measured temperature difference, but it has an utterly importance on the maximum use temperature. The higher the ambient temperature, the less power has to be added in order to reach this temperature.

4.2.2.8 Case-specific parameters

The parameters discussed above are only dependent on the characteristics of the sample to be inspected. As can be seen in [54] the image acquisition rate, framerate of the camera, and the scanning path of the inspection are not considered in this research. The framerate of the camera has no influence on the response surface since the optimal measurement moment is calculated using the distance between the heat source and the camera. The time difference between passing the heat source and the camera is calculated. Therefore the amount of frames can change accordingly to the framerate, but the time remains the same. The scanning path is not taken into account since path optimisation is tremendously dependent on the use case. Inspections whereby the width of the sample is smaller than the heat source have no need for additional path optimisation. Two dimensional inspections can be partly optimised using the parameter optimisation of this research. There will remain the possibility for further path optimisation for example by implementing the pre-heating of a sample region etc. Since these parameters are so specific they will not be taken into account for this research.

4.2.2.9 Constraints

One could think that the contrast can be maximized by using the maximum heat load and the minimum source velocity. This actually could work, however one could not call this optimising the use of dynamic line scan thermography. In order to optimise the set-up parameters, constraints have to be imported depending on the case. An utterly important constraint is the maximum temperature of the sample to be inspected since this can not reach the maximum use temperature. This constraint always remains in force, but one can imagine temporary constraints depending on the case. In mass-production environments the velocity of the sample on the conveyor belt could become a constraint as well. In this case the optimisation problem shifts from finding the highest temperature difference to finding the biggest contrast considering the minimal speed or a fixed speed. It is also possible to change the way of thinking and optimise the parameters in order to use as little power as possible. In order to have the freedom to add or remove constraints response surfaces were used in stead of an optimisation for each scenario.

4.2.3 Response surfaces

In order to preserve the freedom of adding and or removing constraints without the need of running an optimisation simulation, response surfaces are used in this research. The response surfaces were created using specialised software to perform multiple simulations, named Siemens Heeds. This software is used for design space exploration and therefore combines multiple software packages such as Siemens Simcenter 3D, Python, etc. Multiple simulations are performed using a variety of parameter sets. The output for every simulation is plotted and stored together with the parameter set and a surrogate surface is learned from this data. This surrogate will be used in order to predict the optimal parameter set based on the constraints. In order to create an accurate surrogate, 1000 simulations were performed in the complete design space. The design exploration software used in this research has the ability to draft the response surface in several ways such as Least squares linear, Least squares quadratic, Kriging gaussian, Radial Basis Function (RBF) thin plate spline and one can even program a new approximation himself. In this research RBF thin plate spline approximation is used.

4.2.3.1 Correlation table

Using the design exploration software a correlation table is created using the multiple simulations. Using the correlation table one can see interesting and unexpected correlation between several parameters. One can see a correlation table extracted from the simulations in figure 4.7.

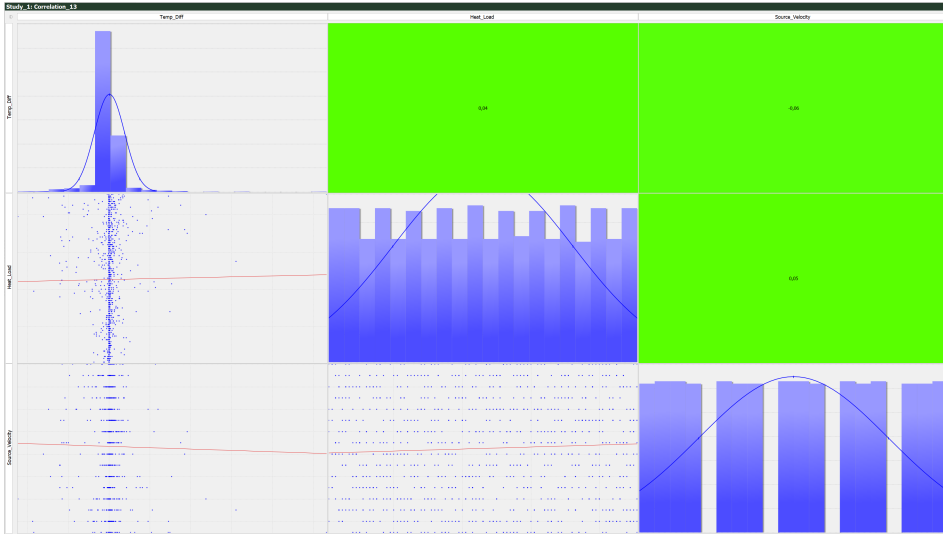


Figure 4.7: A correlation table drawn up while performing the 1000 simulations needed to create the response surface. The chosen parameters are placed on the x- and y-axis in order to get a relation between the parameters separately. The connections represented in the table are solely linearly approached, resulting in non-accurate approximations. The color of each box gives a visual representation of the correlation between the parameters. One should inspect the dispersion of the measurement points for one parameter in order to find the correlation since the linearly approximation is faulty. This visualisation focuses on the influence of the heating power in combination with the source velocity in order to predict the resulting temperature difference. A correlation table can be drawn for every parameter combination as wanted.

4.2.3.2 Simplified surfaces

It is only possible to make visual representations of 3D response surfaces, therefore only two input parameters can be evaluated regarding the resulting contrast. Since the total response surface has more input parameters than two it is not feasible to create a visual representation of the response surface. Creating the visualisations can help to understand the correlation between several input parameters. This knowledge can be useful in order to optimise a set-up where multiple parameters are fixed as a result of an already existing inspection set-up. In figure 4.8 one can see a 3D visualisation showing the influence of the heat load and the source velocity on the temperature difference for a set of fixed parameters.

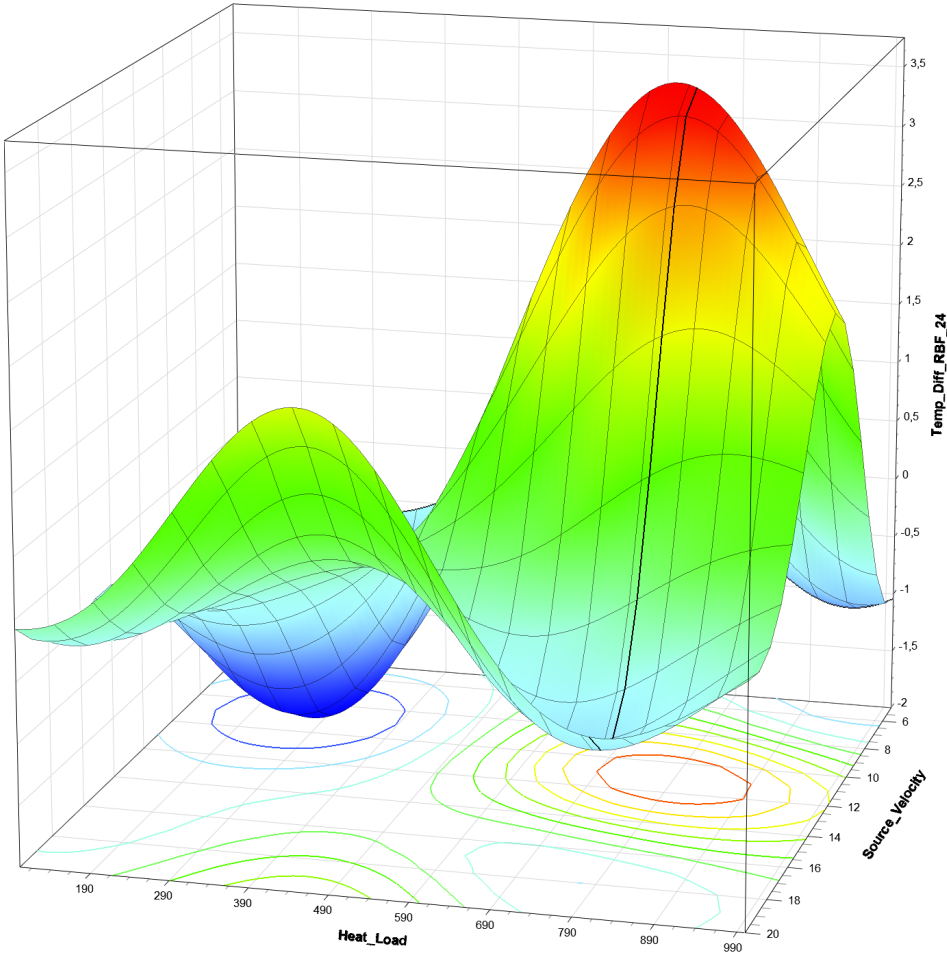


Figure 4.8: A simplified 3D response surface extracted from the eight dimensional response surface created using 1000 DLST simulations. An approximation has been composed visualising the influence of the source velocity [mm/s] and the heat load [W] on the contrast above the defect [°C]. Following values are used for the remaining parameters: $d_{heat-cam} = 425$ mm, $d_{start} = 5.8$ mm, $D_{hole} = 9$ mm, $d_{height} = 430$ mm, $T_{ambient} = 48$ °C. An ambient temperature of 48 °C is extremely high, but since it doesn't influence the temperature difference this example is chosen to show that the response surface can be created under extreme circumstances as well. One can clearly see the peak and valley in the response surface and therefore one can find a combination that results in a high contrast. It is important to notice that a 3D visualisation of a response surface only counts for the specific parameter set. One can see that the optimal case is not found for the combination of a maximum heat load and a minimal source velocity. The answer to this phenomenon can be found in the use of the temperature difference as output parameter of the response surface. Combining maximum power with minimum velocity will result in the highest surface temperature of the sample, but will not automatically result in the biggest temperature difference since the sound area is heated extremely as well.

4.2.3.3 Joint response surface

As can be read in section 4.2.3.2 it is only possible to visualise a 3D response surface for a specific parameter set of the remaining parameters. Performing the simulations a joint response surface is created for all parameters simultaneously. This approximation is exported as a Python script that describes the response surface using several parameters. A software tool is programmed in Python in order to predict the best parameter set according to the constraints provided by the inspector. The purpose of this optimisation is to maximise the temperature difference while taking the fixed parameters in account. The user has to enter some parameters in order for the script to function. The obligated parameter values are the estimated start-depth of the defect, the estimated diameter of the defect, the maximum use temperature of the sample to be inspected and the ambient temperature while performing the inspections. One can consider the estimated defect parameters as the minimal defect size and depth one wants to be able to detect. The distance between the heat source and the camera, the height of the camera, the source velocity and the heating power can be provided if they need to be fixed. Performing the inspections in line with the manufacturing process has a consequence for the parameters that can be optimised. It is not desirable to change the speed of the manufacturing process, therefore every parameter can be given as fixed. The remaining parameters will be optimised considering the given parameters. This optimization is achieved as the Python algorithm searches for the point with the greatest thermal contrast that meets the specified parameters. This search is conducted through a grid-search, where each variable ranges from the user-defined minimum value to the user-defined maximum value, with a step size that can be specified by the user. This process involves a trade-off between the speed at which one wants to obtain a set of parameters and the precision with which one wants to achieve maximum contrast. A smaller step size can result in a contrast that is slightly larger than what you would obtain with a larger step size. Since the obtained Response Surfaces exhibit continuous behavior in this study, there will never be a significantly large difference in contrast.

4.3 Results

The measurements were performed on a PVC flat bottom hole plate with a thickness of 9,8 mm and a hole pattern consisting of 12 holes with various depth and diameter. The diameters increase step by step between 6 and 25 mm: 6 mm, 12 mm, 20 mm and 25 mm. The hole depths vary between 2,5 and 8,5 mm: 2,5 mm, 5,5 mm and 8,5 mm. A visual representation can be found in Figure 4.9. Since the used measurement technique is dynamic line scan thermography, the pulse length is solely dependent on the movement velocity. The heating is initiated at the beginning of the measurement and remains until the end of the movement. While the sample moves underneath the heater, the pulse length for a specified region can be calculated using the movement speed of the sample.

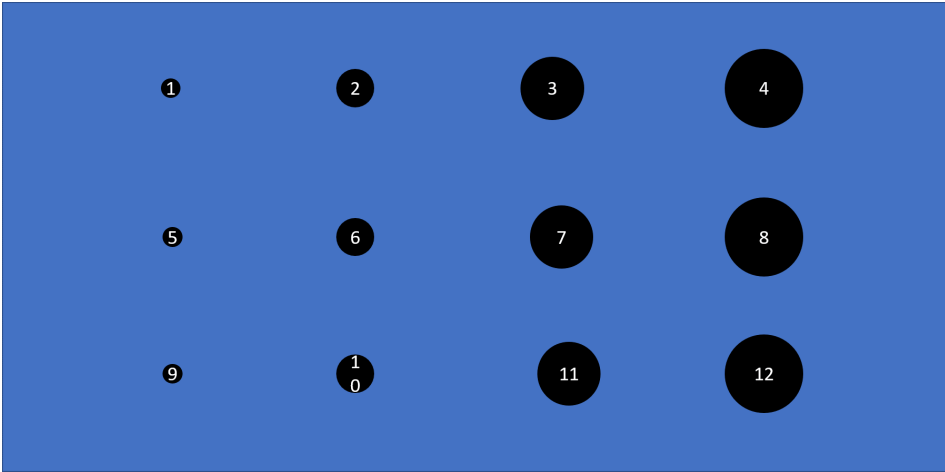


Figure 4.9: Visual representation of the PVC flat bottom hole plate with various depths and diameters. Holes 1-4 have a depth of 2,5 mm, 5-8 have a depth of 5,5 mm and 9-12 a depth of 8,5 mm. Every vertical set of holes have a different diameter starting with 6 mm for holes 1, 5 and 9. The distance between the center of the holes is 45 mm in order to minimize the influence of one defect on another.

The parameter set is optimised for hole 2 and resulted in following combination: $d_{heat-cam} = 50$ mm, $P_{heat} = 16,7$ W/cm², $v_{source} = 5$ mm/s, $d_{height} = 300$ mm, $T_{ambient} = 22$ °C, $d_{start} = 2,5$ mm, $D_{hole} = 12$ mm and Maximum use temperature of 80 °C. Optimising the parameter set for hole 2 will result in the upper horizontal row to be detectable in the inspections. The diameter difference has minimal influence on the optimised parameter set. The diameter however will determine the maximal height placement of the camera.

One could see the influence of varying the measurement set-up parameters in comparison to the optimal parameters as predicted by the response surface in Figure 4.10. Performing measurements at higher speeds without varying the rest of the parameters will result in a loss of contrasts. Placing the camera at a bigger distance of the heat source than prescribed by the optimised parameter set will result in a minor contrast loss but will majorly result in a loss of detail about the size and shape of the detected defect.

The optimal parameter set for each hole can be found in Table 4.2.

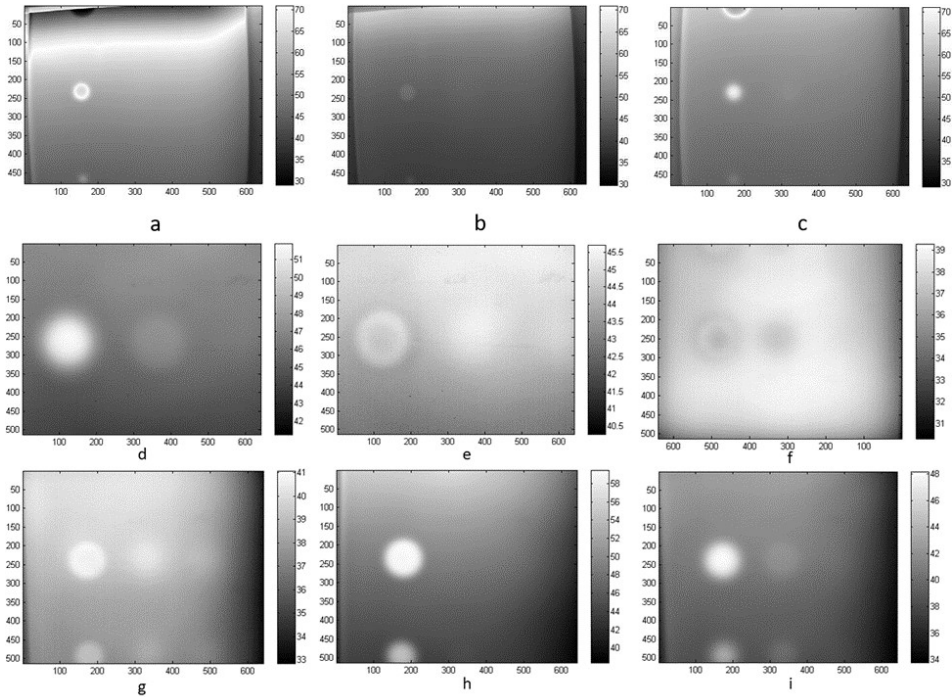


Figure 4.10: Comparison between measurements performed with alternating parameter set. The values on the x- and y-axis are pixel values and the colors represent temperatures in $^{\circ}\text{C}$. The range is fixed between 29 and 70 $^{\circ}\text{C}$ for measurements a, b and c in order to facilitate the comparison between different measurements. Image a shows the detection of hole 2 using the optimal parameter set ($d_{\text{heat-cam}} = 50$ mm, $P_{\text{heat}} = 41,7$ W/cm 2 , $v_{\text{source}} = 5$ mm/s, $d_{\text{height}} = 300$ mm, $T_{\text{ambient}} = 22$ $^{\circ}\text{C}$), image b shows the detection of hole 2 with the only difference that the inspection was performed with higher source velocity (15 mm/s) and image c shows the detection of hole 2 using a bigger distance between the camera and heat source (170 mm). As this is a snapshot taken from the DLST measurement other defects are not clearly visible in these images. The defects 1-4 were all clearly visible in the movie what can be explained by the fact that they have the same depth. Other holes such as 7 and 8 could be detected in the movie as well, but were not as clear as hole 2. Measurement d, e and f are performed on hole 8, whereby d is measured using the optimal parameter set, e is performed with a movement velocity of 15 mm/s and in measurement f the camera was placed too close to the heat source (150 mm in stead of 350 mm). The bottom row of measurements (g, h and i) are measurements performed on hole 12. Image g represents the optimal measurement where hole 12 can barely be detected. In measurement h the movement speed was 15 mm/s while the optimal speed is 5 mm/s. The difference between g and i is the difference between the heat source and the camera. The distance equals 300 mm for measurement g and 250 mm for measurement i.

Hole	Diam. [mm]	Depth [mm]	Dist. cam - heat [mm]	Heating [W]	Velocity [mm/s]	Cam. height [mm]	Ambient Temp. [°C]	Max. Temp. [°C]	Contrast [°C]
1	6	2.5	50	300	7	300	22	80	16
2	12	2.5	550	900	19	950	22	80	8.9
3	20	2.5	150	400	19	300	22	80	12.1
4	25	2.5	50	600	19	300	22	80	27.7
5	6	5.5	50	300	5	300	22	80	34.2
6	12	5.5	50	900	5	300	22	80	15.8
7	20	5.5	100	800	10	950	22	80	10.4
8	25	5.5	350	300	5	950	22	80	27.3
9	6	8.5	50	800	17	300	22	80	12.5
10	12	8.5	50	500	5	300	22	80	7.7
11	20	8.5	250	900	16	950	22	80	13.4
12	25	8.5	300	300	5	950	22	80	29.2

Table 4.2: Optimal parameter sets found for the holes in the flat bottom hole sample. The ambient room temperature is 22 °C and the maximum use temperature is chosen at 80 °C. This is not the maximum use temperature of PVC, but it limits the cooling time the sample needs before performing a consecutive measurement. Since the temperature difference is used as a measure of contrast, this limitation of the maximum temperature causes no problems. Next to the optimal parameter values for each parameter, the predicted temperature difference is calculated. This contrast is calculated between the sound area and the area above the defect.

In order to compare the contrast objectively the contrast is calculated between a pixel in the center of defect en 8 different pixels around the defect. The location of the pixels is shown in Figure 4.11. The contrast is calculated as the absolute value of the sum of the temperature difference between a pixel and the center pixel divided by 8.

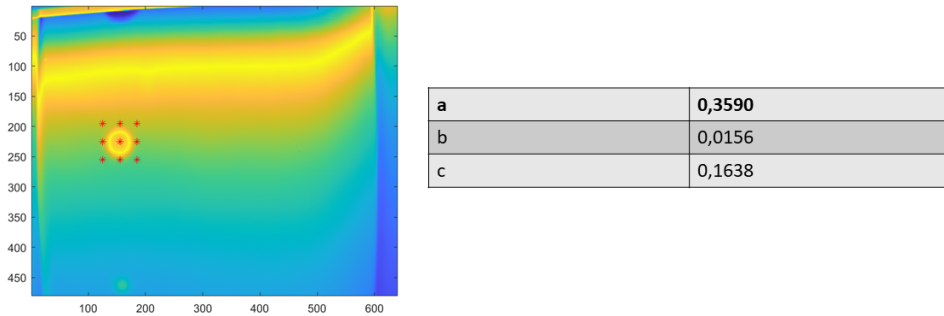


Figure 4.11: Calculation of the contrast between 9 pixels. The center pixel is situated in the middle of the defect, the other defects are spaced equally around the center pixel. The distance between the pixels is 30 pixels. The contrast values are calculated for the images a,b and c of Figure 4.10. A higher value equals a bigger contrast between the defect and the surroundings.

4.4 Discussion

The optimization routine presented in this research can offer an insight in the working principle of dynamic line scan thermography. Understanding the influence of the different parameters on each other helps an inspector selecting the most appropriate measurement set-up reducing the time needed to perform inspections. In addition it enables to perform measurements without the need of an expert skilled in the art of thermography. The optimal parameter combination can be obtained by inputting the required parameters into the software describing the Response Surface and then searching for the combination that yields the highest thermal contrast, while taking into account the specified values. In the above study, this search was conducted using a grid search, where the step size, minimum, and maximum values for each parameter can be input by the user. In further research, this search could be carried out in a more intelligent manner.

It should be mentioned that the presented technique assumes that the defects are sufficiently distant from each other. Defects near one another will influence the contrast shown in the thermograms. The influence is shown in Figure 4.12. As can be seen bigger defects experience less influence of nearby defects as the reflected energy is greater. Defects starting at different distances beneath the top surface however will minimally influence each other.

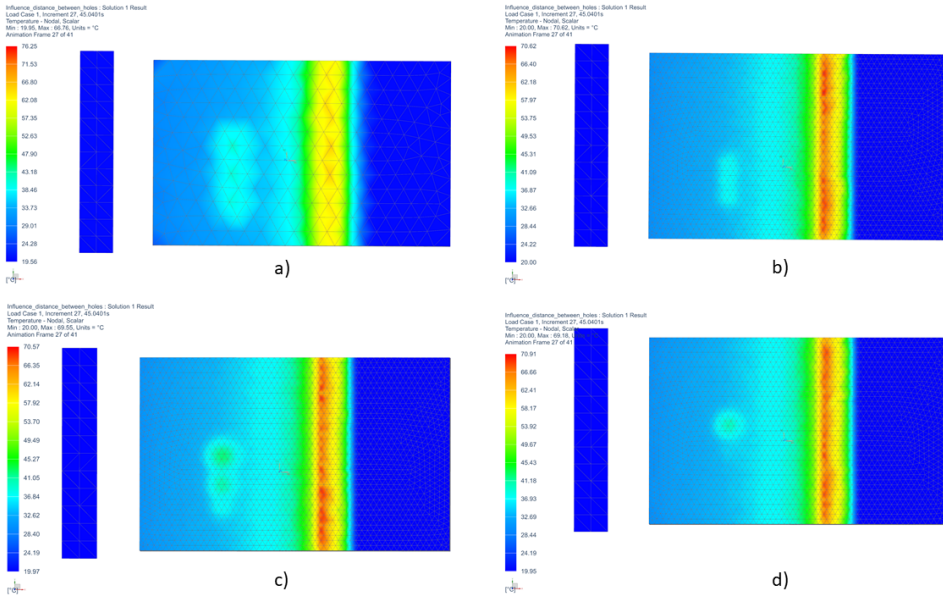


Figure 4.12: The influence of the intermediate distance between samples on the contrast is visualised in four situations. Image 4.12a) represents a simulation of three defects with a diameter of 25 mm, a depth of 5 mm under the surface and an intermediate distance of 27 mm between the centers of the defects. The heat reflected by the defects influences each other resulting in a reduction of the contrast between the separate defects. The resulting hotspot is bigger than the area of the defects. Visualisation 4.12b) represents a similar simulation performed on defects of 12 mm diameter, starting 5 mm underneath the top surface and at an intermediate distance of 15 mm of each other. The heat reflected by the separate defects influences the contrast making it impossible to distinguish the defects. Smaller defects however reflect less energy in comparison to bigger defects making it harder to detect them. Multiple small defects close to each other will show as a bigger defect, but with more contrast than the individual defects. Defects of different diameters are simulated in figure 4.12c) where the intermediate distance is 25 mm between the defects. The defects have a diameter of 25 mm, 20 mm and 12 mm. The two bigger defects can still be distinguished from each other. The smallest defect however shows as a part of the other defect. Figure 4.12d) shows the influence of defects placed at different starting depths from the top surface. The defects all have a diameter of 25 mm and are placed at a depth of 5 mm, 10 mm and 15 mm underneath the surface. Since the heat wave requires a specified amount of time to reach the top of the defect and reflect to the top surface, the different defects will not result in hotspots at the same moment in the inspection. Therefore the influence of deeper defects will affect the top defect minimally. Deeper defects however will be less visible to detect because of the hotter regions caused by defects above. The defects closest to the surface will not have the biggest contrast since the parameters are not optimal, but they will still remain hot, disturbing the detection of defects at a greater distance from the top surface. This occurrence makes a flat bottom hole plate with defects at different depths not the most suitable test case.

4.5 Conclusion

Performing dynamic line scan thermography measurements is a difficult task without consulting an expert. The various parameters have an impact on each other making it challenging to estimate the correlation between one and another. Using a response surface however it is possible to find the best parameter set based on the defect parameters such as diameter and depth beneath the inspected surface. The algorithm to find the optimal parameter set focuses on maximizing the temperature difference between the area above the defect and a sound area. In order to prevent the sample from overheating a maximum use temperature can be given as input parameter next to the defect parameters and the ambient temperature. The resulting parameter set consists of following parameters: Defect Diameter D_{defect} , Defect Starting Depth d_{start} , Ambient Temperature $T_{ambient}$, Maximum Use Temperature, Heat Load P_{heat} , Source Velocity v_{source} , Distance Between Heat Source and Thermal Camera $d_{heat-cam}$ and Height Thermal Camera d_{height} . Measurements performed with an optimized parameter set result in good contrast in a fast way. Differing from the optimised parameter set will result in contrast loss and even losing the possibility to detect the defects. This chapter only focused on the creation of a response surface for DLST measurements on PVC samples since this is the standard testing material for thermography.

DLST optimisation: comparison Reinforcement Learning and Response Surfaces.

The second optimization approach used during this research is based upon the idea of finding a variety of defects in a sample in the least amount of measurements. The development of this technique is described in chapter 5. The optimization is accomplished using Reinforcement Learning (RL). This machine learning technique is based on self-learning of the computer algorithm in order to find the most suitable parameter combinations. A virtual environment is created in order to mimic the DLST measurement setup with the parameters to be optimized.

Simplified example of the Reinforcement Learning methodology:

Behold once again the blue curve describing a function $y = f(x)$. The blue curve is approximated by sampling data points selected by the 'reinforcement learning agent'. This is a part of the algorithm that is being trained to select adequate data points. There is a restriction on the number of data points that can be sampled, such as in this example a maximum of 6 data points. At the beginning of training, these points are randomly chosen, but as the training progresses, the goal is to train the agent to select the points in a more targeted manner. The pink curve is an approximation through a set of points selected at the beginning of training. One can observe that this curve does not provide a very good approximation of the original blue curve. The red data points are chosen by the reinforcement learning agent after training and result in a better approximation of the original function. In this example, a 2D curve was used, but in the further discussed research, these curves are replaced by surfaces.

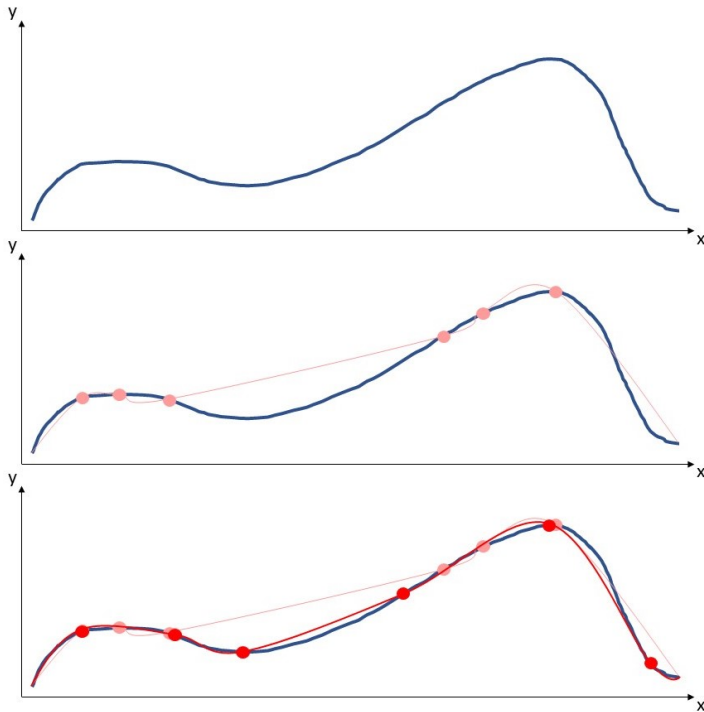


Figure 5.1: Schematic visualisation of the working principle of the Reinforcement Learning Methodology as described in this thesis. The blue curve is approximated by sampling data points that are chosen by the agent.

5.1 Introduction

Since artificial intelligence is growing exponentially worldwide, it was only a matter of time until it found its way in thermography. Nowadays the combination of thermal images and artificial intelligence (AI) is mostly found in biomedical applications such as detecting cellulite [65], breast cancer [66, 67, 68] and Carpal Tunnel Syndrome Diagnosis [69]. Dos Santos et al. [70] however used AI in an industrial setting inspecting electrical transformers. It is commonly known that the biggest issue using AI is the large amount of training data that is required to create a reliable and robust network. Gathering so much thermal data is very time-consuming and can be utterly expensive. Training a neural network requires data of different situations that can occur in order to teach the network the possible features it has to detect. In order to generate thermal data, it is necessary to produce the needed samples and perform measurements on them. Manufacturing samples and specifically carbon fibre samples just for the sake of training a neural network is expensive and not environment friendly. A well-known alternative to thermal inspections is the use of finite element simulations. Creating a thermal simulation

minimizes the needed cost and time to analyse the thermal response of a defect in an object to be inspected. Performing simulations enables to investigate multiple situations that can occur at the same time. Several researches have been performed on optimizing numerical models in order to mimic the real life situation as much as possible [54]. Performing simulations is less costly than performing actual measurements, but it also has a major drawback considering artificial intelligence. The result of a thermal simulation can approach the numerical result of a real measurement, but it will not show as a real thermogram. The goal of this chapter will focus on creating thermograms using finite element simulations and using them to train a reinforcement agent to find the optimal parameter set for a measurement. Reinforcement learning is gaining interest in optimisation routines since the agent could bring possible solutions forward of which a person would not think. Sato et al. [71] used reinforcement learning to optimise the designs for electrical machines. The first section handles the finite element simulation, afterwards the link between the finite element simulation and Mathworks® MATLAB as optimisation tool is explained. The third section handles the reinforcement learning process and finally a comparison is made between the use of reinforcement learning and response surfaces for parameter optimisation.

5.2 Finite Element Simulation

5.2.1 Finite Element Model

A thermal simulation is created in Siemens NX and consists of a flat bottom hole plate with following dimensions: 265 x 165 x 15 mm. The holes vary in diameter and depth as can be seen in Figure 5.2. Flat bottom hole plates out of PVC are often used as a reference material in thermography to verify new methods and ideas. The simple geometry and material parameters enable the possibility to compare new techniques to already existing ones.

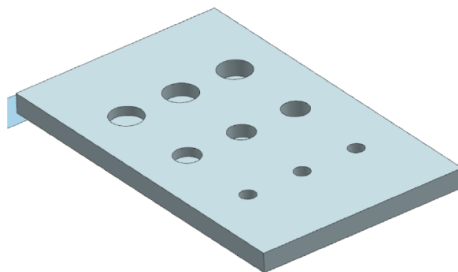


Figure 5.2: Flat bottom hole plate used in the thermal simulations. The diameter gets smaller from left to right: 25 mm, 20 mm and 12 mm. Every diameter has three different depths starting at 12.5 mm, the second depth is 10 mm and the third is 7 mm.

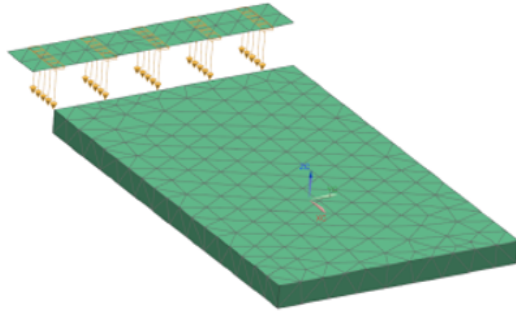


Figure 5.3: FEM-model of the flat bottom hole plate. The holes are positioned on the bottom of the sample and the sample is heated from the top. The plate is meshed in a 3D tetrahedral mesh. The heating source is meshed in a 2D mesh.

In the figures above a visualisation of the flat bottom hole plate as used in the finite element simulation can be seen. Figure 5.2 is the representation of the bottom of the flat bottom hole plate. The sample consists of a PVC plate with holes varying in size and depth. In Figure 5.3 the meshed plate and the heating source can be seen from the top.

The workflow can be used with any finite element simulation but for this research a dynamic line scan (DLST) simulation will be used. The simulation is build in analogy with the simulation used in [51]. A 2D meshed line heater moves above the top surface of the sample. The heating load is connected to the moving line heater to create a DLST simulation.

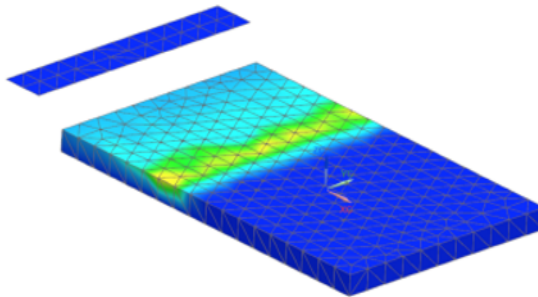


Figure 5.4: Dynamic Line Scan Thermography simulation during movement of the heating source. The sample can be divided into three parts: the cold region (dark blue) has not been heated yet, the region that has been heated and is cooling down (light blue region) and the region right beneath the heating source (yellow region).

The initial temperature is set on 20 °C. In order to create a dynamic simulation a transient solution is used. Since the length of the sample is fixed, the simulation time can be calculated out of the moving velocity of the heating source using following formula:

$$heatingTime = \frac{length[mm]}{velocity[mm/s]} \quad (5.1)$$

It is not possible to use the heatingTime as the total simulation time since this only accounts for the time that the heating source moves. The total simulation time consists of the heatingTime and coolingTime in order to minimize the influence of the heating source in the last simulation step. The coolingTime can be calculated as follows:

$$coolingTime = 10 \log\left(\frac{heat[W]}{velocity[mm/s] * \theta[W/mm]}\right) \quad (5.2)$$

θ represents the thermal resistance which can be calculated using the thickness, thermal conductivity and area of a sample. The thermal resistance in this case means that for every millimeter of thickness, the material resists the flow of heat with approximately 1.71 watts.

$$\theta = \frac{0.015[W]}{0.2[W/(m.K)] * 0.165[m] * 0.265[m]} \approx 1.71[W/mm] \quad (5.3)$$

If a large heating power and a small velocity is combined, longer cooling time is needed and vice versa. Therefore a logarithm is used for the calculation of the coolingTime. The total simulation time can be calculated as the sum of the heatingTime and the coolingTime using equation 5.4.

$$endTime = \frac{length[mm]}{velocity[mm/s]} + 10 \log\left(\frac{heat[W]}{velocity[mm/s] * \theta[W/mm]}\right) \quad (5.4)$$

5.2.2 Expressions

Since artificial intelligence requires an enormous amount of data it is not desirable to create a finite element simulation for every defect possible. In order to automate the simulating process 'Expressions' are used in the finite element simulation. 'Expressions' can be linked to simulation parameters in order to bundle all the needed variables in one place. The variables used in the simulation are heating power and source velocity. The variables endTime, heatingTime and coolingTime are then calculated. The advantage of using 'Expressions' is the fact that you can change dimensions, constraints and loads without the need of really editing the simulation. The expressions used for this research are visible in Table 5.1. Since the flat bottom hole plate in this research consists of a PVC plate with a variety of indentations, the parameters defect diameter and starting depth of the defect are excluded. The parameter camera height is not included either since the diameters of the defects are fixed on values that cover a 3x3 pixel grid in the range of camera

cooling	10log(heat/speed*1000000*thermal resistance))	65.26	s	Time
EndTime	(width/speed)+cooling	85.64		Unitless
heat	25.5	25.5	W	Heat Flow Rate
speed	13	13	mm/s	Velocity
TimeStep	EndTime/40	2.14		Unitless
width	265	265	mm	Length
thermal resistance	1.71	1.71	W/mm	Thermal resistance

Table 5.1: Expressions used in the thermal simulation. One can see the created variables heat, speed, endTime, coolingTime and heatingTime with their corresponding values and units.

heights. The ambient temperature could easily be added as an input parameter, but since the purpose of this research is to determine whether it is possible to detect all defects in the least amount of measurements, the ambient temperature should remain constant within the consecutive trials. Therefore there is no benefit in adding the ambient conditions as an input parameter. The distance between the camera and the heating source is discarded since all data from every mesh node is used to detect the defects. Therefore the distance has no influence on the detectability.

5.2.3 Journal File

The use of expressions facilitates editing a simulation in an efficient way. However it does not enable to perform simulations automatically. It is possible to write a dedicated script to handle the automated simulations, but Siemens NX offers a solution for the automation. In Siemens NX it is possible to use a 'Journal File', what can be described as an intelligent macro. The user records all necessary actions once in order to create the 'Journal File'. The 'Journal File' is automatically created in Visual Basic and consists of every step performed by the user. Afterwards the created file can be used to perform automated simulations. The file created for this research consists of four distinguishable parts: editing the expressions, solving the simulation, exporting the results to a CSV-file and saving the simulations followed by closing it. Each simulation starts with adjusting the parameters to the desired values using the expressions. Thereafter the simulation is updated and solved to generate results for the desired situation. Since the simulation is transient the results will be generated for each time step in the process.

5.3 Matlab

The 'Journal File' can be executed from the command line using the command in equation 5.5. The variables heat and speed are changed in order to create thermograms as if they were generated using different measurement parameters. The variables SoftwarePath, JournalFile, GeneralFolderPath and Map are used to

refer towards the proper places of the journal file, the simulation file and the location where the CSV-files should be saved.

$$cmd = sprintf('"%s" "%s" - args "%f%f" %s%s"', SoftwarePath, JournalFile, heat, speed, GeneralFolderPath, Map); system(cmd) \quad (5.5)$$

5.3.1 Result Sampling

Since the simulations in this research are transient, a CSV-file is exported for each time step in the simulation. Each time step the temperature for all mesh points is calculated and the heating source is moved. It can be compared to the frame rate of a camera. The lower the frame rate the longer the time between two consecutive frames. In order to create a sequence of thermogram, multiple images have to be created using the CSV-file from different time steps. Inspecting a number of successive thermograms enables performing post-processing in order to detect defects in an object. Air voids or other defects will affect the cooling down of an object resulting in hotspots where the defects are located. As the simulation time is influenced by the movement speed of the heating source, the number of time steps is also dependent on the movement speed. In order to investigate every thermogram it is necessary to process all time steps generated by the simulation. For each time step a table is generated from the CSV-file. This table consists of the X,Y and Z location of a node in the finite element model and the corresponding temperature of that node at that moment.

5.3.2 Top Surface Filtering

Performing active thermography inspections, the top surface of a sample is recorded in order to detect the temperature change of the surface. Finite element simulations consist of 3D elements and the temperature of the whole object is calculated. In an effort to create thermograms the top surface of the 3D object has to be filtered out of the data points. The simulation exists of a flat bottom hole plate and a 2D meshed heater that moves above the plate as explained in [51]. In order to filter the top surface out, the nodes with the highest z-values are removed from the results. These nodes represent the line heater and are therefore not desirable in the results file. The second highest set of z-values correspond to the top surface of the flat bottom hole plate. Consequently the corresponding x, y and temperature values for these z-values are used to create the top surface as a 2D thermogram.

5.3.3 Top Surface Resampling

Finite element simulations require meshed objects for their working principle. The element size of a mesh influences the accuracy of the results as can be seen in [72, 73]. On the other hand there is a strong correlation between the mesh size and the solve time of a simulation. Smaller mesh sizes typically resolve in more accurate results, but at the cost of longer simulation times. Performing a convergence study however it is possible to find the minimal mesh size after which the result does not improve despite shrinking the mesh size. When generating large datasets it is desirable to keep the simulation time as low as possible. Therefore the mesh size found in the convergence study is used. Thermal cameras on the other hand have a certain resolution. In favor of creating simulated thermograms as close as possible to real thermograms, the resolution of thermal cameras needs to be mimicked. The filtered top surface from section 5.3.2 has a resolution depending on the amount of mesh nodes in the simulation. The temperatures of the top surface are interpolated and then resampled to resemble the resolution of a thermal camera. The resampled thermogram is compared to the result view of the finite element simulation in Figure 5.5.

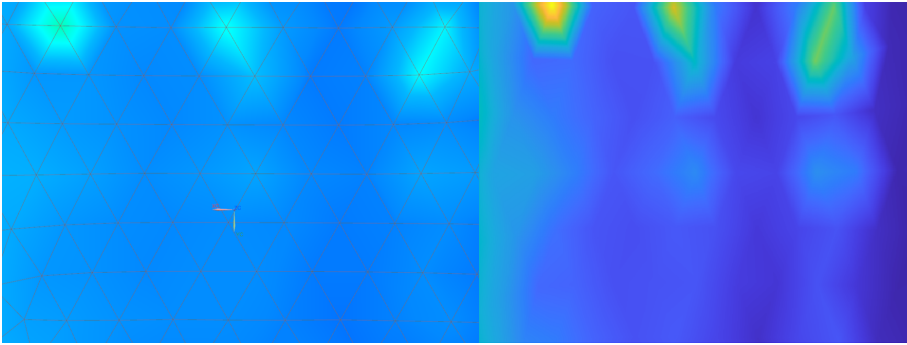


Figure 5.5: A comparison between the visualisation in the finite element simulation (left) and the thermogram provided by the processing algorithms (right). The holes can be detected in both the images, however the resampled top surface is more suitable for AI training data. Due to the interpolation, the edges of the mesh elements are not visible and therefore the neural network algorithm will not be affected by them.

5.4 Reinforcement Learning

Generating data for artificial intelligence applications is time-consuming and can be very expensive since every possible occurrence of parameter combinations has to be recorded. Multiple samples have to be manufactured, heated, recorded and in between measurements the sample has to cool down to its surroundings conditions. By the use of finite element simulations the cost and time required to produce data for one specific case can be minimized as can be read in [54]. This research focuses on creating training data for reinforcement learning automatically out of finite element simulations.

Reinforcement learning is a subdomain of artificial intelligence where the model learns how to react on the environment. The agent, the computational entity or program that is responsible for decision-making, gathers knowledge of the environment in which it works through trial and error at first. The environment exists of the possible actions the agent can perform, called action space, and the observations that are carried out, the observation space. For this research the possible actions are the parameter values that can be chosen in analogy with the parameters in [51]. The main objective of the reinforcement learning agent is to find the best parameter set to detect as many defects as possible in the flat bottom hole plate in the least amount of measurements. The best decisions are saved and thereby the agent becomes smarter with every attempt. In order to distinguish a bad from a good attempt a decent reward function has to be declared.

	Amount of episodes	Defects detected
Q-learning agent	800	8 or 9
Deep Deterministic Policy Gradient agent	400	7
Policy Gradient agent	400	8
Policy Gradient with Baseline agent	400	9

Table 5.2: Comparison of different training methods applied in this research. The policy gradient agent with baseline performed the best for this application.

5.4.1 Reward

For this research the reward is a combination of the amount of steps/tries the agent performs and the amount of holes it detects. For each try a point is deducted in order to train the agent to perform as little steps as possible. The amount of detected defects functions as a reward since the best parameter set ensures to find the largest amount of defects in the least amount of measurements. Using the resampled images from Section 5.3.3 the holes can be easily counted after creating a binary image.

5.4.2 Training

The creation and training of the agent is performed in Matlab using the Reinforcement Learning Toolbox. The training algorithm used in this research is the policy gradient agent. This method provided the best and fastest training sessions with eventually a convergence to the maximum number of defects as can be seen in Table 5.2. In order to train the agent, the reinforcement learning episode manager is used. The training parameters were optimised and resulted in a policy gradient agent with baseline, entropy weight loss = 1, discount factor gamma = 0.3 and sample time = 0.05. These parameters were found by conducting various training sessions, carefully examining the influence of each parameter. Multiple values were used for each parameter in order to find the most optimal one. The training outcome is visualised in 5.6. Each training episode existed of maximal 60 steps, in other words the agent can try 60 possible parameter combinations in every episode. After every episode the policy is evaluated and if necessary adjusted by the agent. In this research an average of 400 episodes was needed to find the maximum amount of holes in one episode. The agent learned what combinations of parameters needed to be used consecutively in order to find all nine holes in the flat bottom hole plate.

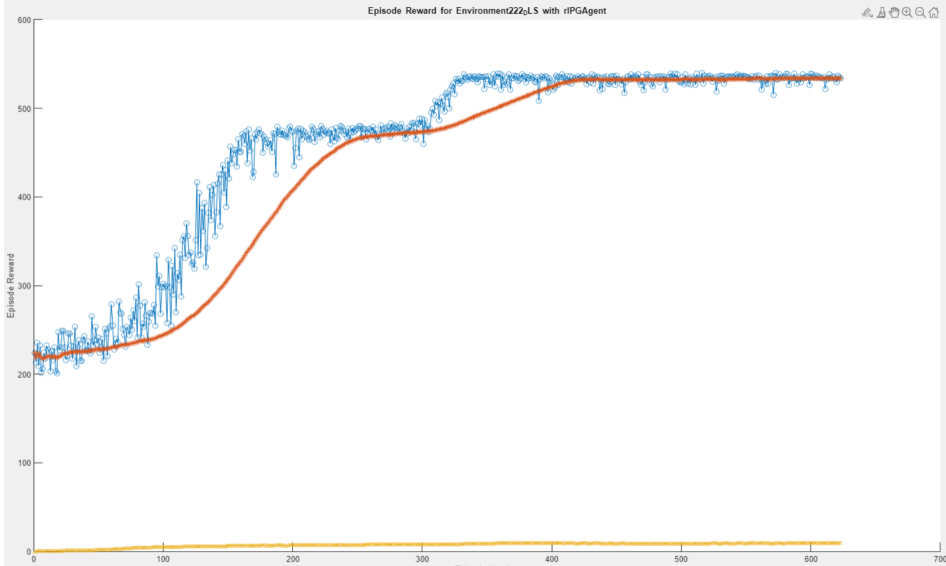


Figure 5.6: Screenshot of the Matlab Reinforcement Learning Episode Manager. The yellow line represents the value of the baseline, the red line is the average reward and every blue point is equal to the episode reward. This Matlab tool is used during the training of the agent in order to inspect the improvement. The vertical axis represents the reward received during the training and the horizontal axis equals the amount of episode numbers needed.

5.5 Discussion

It is possible to use reinforcement learning in order to train an agent to find the holes in a flat bottom hole plate. Using a policy gradient agent with baseline resulted in the best outcome and is able to find all nine defects in the sample to be inspected. In comparison to the optimisation paper of Verspeek et al. [51] the agent is not trained in finding the best parameter combination for one specific defect. The agent is trained to find all defects in the least attempts possible. In order to find the best parameter sets in order to detect all nine holes, the agent needed 400 episodes consisting of 60 steps each. In total 24 000 attempts needed to be performed in order to train the agent. Optimizing the parameter set using response surfaces as written in previous work [51] took 1000 simulations to create the response surface. Once this approximating surface was created, the optimal parameter set for each defect can easily be found. One step for the reinforcement learning consists of performing a finite element simulation and detecting the amount of visible holes and thus takes minimum the same amount of time as an individual simulation during the creation of a response surface. Therefore it is faster to create a response surface for the parameters of DLST in comparison to training a reinforcement learning agent.

5.6 Conclusion

The goal of this chapter was to investigate how thermograms could be generated from finite element simulations in an optimal manner. Using expressions, the simulation file can be changed without opening the finite element software. The results produced by the finite element simulation are exported automatically for each time step making it possible to distinct a thermal image sequence. In order to visualise the data as a thermogram, the 3D result data from the simulation need to be processed in order to create 2D thermograms. These generated images can be used as learning data for artificial intelligence applications in a cheaper and faster way than performing real thermal inspections. It is possible to train a reinforcement learning agent to find the optimal parameter set for DLST. However it is faster and more reliable to create a response surface using simulations. Future work will investigate the use of gaussian processes compared to the use of response surfaces.

Thermography Parameter Design via Gaussian Process Emulation

The following chapter elucidates the use of Bayesian emulation to perform parameter optimization. This technique has the benefit of performing optimization based on a limited amount of data. Moreover this technique is capable of providing answers to multiple relevant industrial questions. Chapter 6 is published in MDPI Algorithms as "Dynamic line scan thermography parameter design via Gaussian process emulation" [22].

Simplified example of the Bayesian Emulation methodology:

Behold the blue function $y = f(x)$ one last time. In Bayesian Emulation, an approximation is formed by intelligently selecting data points for sampling. With each sampled data point (pink points), one obtains an uncertainty interval for the regions between two consecutive sampled points (pink regions). These colored regions represent all the possible curves that can be formed by these sampled points. The further the curves are from the original blue curve, the greater the uncertainty in that area. The next data point is chosen at the location where the uncertainty is greatest, and a new approximation is formed using the sampled data points. By sampling in this manner, it is possible to form a good approximation of the original curve in a faster and more efficient way. This approximation is represented by the red curve, which is formed by sampling the red points. Once again, this example used a curve, but this technique can also be extended to higher-dimensional spaces.

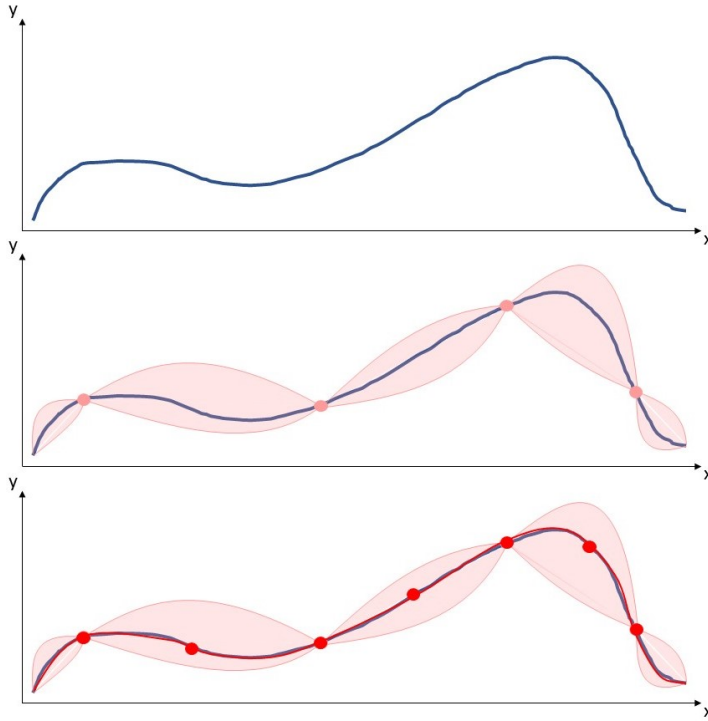


Figure 6.1: Visualisation of the Bayesian Emulation methodology. The blue curve is approximated by sampling data points in a smart manner based on the biggest uncertainty.

6.1 Introduction

Active thermography is widely recognized as a fast, reliable and contactless non-destructive inspection technique. It can be performed in a stationary manner in which the sample to be inspected remains at the same location. This way the object is easily heated using a heating source and the cooling down of the sample is registered using a thermal camera. This method limits the size of the object since the sample has to fit in the field of view of the camera. It is possible to examine larger samples by placing the thermal camera at a greater distance of the sample. The downside of placing the camera further away of the sample, is the resolution reduction in a specified region. In order to detect a defect with sufficient certainty, the defect has to have an area of at least 3×3 pixels [51]. Larger samples can be inspected using dynamic line scan thermography (DLST). This technique uses a heat source and a thermal camera in tandem, which moves relative to the sample to be inspected. This can be achieved in two ways: either the camera and heating source are moved above the object using a robotic arm, or the specimen can translate on a conveyor belt underneath the heating source and the camera

[74]. Since dynamic line scan thermography is a relative new technique, it is less widely spread in comparison to other nondestructive testing methods.

An expert skilled in the art has to define the DLST measurement parameters in order to prevent time-intensive trial and error attempts to find a workable parameter set. In this work, we focus on the movement velocity, the distance between the heat source and the camera, the heating power, the start depth of the defect, the diameter of the defect, the height of the camera and the ambient temperature.

Several studies have been performed in order to simplify the search for these DLST measurement parameters. Finite element simulations have been used in order to update the parameters according to measurements. Response surfaces are used as approximation in order to find the best parameters based on the characteristics of the defect (depth, dimension) and the thermal properties of the material [51]. Using the response surface and some fixed parameters provided by the inspector of a specimen, the best matching set of parameters is predicted. A response surface can be generated using data from multiple measurements. However, in order to create such a response surface, a large amount of measurements are needed. Generally, this is a time-consuming and costly endeavour. Therefore, a response surface is often built from data gathered in multiple finite element simulations. The amount of simulations matches the amount of needed measurements, nonetheless performing simulations is cheaper cost-wise and time-wise. The simulation performed for this manuscript consists of a flat bottom hole plate heated by a line heater moving above the sample. The simulated object is a flat bottom hole plate since this is widely used in scientific research on thermography. The thermal behaviour of flat bottom holes resembles best the response expected by most defects whereby active thermography is used as inspection method. Such defects are delaminations, lateral cracks, areas of porosity, etc. Attempts are made to create a standard for thermal imaging based on the use of flat bottom hole plates [75, 76]. Therefore this research is limited to flat bottom hole plates. However a flat bottom hole plate does not resemble above-mentioned defects, therefore further validation of the proposed research is needed.

A different approach to predict an optimal parameter set, is to use artificial intelligence. For instance, it is possible to train a reinforcement agent to search for the best parameters to detect multiple defects in a flat bottom hole plate. However, training the reinforcement learning algorithm required more simulations than generating the response surface and therefore is less interesting.

Computer simulations are used in a wide range of scientific and engineering challenges [77]. In this work we follow their definition of a simulation, stating that it is any computer program that imitates a real-world system or process. Being able to simulate an experiment instead of actually conducting it in the real world, greatly reduces the required time, cost and other and practical implications such as possible health risks or consequences for the environment.

However, since simulators are programmed to a specific task, they are not insensitive to bias. Moreover, for more complex simulators, the amount of time needed to

run the simulations can become cumbersome. In order to overcome these drawbacks, the simulation itself can be modelled by a machine learning algorithm, which predict the outcome of the simulator. Popular choices for these models are Gaussian processes [78], random forests [79] and neural networks [80]. In this sense, the emulator is a 'model of a model'. The gain stems from the fact that a complex simulation is much more computationally expensive than a computationally cheap emulation. Over the past years, emulation has found its way in several domains. In [81], a Gaussian process was implemented to emulate a mechanical model of the left ventricle, which allowed for a more rapid discovery of the optimal parameter set for the design. The authors of [82] build an emulator to model to calibrate an engine. The spread of an infectious disease was modelled in [79].

For machine learning models that are probabilistic by nature, they serve as a statistical surrogate model. This allows for the quantification of uncertainty of their predictions, which plays an important role in decision making or risk assessment. For this reason we focus on Gaussian processes in this work. By following the Bayesian paradigm, their predictions consist of both a mean and a variance, which is interpretable as a measure of uncertainty. A more detailed description is given in Section 2.

The rest of this paper is structured as follows. In the next section we explain how we generated the data and give some theoretical background on Gaussian processes and uncertainty sampling. The third section describes our results. In Section 4 we discuss these findings. Finally, conclusions are provided.

6.2 Materials and Methods

6.2.1 Data generation

The simulated data used in this manuscript is provided by a finite element simulation. The simulation consists of a flat bottom hole plate and a line heater. The flat bottom hole plate has following dimensions: 330 x 170 x 10 mm. The material linked to the plate is PVC and the circular pocket is located in the centre of the sample. A representation of the simulation can be found in Figure 6.2.

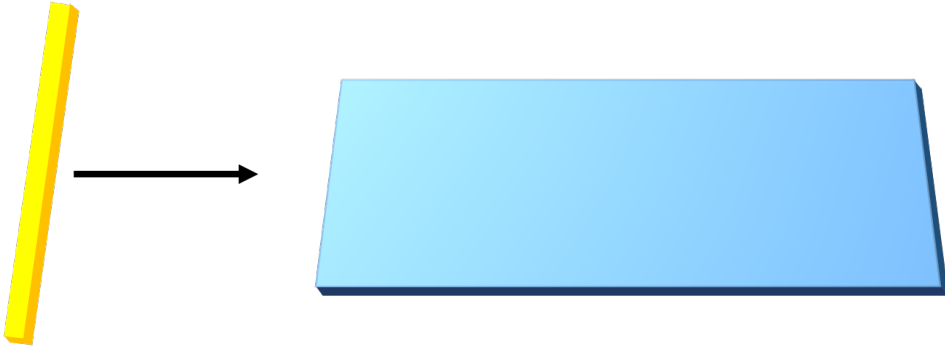


Figure 6.2: Simplified schematic visualisation of the finite element simulation as described in Chapter 3. The simulation consists of a flat bottom hole plate (blue) and a line heater (yellow). The line heater moves above the sample in a linear motion.

The line heater translates above the flat bottom hole plate and the thermal response of the sample is examined. The sample to be inspected is a PVC flat bottom hole plate with defects varying in size and depth. The simulation uses the following variables: movement velocity, distance between the heat source and the camera, heating power, start depth of the defect, diameter of the defect, height of the camera and ambient temperature. This allows for a variety of scenarios to be mimicked. The result of the simulation is the temperature difference between a position on the surface above a defect and a position that is not above a defect. The result of each simulation is used to generate a response surface as explained in Chapter 3.

Running a simulation is much faster and cheaper than performing actual measurements, since there is no need for a cooling time between consecutive simulations. However, as thoroughly described in Chapter 3, every simulation still requires solving time. The data provided by these simulations serve as input for the training of the underlying model in the emulation. In this work, the model is a Gaussian process.

6.2.2 Gaussian processes

Here we give a brief overview of Gaussian processes. A more comprehensive treatment can be found in [78]. The authors define a Gaussian process (GP) as a continuous collection of random variables, any finite subset of which is normally distributed as a multivariate distribution.

We denote a dataset of n observations as $\{(\mathbf{x}_i, y_i)\}_{i=1}^n$, where \mathbf{x} is an input vector of dimension d and y is a scalar-valued observation. In regression, the objective is to find a function $f : \mathbb{R}^d \rightarrow \mathbb{R}$,

$$y = f(\mathbf{x}) + \epsilon, \quad \epsilon \sim \mathcal{N}(0, \sigma_\epsilon^2), \quad (6.1)$$

with ϵ being identically distributed observation noise. This function can be drawn from a GP, which is fully defined by its mean $m(\mathbf{x})$ and *covariance function* $k(\mathbf{x}, \mathbf{x}')$, also denoted as

$$f(\mathbf{x}) \sim \mathcal{GP}(m(\mathbf{x}), k(\mathbf{x}, \mathbf{x}')). \quad (6.2)$$

The covariance function is parametrized by a set of hyperparameters θ , that can be learned by maximizing the log marginal likelihood. In our experiments we use BFGS, a quasi-Newton method described in [83]. The squared exponential kernel (SE), also called the radial basis function kernel, is applicable in a wide variety of situations because it generates smooth (infinitely differentiable) functions. It has the form:

$$k_{SE}(\mathbf{x}, \mathbf{x}') = \sigma_f^2 \exp\left(-\frac{|\mathbf{x} - \mathbf{x}'|^2}{2l^2}\right), \quad (6.3)$$

in which σ_f^2 is a height-scale factor and l the length-scale that determines the radius of influence of the training points. Since our data is both very smooth and stationary (covariances only depend on the distance between two data points, not their location), the squared exponential kernel is a more than reasonable choice. We do however implement a different length-scale parameter for every input dimension. This technique is called automatic relevance determination (ARD) and allows for functions that vary differently in each input dimension [84]. The kernel used in this work has the form:

$$k_{SEARD}(\mathbf{x}, \mathbf{x}') = \sigma_f^2 \exp\left(-\frac{1}{2} \sum_{j=1}^d \left(\frac{|\mathbf{x}_j - \mathbf{x}'_j|}{l_j}\right)^2\right). \quad (6.4)$$

6.2.3 Active learning

The process of simulating the values for the temperature difference given a large amount of inputs is very time consuming. The strategy to overcome this via emulation, is to train a machine learning algorithm to predict those values. The aim is now to train the model as accurately as possible given a limited number of data points. This is achieved by the following steps:

1. A small selection of data points is sampled uniformly from the dataset. Alternatively, those points could lay an n-dimensional grid, be Latin hypercube sampled or chosen from a Sobol sequence. In [81], a comparison between the different sampling methods is made. In this work, we restrict ourselves to uniform sampling, as it is the most simple method. For a more comprehensive study on this topic, we refer the reader to [85] and [86].
2. The model (in our case the Gaussian process) is trained on this initial small dataset.
3. The point from the input space with the highest uncertainty (variance) in the GP's posterior distribution is chosen and added to the data set of the

GP, which is then retrained. This method is called Uncertainty Sampling (US). Alternatively, the point which reduces the total variance of the posterior could be chosen. This method is called Integrated Variance Reduction (IVR). We implemented US because it is cheaper to compute [87].

4. Step 3 is repeated until a certain criterion is met. When limited by a computational budget, this could be a fixed number of iterations. Another criterion is convergence in the posterior distribution, which means that adding a new data points no longer has a significant result on the predictions of the GP.

This process is called active learning and has been well studied by the machine learning community [78, 88, 89, 90]. A more recent view on the subject in the context of information theory can be found in [91]. This algorithm is summarised in Algorithm 6.1.

Algorithm 6.1 Active Learning with Uncertainty Sampling

```

1: trainset  $\leftarrow$  dataset( $n$ )            $\triangleright$  start with a training set of  $n$  random points
2: testset  $\leftarrow$  dataset - trainset      $\triangleright$  put remaining points in test set
3: GP.train(trainset)                      $\triangleright$  train Gaussian process on trainset
4: oldPosterior  $\leftarrow$  GP.predict(testset + trainset)  $\triangleright$  get the GP posterior
5: while nrOfIterations  $\leq$  maxNrOfIterations  $\triangleright$  check computational budget
6:   or diffPosterior  $\leq$  minDiffPosterior do  $\triangleright$  check for convergence
7:   ActiveLearningIteration(GP)           $\triangleright$  perform one iteration
8:   newPosterior  $\leftarrow$  GP.predict(testset + trainset)  $\triangleright$  get the GP posterior
9:   diffPosterior  $\leftarrow$  newPosterior - oldPosterior  $\triangleright$  calculate the change
10:  oldPosterior  $\leftarrow$  newPosterior  $\triangleright$  store for next iteration
11: end while
12: procedure ACTIVELEARNINGITERATION(GP)  $\triangleright$  Active Learning iteration
13:   trainset  $\leftarrow$  dataset(US(testset))  $\triangleright$  update training set
14:   testset  $\leftarrow$  dataset - trainset  $\triangleright$  update test set
15:   GP.train(trainset)  $\triangleright$  retrain GP
16: end procedure
17: procedure US(testset)  $\triangleright$  Uncertainty Sampling
18:   for all  $\mathbf{x}_{\text{test}} \in$  testset do  $\triangleright$  evaluate every test point
19:     if  $\text{var}(\mathbf{x}_{\text{test}}) > \text{var}(\mathbf{x}_{\text{mostVar}})$  then
20:        $\mathbf{x}_{\text{mostVar}} \leftarrow \mathbf{x}_{\text{test}}$   $\triangleright$  this point becomes new candidate
21:     end if
22:   end for
23:   return  $\mathbf{x}_{\text{mostVar}}$   $\triangleright$  return test point with most variance
24: end procedure

```

6.3 Results

The purpose of this manuscript is to investigate the feasibility to use emulation for dynamic line scan thermography. Predicting the optimal parameter set is difficult and highly dependent on the defect characteristics. Generating a sufficient detailed response surface requires a large number of data points. The incentive of

using Gaussian Process emulation for parameter prediction, is based on the idea that it takes less data points to learn the effect of the different design parameters in comparison to generating a response surface.

We evaluate the benefits of dynamic line scan thermography emulation by means of a Gaussian process in two ways. First, we assess the ability of the model to capture the underlying physical truth. Second, we formulate several design specific queries that arise in a practical setting and investigate to which extend the emulation can be utilized to answer these.

6.3.1 Model performance

In order to assess the accuracy of the model, we need a ground truth. We ran the simulator, as described in [51], 45000 times. However, the movement velocity, height of the camera and the ambient temperature were kept constant at 10 mm/s, 450 mm and 20 °C respectively. The remaining input variables are:

1. distance between the heat source and the camera, range 50 mm to 600 mm
2. heating power, range 50 W to 800 W
3. start depth of the defect, range 2 mm to 9.8 mm
4. diameter of the defect, range 12 mm to 24 mm

These four-tuples are the inputs of our dataset. The reason we limited the dataset to four variables, is that composing a dataset of seven input variables with enough resolution to assess the accuracy of the model, would take a lot more data points and thus time to simulate. Moreover, in an industrial context, one does not always have full control over the parameters we fixed in this demonstration, as they are dictated by the production process and installation itself.

For each of those four-tuples, the temperature difference between a position on the surface above a defect and a position that is not above a defect is calculated. This temperature difference is the output of our dataset.

Via active learning, as described in Section II, we iteratively pick data points from the dataset and move them to the training set of the Gaussian process. The remaining data points in the dataset serve as test points. After the Gaussian process is trained, two calculations on the test points are performed:

1. The root mean square error between the posterior mean in each test point and the actual values from the simulations. This number will serve as a measurement for the deviation of the model from the underlying truth.

2. The average posterior standard deviation for all remaining test points. This is a measurement for how much uncertainty there still is in the system. The point with the highest variance, i.e. the highest uncertainty, becomes the point that will be moved from the test set to the training set of the Gaussian process in the next iteration.

When both of these numbers flatline, then there is little to be gained in running more simulations. In that case, the Gaussian process is able to approximate the ground truth. Since Gaussian Processes are used in this research to approximate a surface rather than to find an optimum, the RMSE and the standard deviation represent the total error between the approximation and the ground truth. If the total error becomes smaller, this means that the approximation is improving as a whole.

We performed the active learning process for 500 iterations. We started with 25 training points randomly chosen from the dataset. This makes for a total of 525 data points in the Gaussian process of the last iteration. In Figure 6.3 the learning curves of the Gaussian process are visualised. The exact curves of the iterations depend on the initial random points, that are drawn from the dataset described above. Therefore, we repeated the experiment five times.

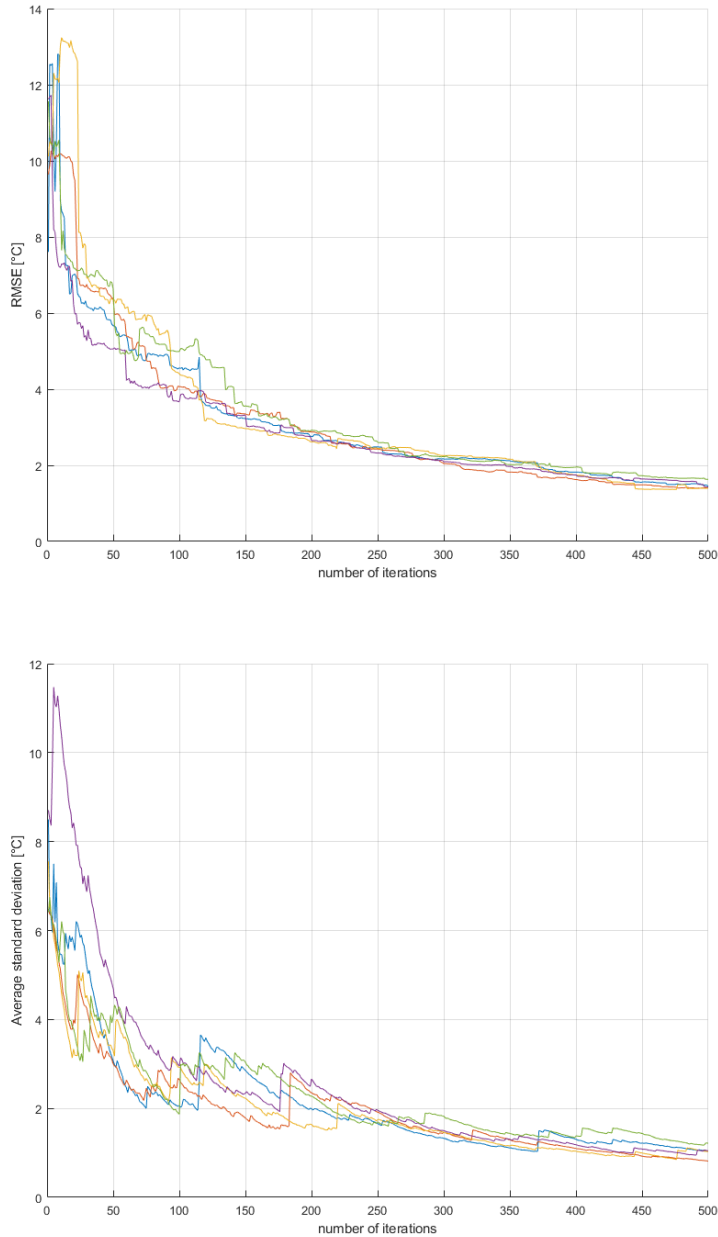


Figure 6.3: Graphical visualisation of the learning process of the Gaussian process for five runs of 500 iterations. The top figure represents the Root Mean Square Error (RMSE) of the learned surrogate compared to the response surface created in Chapter 3. The error describes the difference between the trained Gaussian process and the generated response surface of Chapter 3. Both are approximations of the real-world. The bottom figure shows the average standard deviation of the Gaussian process posterior prediction.

The hyperparameters for the covariance functions, as described in Equation 6.4, of the trained Gaussian processes, can be found in Table 6.1.

Table 6.1: Hyperparameters of the trained Gaussian processes

Run	$l_1[mm]$	$l_2[W]$	$l_3[mm]$	$l_4[mm]$	$\sigma_f^2[C]$
1	142.81	246.17	2.28	2.35	11.97
2	150.00	255.99	2.30	2.41	11.75
3	182.72	216.52	2.23	1.98	10.87
4	177.48	223.02	2.26	1.96	10.97
5	153.98	238.46	2.60	2.37	12.84

The values for the hyperparameters of the covariance function of the trained Gaussian processes for each of the five runs.

6.3.2 Parameter Design

Generating a response surface is a technique used in Design Of Experiments (DOE) often with the idea of investigating the interference between several factors in a process. It is possible to determine which factors have an influence on the output effect and in what way the output responds on a change in one or a collection of input parameters. Afterwards the insight in the process and the response surface itself can be used to optimize the parameters in order to minimize/maximize the output effect of the process. In industrial applications, one is generally not interested in the influence of the different input parameters on the output effect. There, focus lies on how to optimize the efficiency of the inspection process itself, or in other words, how to reduce its economical impact on the overall production process.

Once a Gaussian process has been trained to emulate the simulations up to an adequate level, we can query the model with real world engineering design questions. Below, we give a few examples. We picked the threshold values in these examples in an arbitrary way. Here, they only serve for demonstration purposes. They are of course application specific. In a practical setup, they depend on the type of the camera used, the ambient temperature in the production facility, the material of the sample under inspection, etc.

Example 1: From a practical and economical point of view, the most crucial input parameter is the heating power. The reduction of the energy needed to heat a sample under inspection, results in a drastic reduction of the inspection cost. To accommodate this, we can ask the question: What parameter combination should be used to be able to detect a predefined defect with a certain start depth and diameter, with a minimal amount of heating energy needed? For instance, we want to be able to detect a defect with a diameter of 14 mm, which is situated

6 mm below the surface. We query the GP posterior prediction for all test and training points, by filtering on the input variables start depth and diameter. Then, we filter the temperature difference on a range from 5 °C to 10 °C. A temperature difference that is lower, might make it hard to detect with a given camera. A temperature difference that is higher, means the sample under inspection is heated to a value that is too high, resulting in a waste of energy and undesirable effect on the material itself. From all the remaining possible inputs, we choose the ones with the lowest heat load. In our case this is 50 W. We end up with a range for the distance between the camera and the heat source of 335 mm to 420 mm. All these values yield a temperature difference between 5 °C and 10 °C for the given defect. On the other hand, when the distance between the heat source and the camera is below this range, we can observe that the heat load has to be increased to 75 W to still yield a temperature difference between 5 °C and 10 °C.

Example 2: In some practical scenarios, it is possible that the distance between the heat source and the camera has to be a fixed value. For instance due to constraints on the physical setup in the production environment. We can ask the trained model: What parameter combination should be used to be able to detect a range of defects with only adjusting the heating power? Again, we filter the temperature difference on a range from 5 °C to 10 °C. We fix the distance between the heat source and the camera to 100 mm. We observe that we need a minimum of 500 W to be able to detect all defects from our dataset. When the heat load is below 500 W, we can no longer detect defects that are lower than 9.8 mm below the surface.

Example 3: The model can also be used to visualize regions in the input space that result in undesirable temperatures for the sample. For instance, we can highlight regions where the temperature of the sample would become too high. This serves as a warning, as temperatures that are too high might cause damage to the sample under inspection. In Figure 6.4, we provide an overview of the predicted temperature differences per defect diameter. Regions that are coloured are to be avoided when designing the dynamic line scan thermography setup. These plots also reveal that some regions of the input space are workable for some defects, but not for others. The full benefit of these plots comes into its own when using software that allows the end user to rotate the generated cubes, which is trivial to set up in Matlab or any Python environment equipped with a graphing library such as Matplotlib.

Example 4: In this last example, we visualize the plots from Example 3 in a different way too highlight regions of the input space that correspond to appropriate temperature differences. In Figure 6.5, we colour regions that result in hard to detect (or even undetectable) temperature differences red. For this example, we set the threshold to an arbitrary value of 5 °C. Regions that result in temperature differences above 25 °C are coloured yellow. Ideal regions lie in between those values and are given the colour green.

Table 6.2: Optimal parameter sets found for the examples explained above.

Parameter	Example 1	Example 2	Example 3	Example 4
Ambient Temperature [° C]	20	20	20	20
Velocity [mm/s]	10	10	10	10
Camera Height [mm]	450	450	450	450
Diameter Hole [mm]	14	12 - 24	22	12
Startdepth Hole [mm]	6	2 - 9.8	2 - 9.8	2 - 9.8
Heating Power [W]	50	500	200 - 400	600 - 800
Distance cam. - heat [mm]	335 - 420	100	500 - 600	50 - 200

Example 1 handles the question 'What parameter combination should be used to be able to detect a predefined defect with a certain start depth and diameter, with a minimal of amount of heating energy needed?'.
 Example 2 searches for the best parameter combination to detect as many holes as possible with only adjusting the heating power.
 Example 3 predicts the regions in the input space that result in undesirable temperatures for the sample. Consequently the interesting regions can be found as the remaining parameter combinations.
 Example 4 visualizes the regions of the input space that correspond to appropriate temperature differences. Depending on the colours one can find a suitable region.

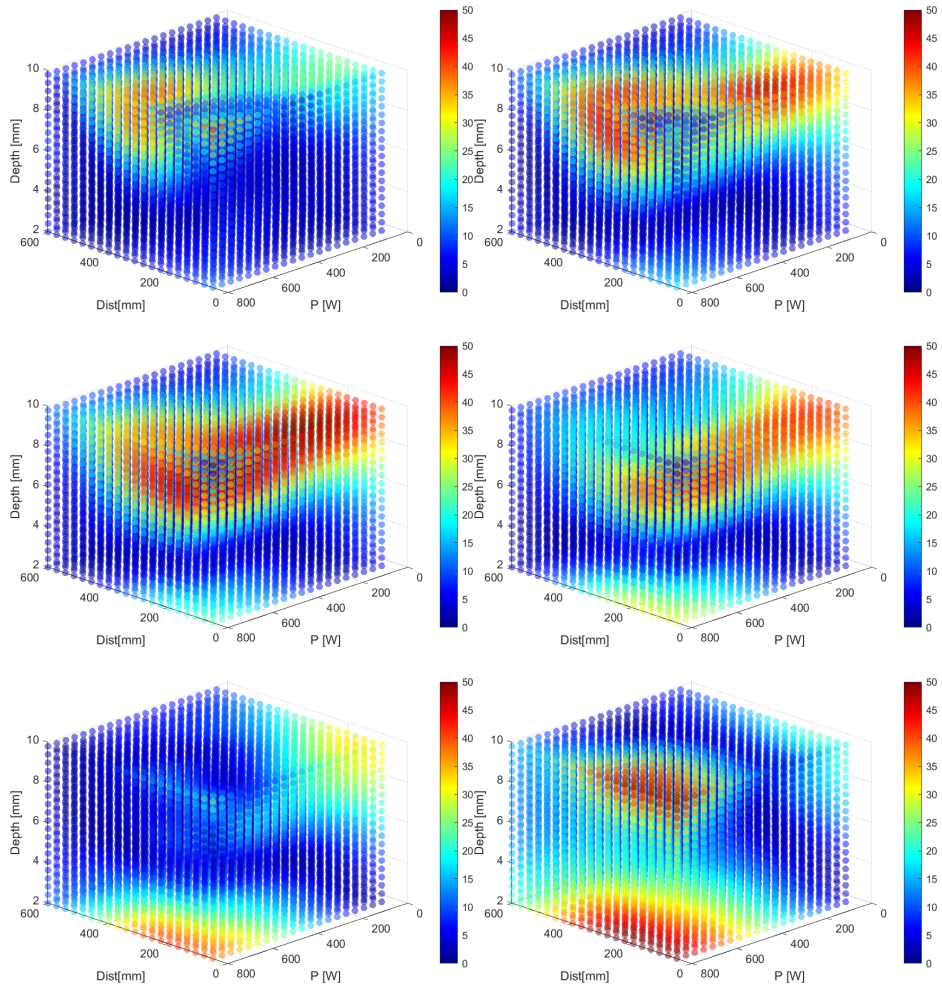


Figure 6.4: Visualization of the temperature difference for six different defect diameters. (a) 12 mm, (b) 14 mm, (c) 16 mm, (d) 18 mm, (e) 20 mm and (f) 22 mm. Red indicates temperature differences that might result in damaging the sample under inspection. These plots serve as a warning when designing a setup. One can combine different plots to find a suitable region to perform measurements without the danger of damaging the sample regardless of the size of the defect.

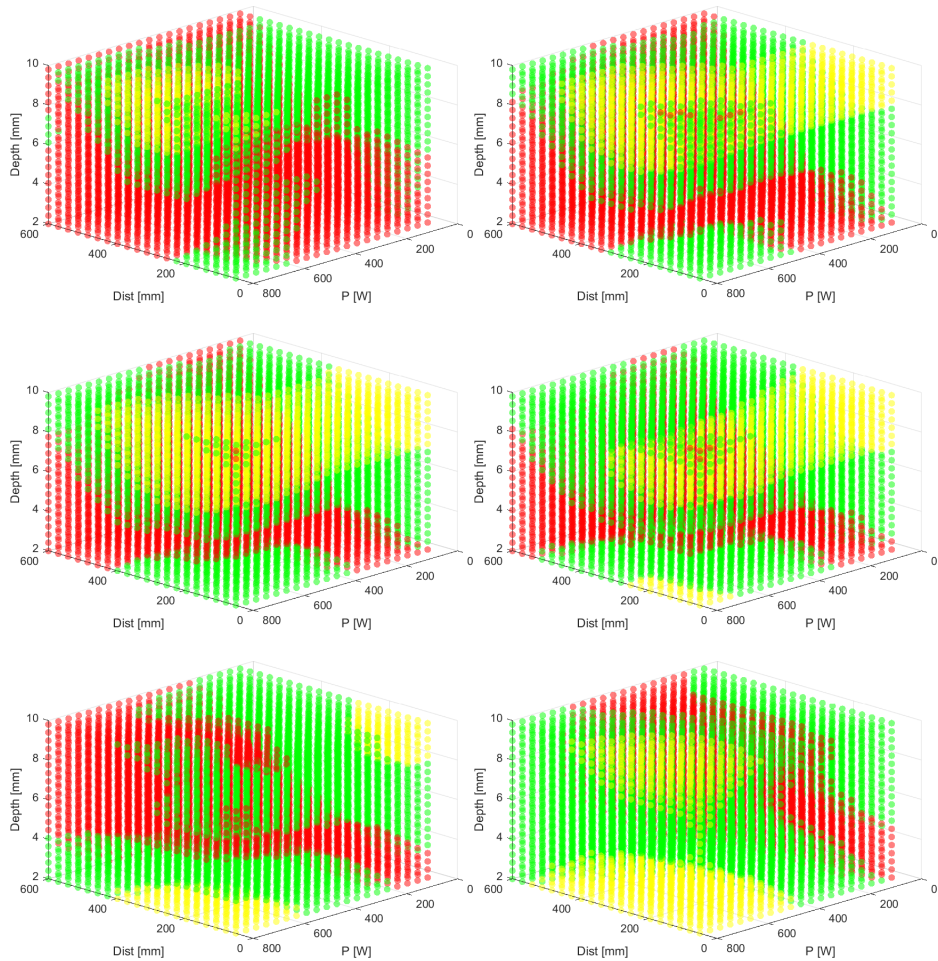


Figure 6.5: Visualization of the temperature difference for six different defect diameters. (a) 12 mm, (b) 14 mm, (c) 16 mm, (d) 18 mm, (e) 20 mm and (f) 22 mm. Red are temperature differences below 5 °C, yellow above 25 °C and green in between. Only the green regions are of practical value in a real world application.

6.4 Discussion

Both the RMSE and the average standard deviation show an initial steep decline that gradually flatlines. All our experiments have shown to converge to the same values after enough iterations. These curves support the decision making process whether or not to continue to add more data points (costly simulations). For our application, one could conclude that after 350 iterations the RMSE and the standard deviation are sufficiently low enough and do not change significantly

anymore. The total amount of iterations needed to train the Gaussian process such that it can approximate the simulations up to an adequate level, depends on the application itself. It is a function of the available computational budget and the amount of uncertainty that can be tolerated. Similarly, generating a response surface is also subjective in the sense of deciding when a surrogate has a sufficient resolution and accuracy for the specified application. Therefore this manuscript does not focus on the exact numbers or percentage of data points needed to approximate the response surface.

Simulators and emulators are models of an underlying truth and as such nothing more than an approximation. This means that one has to be prudent about the outcomes of such models. For instance, it is possible for the model to predict values that do not correspond with reality or, even worse, that do not have any physical meaning. For instance, we noticed that for some test points (points where we make predictions) far away from the data, it is possible to obtain negative values for the temperature difference, even though the data only contained positive values. This issue can be dealt with in two ways. First, one could implement constraints on the model. In our case we could alter the covariance function, such that only positive values can be predicted by the model. This is an approach thoroughly explained in [92]. Second, in this research, we chose the Gaussian process for the underlying machine learning model. By following the Bayesian paradigm [78], this stochastic model makes predictions that are not just numerical values (in our case for the temperature difference). They are also accompanied by a variance. As such, each prediction for every test point is in fact a normal distribution. The variance can be interpreted as a measurement of uncertainty about the prediction. This extra information should be taken into account when evaluating the predictions.

As mentioned throughout the text, several optimisations could further improve the performance of the model. They were not investigated in this work, because we wanted to restrict ourselves to a basic implementation of the core idea of approximating dynamic line scan thermography parameter design via emulation. We consider these to be future work. First, the initial sampled points were drawn uniformly from the input space. Several alternatives are described in the literature [81, 85, 86]. As the total number of sampled points increases, the influence of the initial points becomes less important. Still, on very tight computational budgets, this could become a factor of interest. Second, the Uncertainty Sampling method sometimes favours points on the boundary of the input space. This is due to the fact that the density of data points is lower in those regions and thus the uncertainty is higher (there are no data points beyond the boundary). Integrated Variance Reduction takes this drawback into account and calculates the total amount of uncertainty reduction a new data point yields. It does so for each point in the test set. This reduces the score of points in the vicinity of the boundary. It is to be expected that Integrated Variance Reduction would reduce the number of time consuming sampled input points, but at a higher computational cost. This is also stated in [87]. The effect of this remains an open question. Third, as also stated above, the Gaussian process used in this study can be further developed to incorporate prior knowledge in the form of constraints.

6.5 Conclusion

We have described a method to emulate the time consuming simulations for a dynamic line scan thermography setup. By means of a Gaussian process, the simulator can be approximated. We have shown that the accuracy increases for every simulation that is added to the training set of the Gaussian process. However, the increase flatlines after a certain application specific number of simulations. At this point, adding more simulations, a time consuming effort, does not add to the overall usefulness of the model. We also posed several parameter design questions relevant in real world engineering design challenges. We demonstrated that a trained emulator can be queried to help find solutions to those questions. This method facilitates the process of finding an economic viable set of design parameters for a dynamic line scan thermography setup in industrial applications.

A novel line scan algorithm for unsynchronised dynamic measurements.

The final chapter of part 3 explicates a novel line stacking technique to enable the processing of Dynamic Line Scan Thermography data without the need of synchronizing the movement of the sample to the framerate of the camera. This enables the implementation of dynamic measurements in processes where the translation speed is fixed. The following chapter explains the algorithm itself and shows the data as a result of applying the algorithm on UV measurements, hyperspectral images and thermal images. Besides converting the spatial thermal data to temporal data, the proposed algorithm also resolves the negative effects of heterogeneous illumination that can occur during inspections.

7.1 Introduction

Non-destructive testing is an attractive way to evaluate the performance, integrity, or deterioration of an object or structure. With nondestructive testing, the object or structure being inspected does not have to be disassembled to find hidden features that are not visible on the surface. Another advantage is that, compared to destructive analysis methods such as fracture or accelerated corrosion testing, the inspection can be performed without affecting the material itself.

There are several methods of nondestructive testing, such as magnetic particle inspection (MPI) [93], radiographic testing, ultrasonic testing (UT) and eddy current testing (ECT). However, there are several drawbacks using these methods such as: MPI can only inspect metallic samples, RT requires extensive safety precautions, UT and ECT are point based methods which are not suitable for a large sample size. To compensate the aforementioned drawbacks, camera-based methods can

be used in a wide variety of applications. Camera based methods include: Infrared Thermography (IRT), Hyperspectral Imaging, Ultraviolet Imaging or RGB Imaging.

Infrared thermography is becoming increasingly important in nondestructive testing for applications such as subsurface defect detection [94, 95, 74, 96], biomedical applications such as DIEP-flap research [97], and historical objects can be inspected with IRT [98]. A typical IRT setup contains a modulated heat source and a thermal camera that can record the heating or cooling curve of each pixel in the detector array. Based on these temperature differences, it is possible to obtain information about the subsurface material properties, since heat dissipation depends not only on the surface but also on the subsurface material properties.

Another NDT camera technique is hyperspectral imaging (HSI). In this technique, we record the reflectance intensity of hundreds of narrow wavelength bands, for each pixel. This measurement technique allows us to obtain more information about the chemical composition of the scanned object. HSI is commonly used in agriculture [99, 100] (to quantify plant health), forensics [101, 102], drug detection [103, 104], NDT [105, 106] and remote sensing [107]. Most hyperspectral imaging techniques are based on line scan measurements. Recently, snapshot hyperspectral cameras developed by Imec [108, 109] have seen a resurgence. These cameras are capable of operating as full area cameras instead of line scan cameras. Another camera-based NDT technique is the use of ultraviolet (UV) cameras. These cameras operate in the ultraviolet region of the electromagnetic spectrum. This UV range includes wavelengths between 100 and 400 nm. An ultraviolet light source is used to illuminate the object, creating fluorescence in the object that can be measured with a detector that is sensitive in the UV range. Typical applications for these cameras are: Forensics (fingerprint and bodily fluid detection) [110, 111], Painting inspection [112], Emission monitoring [113], Coating inspection [114]. Compared to light in the visible spectrum, UV light has a larger diffraction limit, making it possible to distinguish smaller objects or defects than when using visible light [115]. In this article we use a subpart of the UV range, namely the UV-A, spanning from 320 nm to 400nm.

When using camera-based techniques, objects are usually examined from a stationary position, which limits the size and/or resolution of the samples that can be examined. Larger samples require greater distance between the camera and the sample to examine the entire object. Consequently, the resolution of the captured images is lower in a given area. Small defects may not be visible due to insufficient resolution. For example, in thermography, the rule of thumb is that the diameter of a defect must be at least the area of 3×3 pixels. [51] Dynamic line thermography (DLST) is often used when inspecting large surfaces or surfaces in a continuous process such as cold-rolled steel fabrication. [51]. This technique uses a linear heat source and a thermal imaging camera at a specific distance from that heat source. The object of interest moves relative in a linear motion using a traverse system or conveyor belt. The resulting images are reconstructed from the sequence of captured images. This reconstruction is called transforming a spatial matrix into a temporal matrix and is shown in Figure 7.3.

When creating reconstructed images in thermography and hyperspectral inspections, the motion of the sample and the frame rate of the camera are synchronized. In this way, it is relatively easy to extract the desired area from each frame of the recorded sequence, as described in [116]. In industry, however, it is rarely possible to match the movement speed of the object to the frame rate of a camera, as this would result in fewer objects being produced per hour. Cameras, on the other hand, often have a fixed frame rate, making it impossible to adjust the speed at which an object moves.

In this manuscript, an algorithm is proposed for reconstructing images acquired with an unsynchronized dynamic measurement. This algorithm can be used for dynamic line scan thermography measurements and hyperspectral analysis, but also provides a solution for measurements with a heterogeneous illumination source, as is often the case when using HSI or UV cameras.

It is possible to image samples in multiple sections and then stitch them together to examine the entire sample with sufficient resolution. This method only works if the light source used is homogeneous. The slightest difference in illumination will cause a deviation in the recorded data, making it pointless to stitch the different sections together. This is illustrated in Figure 7.1, where the individual images are stitched together to reconstruct the original object.

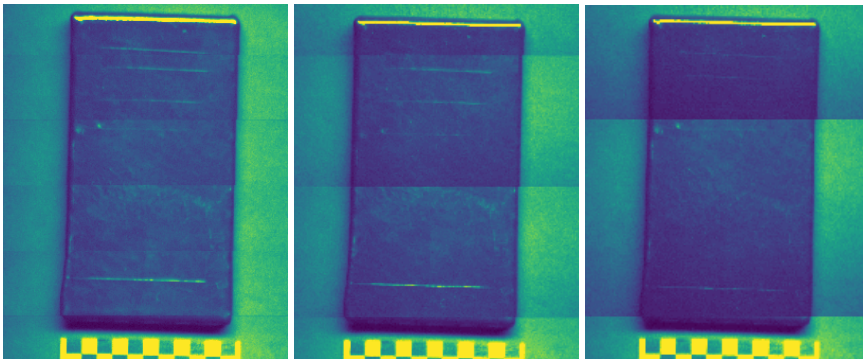


Figure 7.1: Three UV images that are composed of separate images, taken at different locations for the same sample. **(Left)** Six separate images; **(Middle)** Four separate images ; **(Right)** Three separate images. The stitching lines are clearly visible, this could result in misclassifications in defect detection.

In this Chapter, we first explain in detail the algorithm used, followed by a description of the equipment used for the measurements. In Section 7.3, the algorithm is applied to three different camera technologies: UV, IR and RGB, demonstrating the usefulness of this novel algorithm.

7.2 Materials and Methods

To evaluate the applications and show the robustness of the proposed algorithm, different camera types are used. Each camera operates at a different wavelength and has a different frame rate. The cameras used in this study are:

- UV Camera: IMPERX GEV B1620M, frame rate: 35 fps
- Hyperspectral Camera: Photonfocus MV1-D2048x1088-HS02-96-G2, frame rate: 42 fps
- Infrared Camera: Flir A715, frame rate: 30 fps

The objects of interest were placed on a translation stage that moved with a fixed speed of 15 mm/s. The cameras were placed above the translation stage and pointed downward, perpendicular to the translation. Corresponding light source (heating source for IR), provided continuous illumination during the experiments. An image of the setup can be seen in Figure 7.2. An enclosure was made to block harmful UV radiation during the measurement.

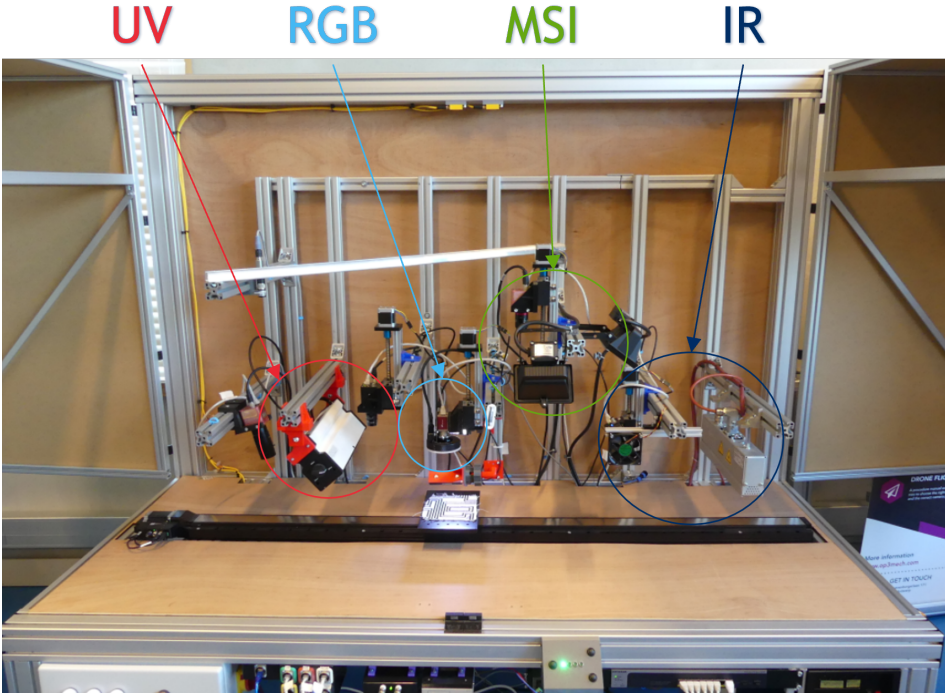


Figure 7.2: Image of the experimental setup with the housing open. Multiple cameras and corresponding light sources are mounted above a translation stage to allow examination of a sample in multiple wavelengths.

7.2.1 Algorithm

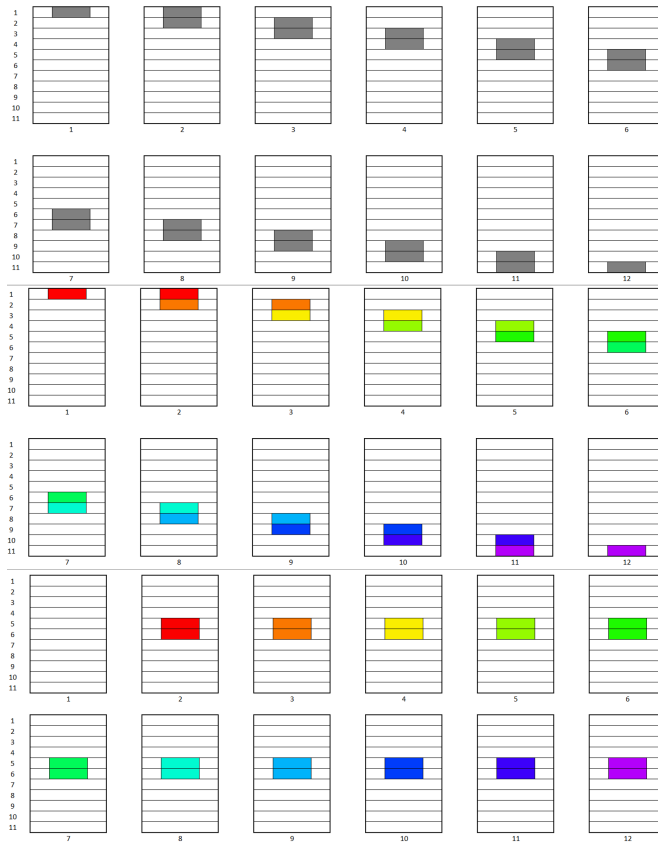


Figure 7.3: Transformation of the spatial matrix of the raw images into a temporal matrix. The first two rows of the images show the raw image sequence, the middle two rows visualize the division into parts corresponding to the pixel shift between successive images, and the last two rows show the stitched temporal matrix. The colors correspond to the moment after passing the light source. The color red corresponds to the spatial directly after passing the light source. Matching colors are combined in the same image from the temporal matrix.

Several steps are required to correct an image sequence where the camera and object speed is not matched. However, the object has to move in a constant linear motion. For an overview of the correction algorithm, see Figure 7.9. The following list explains the algorithm in detail.

1. Capture raw data

The images are captured during translation of the object. While making sure that the start and end of the object is fully recorded.



Figure 7.4: Raw data as captured in a measurement. One can find a pixel shift of 1.5 between two consecutive frames.

2. Preprocess data

Depending on the camera type, preprocessing is required, e.g. NUC (Non Uniformity Correction) for IR cameras or demosaicing for snapshot HSI cameras. Demosaicing, also known as debayering, is an image processing technique to reconstruct full-color images from raw data. Demosaicing involves interpolating missing color information for each pixel by considering neighboring pixels with known color data.

3. Find pixel shift

To calculate the pixel shift from frame n to $n+1$, we present two methods. The first method is to detect and track a checkerboard in a sequence of frames. The upper left corner of the checkerboard is tracked across a series of frames and fitted with a first degree function to minimize the error. The other method is to calculate the pixel shift. This is possible if the camera parameters are known. For more details, see Section 7.2.1.1 [117]

4. Factorize pixel shift

The pixel shift is converted to a fraction with a maximum denominator of 10. The maximum denominator is chosen empirically to limit the computational cost while still providing an accurate result. One should consider the necessary accuracy needed for the application versus the computational cost.

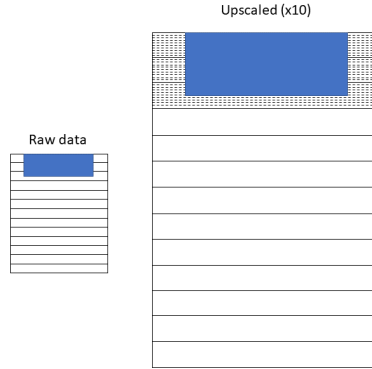


Figure 7.5: A pixel shift of 1.5 can be represented as $15/10$. Therefore a denominator of 10 is used in this example. Consecutively the raw data is upscaled by a factor of 10.

5. Upscale the images

The preprocessed images are resized in length, through interpolation, by a factor equal to the denominator of the previously calculated fraction.

6. Create a temporal matrix

This step consists of a main loop and a nested loop. The main loop iterates over all the different frames of the temporal matrix. The number of frames is calculated by $ft = l * Fraction$, where ft is the resulting number of frames in the temporal matrix and l is the length of a single frame from the original sequence. The nested loop iterates over the original sequence and copies the corresponding rows from the original sequence into the temporal matrix. This step is shown below in pseudocode:

```

for  $i \leftarrow 1, ft$  do
  for  $j \leftarrow 1, fo$  do
     $T_{Mat} \leftarrow O_{Mat}$ 
    Where  $T_{Mat} = \text{line: } j * N : (j * N) + N$  from frame  $k$ 
    Where  $U_{Mat} = \text{line: } (i * N) + N : i * N$  from frame  $j$ 
  end for
end for

```

with fo as the amount of original frames, T_{Mat} as the temporal matrix, U_{Mat} as the upscaled sequence, N as the numerator and D as the denominator of the fraction pixel shift.

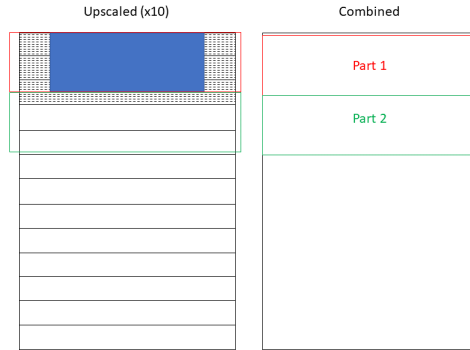


Figure 7.6: The temporal matrix is created by combining parts of the upscaled data. During this process a shift of the object to be inspected can be seen.

7. Correct temporal matrix

The temporal matrix indicates a shift of the object in the direction of translation. This can be corrected by shifting the image.

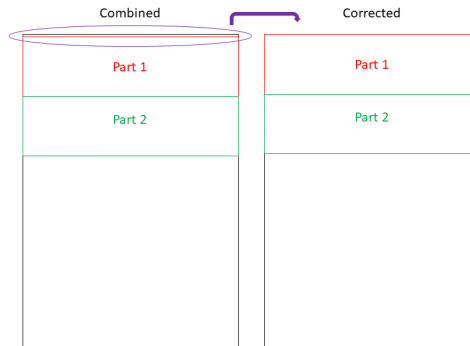


Figure 7.7: The shift in the combined data can be corrected by shifting the whole image in the direction of the image.

8. Downscale the images

The resulting temporal matrix is scaled down in length by a factor equal to the denominator of the previously calculated fraction.

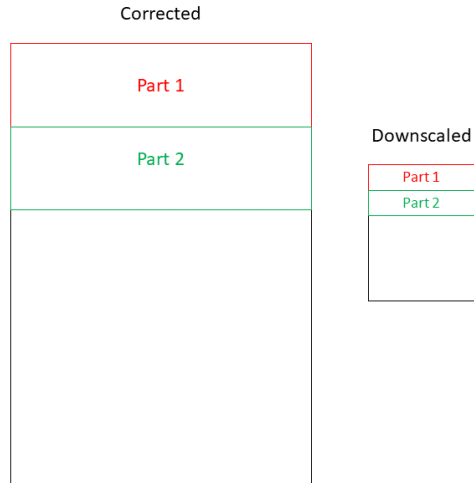


Figure 7.8: The corrected combined image is downscaled to the original image size.

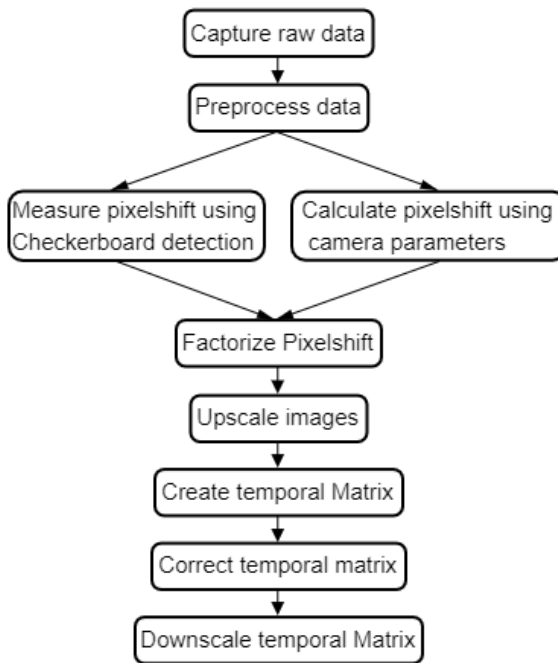


Figure 7.9: Flowchart of the different steps in the proposed algorithm.

7.2.1.1 Calculating correction factor without the use of a checkerboard

The algorithm uses a checkerboard pattern to calculate the required correction factor, as explained in step 3 of the proposed algorithm in Section 7.2.1. However, it is also possible to determine this factor without the use of a checkerboard. The factor can be calculated using the Equations 7.1, 7.2 and 7.3.

$$H = 2 * d * \frac{p}{f} \quad (7.1)$$

The distance (H) detected by a pixel line of a camera can be calculated using the focal length (f) and the height of the camera above the sample (d), as explained in [51]. The calculation can be done similarly using the field of view of a camera. The number of pixels by which the object is translated per second can be calculated using the Equation 7.1 and the translation speed of the object (v).

$$px/sec = \frac{H}{v} \quad (7.2)$$

Using the pixel shift per second and the recording rate of the camera, you can calculate the pixel shift for each frame of the image sequence.

$$factor = \frac{px/sec}{framerate} \quad (7.3)$$

7.2.1.2 Algorithm performance

For the stacking algorithm, a Dell XPS notebook is used with following specs:

1. CPU: Intel i7 6 cores - 2.6 Ghz
2. RAM: 32 GB

The calculation for the provided examples is performed purely on CPU-power, further improvements could be made through parallization on CPU and/or GPU. The time needed to complete the stacking algorithm is very dependent on the processing power, the desired accuracy (scale factor) and the image size. In Table 7.1 the processing times for each experiment can be found.

7.3 Results

In the following section, several applications are presented, one per camera technology, to show the results of the proposed algorithm. The results are presented

	Camera Technology		
	UV	HSI	IR
Frame Size (pixels)	1208x1608	408x208	640x480
Number of frames	498	710	1008
Duration (s)	434	89	101

Table 7.1: Overview of the processing times measured for each experiment, as shown in Section 7.3.

in separate subsections.

7.3.1 IR camera

A commonly used inspection sample in active thermography is a flat bottom-hole plate, as shown in Figure 7.10. The air trapped in the voids cools differently than the surrounding material. As heat is trapped, the air remains at a higher temperature and therefore shows up as a hotspot in the thermograms. Depending on the thermal properties of the sample material and the characteristics of the defects (depth, size, type of defect, . . .), the time needed to show a hotspot in the thermogram may vary. For this reason, the spatial image sequence, as shown in Figure 7.11 must be converted into a temporal image sequence. In the temporal data set, as shown in Figure 7.12, the sample under investigation remains at the same location and the cooling can be investigated.



Figure 7.10: RGB image the inspected bottom wooden sample, so the defects are visible. The dimensions are following: 160x100x5.8 mm.

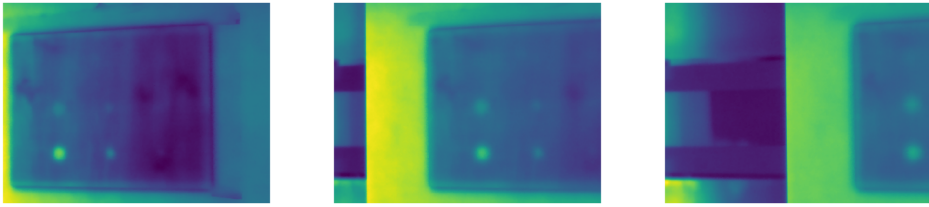


Figure 7.11: Three frames from the sequence captured by the IR camera, while moving the object. **(Left)** Frame 300; **(Middle)** Frame 550; **(Right)** Frame 800. The frames correspond to an amount of seconds after passing the heating source. **(Left)** 10 seconds; **(Middle)** 18.3 seconds; **(Right)** 26.67 seconds.

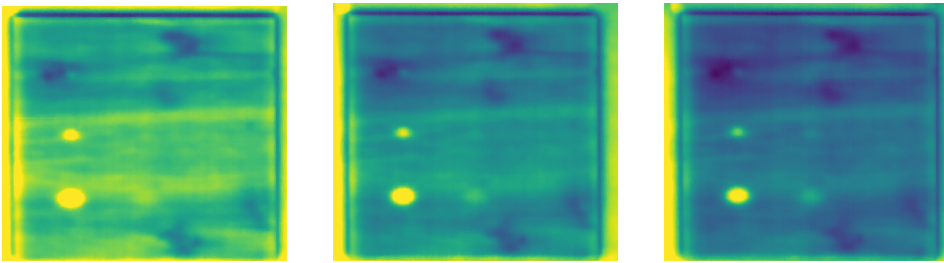


Figure 7.12: Three frames from the temporal matrix. **(Left)** Frame 1; **(Middle)** Frame 428; **(Right)** Frame 856. From the figure, it is apparent that the object dimensions are corresponding to the actual dimensions of the object. The air pockets are visible as circular hot spots. A less accurate stitching would result in a elliptical hot spots.

7.3.2 UV camera

UV cameras can be used to detect scratches with higher contrast than with normal RGB cameras. However, an additional UV light source is required. These light sources are often very narrow and produce uneven illumination in the image, as can be seen in Figure 7.14. The sample studied, which was used for this measurement, is an epoxy-coated carbon steel sample. Several incisions of varying depth were made in this sample using a knife blade. An RGB image of this sample can be seen in Figure 7.13. From the RGB image, it is difficult to see all the different incisions. When looking at the UV sequence in Figure 7.14, the lowest cuts are very visible in the first image and second image, but they become less visible in the last image.

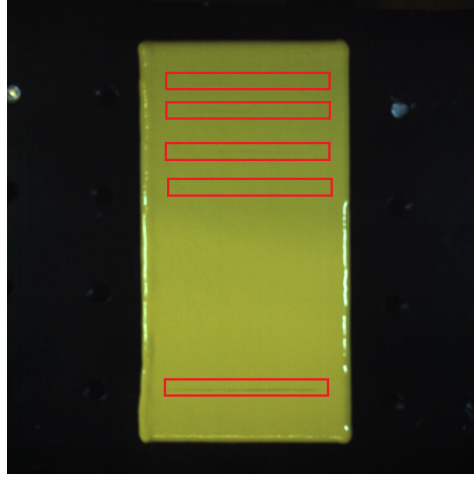


Figure 7.13: RGB image of the epoxy coated steel sample with incisions. The incisions are marked with red squares. The sample has following dimensions: 100x50x13 mm.



Figure 7.14: Three frames from the spatial matrix (**Left**) Frame 90 (2.57 seconds); (**Middle**) Frame 150 (4.29 seconds); (**Right**) Frame 230 (6.57 seconds).

When the spatial matrix is converted to a temporal matrix, the object under study is recreated. Three separate frames from the spatial matrix can be seen in Figure 7.15. Each frame in the spatial matrix represents a different physical location and, in this case, a different intensity of the light source used. In the first image, the incisions are most obvious, but there are also other artifacts that enter the image due to the reflection of the UV light. The second figure is better suited to analyze this type of defect since the reflections of the heterogeneous lighting are no longer present.



Figure 7.15: Three frames from the temporal matrix (Left) Frame 1; (Middle) Frame 50; (Right) Frame 100. Notice that due to heterogeneous illumination from the UV light source, the different frames of the temporal matrix show a different brightness value.

7.3.3 HSI camera

When using hyperspectral cameras, an additional dimension (wavelength) is added to the processing. In Figure 7.17, three different bands are displayed by the HS camera. The object shown is a piece of fabric with weaving imperfections and a black and white woven pattern. This pattern makes it difficult to examine with an RGB camera, as shown in Figure 7.16. When selecting a specific band, the woven black and white pattern will not be visible and the weaving will be clearer.

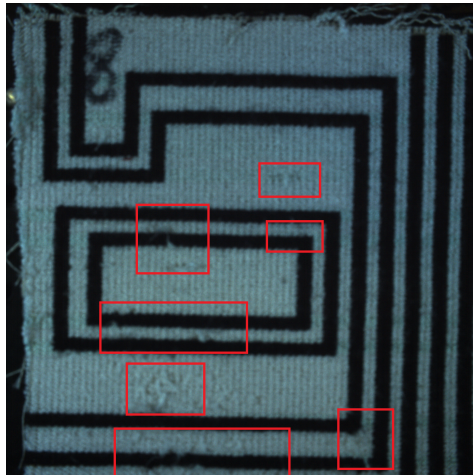


Figure 7.16: RGB image of the textile sample with defects. The defects are marked with red squares. The dimensions of the sample are: 200x200x4 mm.

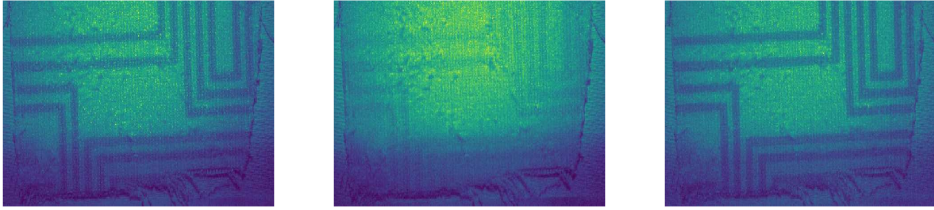


Figure 7.17: Three separate bands from the HS camera for a single frame in the sequence. The identification of weaving errors is complicated through the heterogeneous illumination. **(Left)** Wavelength: 677 nm; **(Middle)** Wavelength: 776 nm; **(Right)** Wavelength: 959 nm.

Figure 7.18 shows the temporal matrix for a single hyperspectral band. It can be seen that not only the choice of wavelength is important, but also the temporal position in order to obtain a high contrast between the weaving defects and the normal tissue. In the third image, for example, the illumination of this spatial position is too large, causing the object to be over saturated.

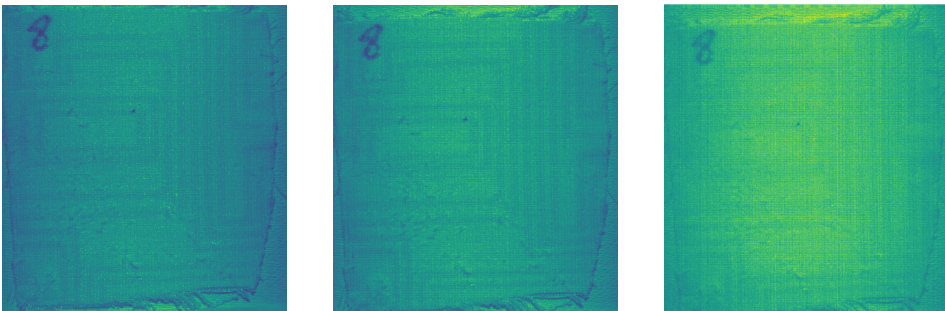
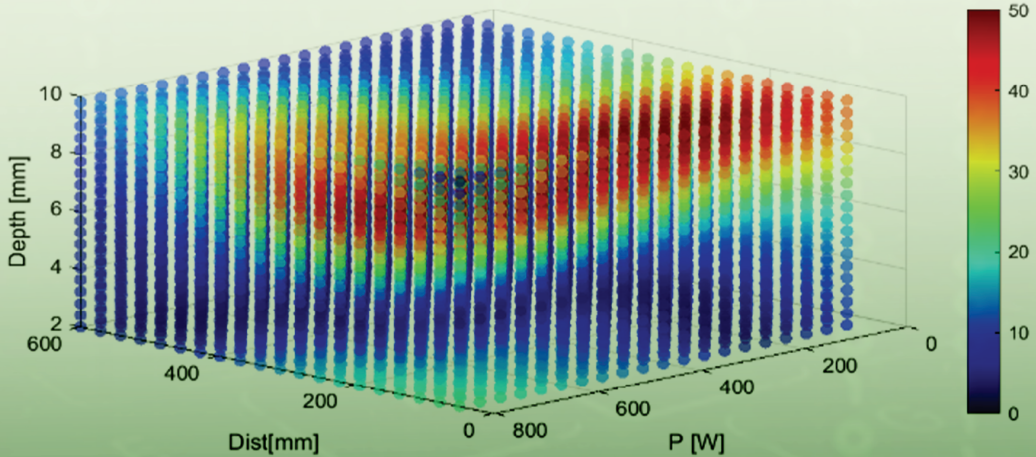
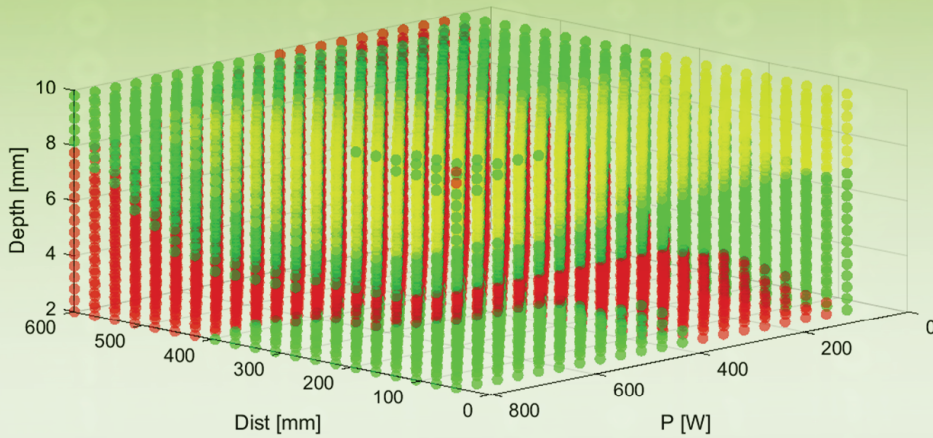
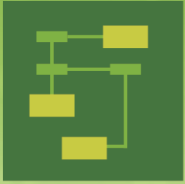


Figure 7.18: Three frames from the temporal matrix for a single wavelength (776nm). Notice that these images display a homogeneous illumination, which improves the detection of weaving defects. The shadows that were present in the original data are no longer present and therefore will no longer be falsely classified as a weaving defect. Throughout the consecutive images in the temporal matrix the influence of the textile color becomes less apparent making it easier to focus on the weaving pattern itself. **(Left)** Frame 1; **(Middle)** Frame 107; **(Right)** Frame 215.

7.4 Discussion and Conclusion

The algorithm discussed in this manuscript allows industry to perform nondestructive inspections during manufacturing without having to adjust the translation speed of the objects to the frame rate of the camera. Nowadays, it is necessary to synchronize the translation speed of an object with the acquisition rate of the camera used. The frame rate of a camera is often fixed, consequently the production process has to be adapted to the capture rate. With this algorithm, the production process is no longer dependent on the camera used. The results show that we are able to successfully apply the algorithm to three different cameras, each camera operating a different wavelength. We are able to achieve an accuracy of 0.1 pixel while stitching the temporal matrix. This accuracy can be further increased by changing the upscaling factor, if this is necessary for the specific purpose. The proposed algorithm can measure the pixel shift in two different ways, through checkerboard detection or field of view calculation.

In addition to the aforementioned advantage of this algorithm, it also allows samples to be examined without the adverse effects of a heterogeneous light source, as can be seen in the sample inspected using an UV camera and light source. In future work, the redesigned matrix can be used to perform automatic inspections using artificial intelligence. The processing time is very dependent on the used PC, the desired accuracy and the size of the images. Additional gains can be found through parallel computing and/or GPU implementation. This will be handled in future work.



Thermography Parameter Design via Gaussian Process Emulation

Volume 15 · Issue 4 | April 2022

Part V

Conclusion

General conclusion and future work.

8.1 General conclusion

This doctoral manuscript provides the basic knowledge of thermography with the aim of understanding the working principle of Dynamic Line Scan Thermography. Various IR techniques were explained in Part 1 of this doctoral dissertation. It is shown that thermography inspections are widely used in several scientific fields. However there are still restrictions when using active thermography for real industrial applications such as the limited field of view. This constraint has proven to become increasingly significant since thermography is more frequently applied to inspect larger composite materials such as wind turbines, plane parts, bicycle frames, etc. Keeping the rule of thumb in mind, a defect has to be bigger than a 3x3 square pixel grid in order to be objectively detectable. Therefore it is undesirable to inspect larger objects in its entirety at once. There exist high resolution thermal cameras but they are much more expensive than regular ones and are larger and heavier which complicates the use in-situ. Hail can be sought in the use of Dynamic Line Scan Thermography whereby the heating source and thermal camera move in tandem relatively to the specimen to be inspected.

The second main part of this doctoral study handles the inspection of the quality of spot welds using thermography. Using active thermography it is possible to assess whether the boundary of the spot weld has a closed circular shape and if the welded area has undergone a change in material properties. Both inductive as halogen heating can offer a solution to inspecting spot welds, but inductive thermography works best to be performed automatically using robot inspections. Since spot welds are often performed in the automotive industry, it is important to be able to reach inside the car body. The advantage of inductive heating is the small size and the possibility to place the heating coils in line with the camera using front heating.

Within the third part of this doctoral study the measurement setup is scrutinized with a view to assess the reliability of the individual components. In order to

optimize the parameters used during Dynamic Line Scan Thermography, it is necessary to ensure an optimized operation of all individual components. Using ray-tracing software an optimized line heating source was designed with the aim of minimizing the heated region and consequently maximizing the power density. In comparison to the commercially available line heaters, the newly designed source combines an elliptical reflector shape with additional straight reflectors. This way the irradiated region is 65% narrower than its commercially available counterpart. The first tests performed with the practical achieved line heater are promising, but further tuning has to be performed in order to have a reliable functioning heating source.

The last main research part describes the parameter optimization of Dynamic Line Scan Thermography in various manners. A finite element simulation was created to mimic the process of DLST whereby the parameters can easily be altered. Initially response surfaces were used in order to predict the most suitable parameter combination according to the desired defect to be inspected. Eight different parameters were included in the tool: movement speed, heating power, distance between the camera and the heat source, the height of the camera above the sample, the ambient temperature, the diameter of the defect, the depth of the defect beneath the surface and the maximum use temperature of the sample. Besides the optimization tool, an insight in the importance of the different parameters and a correlation between the parameters reciprocally could be gathered. The optimization using response surfaces offers the possibility to find the optimal parameter set for the inspection of a specific sample with predefined diameter and depth beneath the surface. It is possible to fix other parameters as well depending on the hardware and/or available liberty in a manufacturing process. However for each different defect the optimization routine has to be performed in order to find the most suitable parameter set. Therefore there is a need for a priori information to find the most optimal parameter set. However in industry, one often knows the possible defects that can occur. The starting depth of the defect for example is often linked to a place in the sample where different layers are bonded together.

Another optimization approach can be found in the idea of minimizing the amount of needed measurements in order to detect all defects in a certain sample. This method was tested using Reinforcement Learning in order to assess the possibility of performing machine learning with the aim of optimizing the measurement parameters. The machine learning environment is fed with the output of the finite element simulation and afterwards extracts the surface temperatures. The retained data points are interpolated to resemble the view of a thermal camera and using an edge detector the defects are automatically found and counted. According to the amount of detected defects a reward is granted to the machine learning agent. It is proven possible to train an agent to detect all defects in a sample, however it takes more training data to achieve this goal in comparison to generating a response surface.

The third optimization approach described in this doctoral study is the use of Gaussian Process Emulation. This technique is based on the conditional probability of an event happening from which a posterior can be extracted. Afterwards this posterior probability can serve as a surrogate function. It is proven that using

this method less simulations are needed to learn the correlation between the parameters used in Dynamic Line Scan Thermography. Besides the limited amount of needed data points, this technique has multiple advantages in comparison to the use of response surfaces. Through Gaussian Process Emulation it is relatively easy to provide an answer to possible questions rising when establishing the parameters of a DLST inspection. It is not only possible to predict the optimal parameter set based on a specific defect, but also to supply the most suitable measurement parameters with the boundary condition of using the smallest amount of heating power. The emulation enables to provide a visible insight in the input space in order to see which regions could be suitable for measurements. An inexperienced inspector could determine at a glance what parameter combinations would result in damaging the sample to be inspected. A second insight provided by the emulation is dividing the input space in regions according to the predicted temperature difference between the surface above a defect and above a sound area. This makes it possible to define measurement parameters without the need of an expert skilled in the art.

Processing DLST measurements is not as straight forward as post-processing thermal data from static measurements. The output of a Dynamic Line Scan Thermography measurement consists of a series of images that can be seen as spatial data. The sample translates beneath the camera resulting in images where the location of the sample is changing. In order to perform post-processing using the well-established techniques in thermal inspections, the sample has to remain in the same location. The conversion between spatial data and temporal (temperature) data is described in main part three as well. A novel technique is proposed to remove the need for synchronisation between the translation speed and the frame rate of the used camera. In industry it is often not possible to match the translation speed and consequently the production speed to the frame rate of an inspection device since this would likely imply changes in the rest of the manufacturing process. It is often not desirable to slow down the established working facility in order to perform quality inspections.

This dissertation answers different questions varying between finding the parameter set to detect a specified defect and providing an insight in the input space in order to remove the need for an expert skilled in the art. Through this doctoral study an insight is achieved in the working principle of Dynamic Line Scan Thermography and the correlation between the measurement parameters. The main insight discovered in this doctoral study is the importance of the distance between the camera and the line heater. The time needed for a specified part of the sample to translate from the heating location to the camera location has to be equal to the time needed for the heat wave to reach the defect and be reflected towards the surface of the sample. This parameter will mainly determine whether or not a defect will be visible in the thermal images. Other parameters such as the heating power, height of the camera, ambient temperature, etc. will affect the appearance of the hotspots in the thermograms.

8.2 Future Work

Further research may still be conducted on the use of DLST in processes where heat is already present. The techniques, as described in this doctoral manuscript, are based on the use of an external heating source. However many manufacturing processes require the sample to be heated already: extrusion of molten steel, pressing of wooden flooring, etc. Removing the need of external excitation could speed up the inspection process since the thermal wave no longer has to travel from the surface to the underlying material before being reflected again. The acquired knowledge in this doctoral dissertation however can not simply be applied in such situations since the heating power can no longer be directly correlated to the other setup parameters. The link between the temperature of an object and its material properties will have to be taken in account.

Improvements can also be made in the area of used cameras. In order to make DLST accessible for a large variety of users it is appropriate to use cheaper cameras. This will enable companies to invest more easily in the technique and even makes it affordable to combine multiple thermal cameras in one inspection process. In order to achieve this, the influence of rolling shutter cameras has to be taken into account. If not the images will be blurry and not usable for determining the structural integrity of the inspected object. The influence of rolling shutters and solutions to overcome the corresponding issues are described by Peeters J. in his doctoral dissertation [118].

Furthermore the acquired knowledge can be used to implement in robotic inspections as an additional parameter to optimize the inspection path. This way the duration of the total measurement could be reduced and therefore more samples could be inspected. Besides conventional robotic inspections, the know-how obtained in this study can be applied to design inspection platforms such as drones to inspect larger objects such as planes, windmills, bridges, etc. The placement of heating source and camera can be chosen in a smart manner based on the desired inspection speed of the unmanned vehicle. However in order to be able to inspect above-mentioned objects, an extension of the used techniques has to occur towards composite materials. One can imaging the difficulties of an anisotropic material and therefore changes will have to be implemented.

Hopefully this doctoral study can provide an aid to implement Dynamic Line Scan Thermography in industrial manufacturing processes.

Bibliography

- [1] G. J. J. Verhoeven and V. Archaeology, "AARGnews," no. November, pp. 10–18, 2018.
- [2] "Infrared thermal imaging in studies of wild animals," 2022.
- [3] H. Glavaš, M. Hadzima-Nyarko, I. H. Buljan, and T. Barić, "Locating hidden elements in walls of cultural heritage buildings by using infrared thermography," *Buildings*, vol. 9, jan 2019.
- [4] P. Botsaris and J. Tsanakas, "Infrared thermography as an estimator technique of a photovoltaic module performance via operating temperature measurements," *Proceedings of the 10th ECNDT Conference*, no. June 2014, pp. 1–11, 2010.
- [5] Pulsar, "THE FIELDS OF APPLICATION OF THERMAL IMAGING TECHNOLOGY — Pulsar."
- [6] A. Kylili, P. A. Fokaides, P. Christou, and S. A. Kalogirou, "Infrared thermography (IRT) applications for building diagnostics: A review," *Applied Energy*, vol. 134, pp. 531–549, dec 2014.
- [7] H. Leicht, M. Heilig, C. Pommer, E. Kraus, and B. Baudrit, "Active and passive thermography for defect detection in polymer joints,"
- [8] J. N. Zalameda and W. P. Winfree, "Passive Thermography Measurement of Damage Depth During Composites Load Testing," *Frontiers in Mechanical Engineering*, vol. 0, p. 19, apr 2021.
- [9] X. Maldague, *Nondestructive Evaluation of Materials by Infrared Thermography - Xavier P.V. Maldague*.
- [10] S. Doshvarpassand, C. Wu, and X. Wang, "An overview of corrosion defect characterization using active infrared thermography," *Infrared Phys. Technol.*, vol. 96, pp. 366–389, jan 2019.
- [11] B. Oswald-Tranta, "Lock-in inductive thermography for surface crack detection in different metals," *Quantitative InfraRed Thermography Journal*, vol. 16, pp. 276–300, oct 2019.
- [12] N. Rajic, "Principal component thermography for flaw contrast enhancement and flaw depth characterisation in composite structures," *Composite Structures*, vol. 58, pp. 521–528, dec 2002.

- [13] Edevis, “Laboratory testing systems for optically excited lock-in-thermography.”
- [14] E. Jasiūnienė, L. Mažeika, V. Samaitis, V. Cicėnas, and D. Mattsson, “Ultrasonic non-destructive testing of complex titanium/carbon fibre composite joints,” *Ultrasonics*, vol. 95, pp. 13–21, may 2019.
- [15] O. Ley and V. Godinez-Azcuaga, “Line Scanning Thermography and its Application Inspecting Aerospace Composites,” tech. rep.
- [16] A. Runnelmalm and A. Appelgren, “SpotLight Punktsvetsning för lättviktskonstruktioner Resistance spot welding for light weight design WP 5 Automated quality checking of spot welds Evaluation of non-destructive testing methods for automatic quality checking of spot welds.”
- [17] Z. W. Yang, H. P. Yan, Y. Li, G. J. Kou, G. Tian, and W. Zhang, “A Novel Inclined Excitation Method for Crack Detection of Non-Ferromagnetic Materials Using Eddy Current Thermography,” *Strength of Materials*, vol. 51, pp. 558–568, jul 2019.
- [18] J. Peeters, G. Van der Snickt, S. Sfarra, S. Legrand, C. Ibarra-Castanedo, K. Janssens, and G. Steenackers, “IR reflectography and active thermography on artworks: The added value of the 1.5-3 μm band,” *Applied Sciences (Switzerland)*, vol. 8, no. 1, pp. 1–19, 2018.
- [19] K. Blessley, C. Young, J. Nunn, J. Coddington, and S. Shepard, “The feasibility of flash thermography for the examination and conservation of works of Art,” *Studies in Conservation*, vol. 55, no. 2, pp. 107–120, 2010.
- [20] M. Zimnoch, W. Olfieruk, and M. Maj, “Estimation of defect depth in steel plate using lock-in IR thermography,” *Acta Mechanica et Automatica*, vol. Vol. 4, no. no. 4, pp. 106–109, 2010.
- [21] M. Hillen, S. Sels, B. Ribbens, S. Verspeek, K. Janssens, G. Van der Snickt, and G. Steenackers, “Qualitative Comparison of Lock-in Thermography (LIT) and Pulse Phase Thermography (PPT) in Mid-Wave and Long-Wave Infrared for the Inspection of Paintings,” *Applied Sciences 2023, Vol. 13, Page 4094*, vol. 13, p. 4094, mar 2023.
- [22] S. Verspeek, I. De Boi, X. Maldague, R. Penne, and G. Steenackers, “Dynamic Line Scan Thermography Parameter Design via Gaussian Process Emulation,” *Algorithms 2022, Vol. 15, Page 102*, vol. 15, p. 102, mar 2022.
- [23] O. S. Amosov, S. G. Amosova, and I. O. Iochkov, “Defects Detection and Recognition in Aviation Riveted Joints by Using Ultrasonic Echo Signals of Non-Destructive Testing,” *IFAC-PapersOnLine*, vol. 54, pp. 484–489, jan 2021.
- [24] J. R. Deepak, V. K. Bupesh Raja, D. Srikanth, H. Surendran, and M. M. Nickolas, “Non-destructive testing (NDT) techniques for low carbon steel welded joints: A review and experimental study,” *Materials Today: Proceedings*, vol. 44, pp. 3732–3737, jan 2021.

- [25] B. J. Rivas S., Servent R., “Automated Spot Weld Inspection In The Automotive Industry,” 2005.
- [26] N. Athi, S. R. Wylie, J. D. Cullen, A. I. Al-Shamma’, and T. Sun, *Ultrasonic non-destructive evaluation for spot welding in the automotive industry; Ultrasonic non-destructive evaluation for spot welding in the automotive industry*. 2009.
- [27] T. G. Santos, P. VilaCca, L. Quintino, J. Dos Santos, and R. M. Miranda, “Application Of Eddy Current Techniques To Inspect Friction Spot Welds In Aluminium Alloy Aa2024 And A Composite Material,” *Welding in the World*, vol. 55, pp. 12–18, sep 2011.
- [28] O. Sherepenko, A. Mohamadizadeh, A. Zvorykina, M. Worswick, E. Biro, and S. Jüttner, “Determination of resistance spot weld failure path in ultra-high-strength press-hardened steel by control of fusion boundary transient softening,” *Journal of Materials Science*, vol. 56, pp. 14287–14297, sep 2021.
- [29] A. Runnemalm, J. Ahlberg, A. Appelgren, S. Sjökvist, A. Runnemalm, J. Ahlberg, A. Appelgren, and S. Sjökvist, “Automatic Inspection of Spot Welds by Thermography,” *J Nondestruct Eval*, vol. 33, pp. 398–406, 2014.
- [30] L. Kastner, S. Ahmadi, F. Jonietz, P. Jung, G. Caire, M. Ziegler, and J. Lambrecht, “Classification of Spot-Welded Joints in Laser Thermography Data Using Convolutional Neural Networks,” *IEEE Access*, vol. 9, pp. 48303–48312, 2021.
- [31] J. Schlichting, S. Brauser, L. A. Pepke, C. Maierhofer, M. Rethmeier, and M. Kreuzbruck, “Thermographic testing of spot welds,” *NDT E International*, vol. 48, pp. 23–29, jun 2012.
- [32] F. Jonietz, P. Myrach, H. Suwala, and M. Ziegler, “Examination of Spot Welded Joints with Active Thermography,” *Journal of Nondestructive Evaluation*, vol. 35, pp. 1–14, mar 2016.
- [33] R. Usamentiaga, C. Ibarra-Castanedo, M. Klein, X. Maldague, J. Peeters, and A. Sanchez-Beato, “Nondestructive Evaluation of Carbon Fiber Bicycle Frames Using Infrared Thermography,” *Sensors 2017, Vol. 17, Page 2679*, vol. 17, p. 2679, nov 2017.
- [34] X. Maldague, F. Galmiche, and A. Ziadi, “Advances in pulsed phase thermography,” *Infrared Physics Technology*, vol. 43, pp. 175–181, jun 2002.
- [35] S. Verspeek, B. Ribbens, X. Maldague, and G. Steenackers, “Optimisation of a Heat Source for Infrared Thermography Measurements: Comparison to Mehler Engineering + Service-Heater,” *Applied Sciences*, vol. 10, p. 1285, feb 2020.
- [36] Xavier P. Maldague, *Theory and practice of infrared thermography for non-destructive testing*. New York: Wiley, 2001.

- [37] F. Ciampa, P. Mahmoodi, F. Pinto, and M. Meo, "Recent Advances in Active Infrared Thermography for Non-Destructive Testing of Aerospace Components," *Sensors*, vol. 18, p. 609, feb 2018.
- [38] J. Chen, L. Yang, Z. Zhang, J. Wei, and J. Yang, "Optimization of a uniform solar concentrator with absorbers of different shapes," *Solar Energy*, vol. 158, pp. 396–406, dec 2017.
- [39] R. Oommen and S. Jayaraman, "Development and performance analysis of compound parabolic solar concentrators with reduced gap losses—'V' groove reflector," *Renewable Energy*, vol. 27, pp. 259–275, oct 2002.
- [40] M. Tian, Y. Su, H. Zheng, G. Pei, G. Li, and S. Riffat, "A review on the recent research progress in the compound parabolic concentrator (CPC) for solar energy applications," *Renewable and Sustainable Energy Reviews*, vol. 82, pp. 1272–1296, feb 2018.
- [41] E.-H. Lee, D.-Y. Yang, and W.-H. Yang, "Numerical modeling and experimental validation of focused surface heating using near-infrared rays with an elliptical reflector," *International Journal of Heat and Mass Transfer*, vol. 78, pp. 240–250, nov 2014.
- [42] E.-H. Lee, J.-S. Hwang, C.-W. Lee, D.-Y. Yang, and W.-H. Yang, "A local heating method by near-infrared rays for forming of non-quenchable advanced high-strength steels," *Journal of Materials Processing Technology*, vol. 214, pp. 784–793, apr 2014.
- [43] B A Unvala and A Maries, "Radiant heating using an ellipsoidal reflector," *J. Phys. E: Sci. Instrum. Z. Phys. Chem. in the press Cady W G Piezoelectricity J. Appl. Phys. Miller J G and Bolef D I J. Appl. Phys. Phys. Journal of Physics E: Scientific Instruments*, vol. 7, no. 7, pp. 4385–90, 1974.
- [44] Mehler Engineering Service, "Industrial Infrared Line Heater."
- [45] R. Rashed and Roshdi Rashed, "A Pioneer in Anaclastics: Ibn Sahl on Burning Mirrors and Lenses," *Isis*, vol. 81, pp. 464–491, sep 1990.
- [46] F. Holland, "The Reflective Property of a Parabola," *Irish Math. Soc. Bulletin*, vol. 66, pp. 87–90, 2010.
- [47] R. C. Williams, E. By, J. P. Hutchinson, and S. Wagon, "A Proof of the Reflective Property of the Parabola," *Source: The American Mathematical Monthly*, vol. 94, no. 7, pp. 667–668, 1987.
- [48] S. A. Waghmare and N. P. Gulhane, "Design and ray tracing of a compound parabolic collector with tubular receiver," *Solar Energy*, vol. 137, pp. 165–172, nov 2016.
- [49] S. Berendonk, "Proving the Reflective Property of an Ellipse," *Source: Mathematics Magazine*, vol. 87, no. 4, pp. 276–279, 2014.
- [50] ResearchInc, "Radiant Infrared Line Heater."

- [51] S. Verspeek, J. Gladines, B. Ribbens, X. Maldague, and G. Steenackers, "Dynamic Line Scan Thermography Optimisation Using Response Surfaces Implemented on PVC Flat Bottom Hole Plates," *Applied Sciences*, vol. 11, p. 1538, feb 2021.
- [52] P. J. Lindberg, "A Prism Line-scanner for High-speed Thermography," *Optica Acta: International Journal of Optics*, vol. 15, pp. 305–316, jul 1968.
- [53] C. Ibarra-Castanedo, P. Servais, A. Ziadi, M. Klein, and X. Maldague, "RITA - Robotized Inspection by Thermography and Advanced processing for the inspection of aeronautical components," QIRT Council, 2014.
- [54] J. Peeters, C. Ibarra-Castanedo, F. Khodayar, Y. Mokhtari, S. Sfarra, H. Zhang, X. Maldague, J. J. Dirckx, and G. Steenackers, "Optimised dynamic line scan thermographic detection of CFRP inserts using FE updating and POD analysis," *NDT and E International*, vol. 93, pp. 141–149, jan 2018.
- [55] Zhang, Sfarra, Ibarra-Castanedo, and Maldague, "Dynamic Line-Scan Thermography for the Inspection of Paper-Based Materials: A Case Study Focused on an Ancient Book Cover," *Proceedings*, vol. 27, no. 1, p. 9, 2019.
- [56] G. Steenackers, F. Presezniak, and P. Guillaume, "Development of an adaptive response surface method for optimization of computation-intensive models," *Computers Industrial Engineering*, vol. 57, pp. 847–855, oct 2009.
- [57] S. Genna, F. Tagliaferri, I. Papa, C. Leone, and B. Palumbo, "Multi-response optimization of CFRP laser milling process based on response surface methodology," *Polymer Engineering Science*, vol. 57, pp. 595–605, jun 2017.
- [58] R. H. A.-C. Myers, *Response Surface Methodology : Process and Product Optimization Using Designed Experiments*. Wiley, 2016.
- [59] M. Ghanbarian, M. Ghanbarian, A. H. Mahvi, and T. Tabatabaie, "Enhanced fluoride removal over MgFe₂O₄-chitosan-CaAl nanohybrid: Response surface optimization, kinetic and isotherm study," *International Journal of Biological Macromolecules*, vol. 148, pp. 574–590, apr 2020.
- [60] C. M. Teglia, M. Guíñez, H. C. Goicoechea, M. J. Culzoni, and S. Cerutti, "Enhancement of multianalyte mass spectrometry detection through response surface optimization by least squares and artificial neural network modelling," *Journal of Chromatography A*, vol. 1611, p. 460613, jan 2020.
- [61] B. Davoodi and B. Eskandari, "Tool wear mechanisms and multi-response optimization of tool life and volume of material removed in turning of N-155 iron-nickel-base superalloy using RSM," *Measurement: Journal of the International Measurement Confederation*, vol. 68, pp. 286–294, may 2015.
- [62] Y. Liu, J. Zhou, W. Fu, B. Zhang, F. Chang, and P. Jiang, "Study on the effect of cutting parameters on bamboo surface quality using response surface methodology," *Measurement*, vol. 174, p. 109002, jan 2021.

- [63] H. Alrweili, S. Georgiou, and S. Stylianou, "A New Class of Second-Order Response Surface Designs," *IEEE Access*, vol. 8, pp. 115123–115132, 2020.
- [64] C. Areas, "MES thermosol® lineIR CP / CF Infrared Line Radiators for Heating Special Edge, Bend and Connection Areas."
- [65] J. Bauer, M. N. Hoq, J. Mulcahy, S. A. Tofail, F. Gulshan, C. Silien, H. Podbielska, and M. M. Akbar, "Implementation of artificial intelligence and non-contact infrared thermography for prediction and personalized automatic identification of different stages of cellulite," *EPMA Journal*, vol. 11, pp. 17–29, mar 2020.
- [66] M. A. S. A. Husaini, M. H. Habaebi, S. A. Hameed, M. R. Islam, and T. S. Gunawan, "A Systematic Review of Breast Cancer Detection Using Thermography and Neural Networks," 2020.
- [67] S. T. Kakileti, H. J. Madhu, G. Manjunath, L. Wee, A. Dekker, and S. Sampangi, "Personalized risk prediction for breast cancer pre-screening using artificial intelligence and thermal radiomics," *Artificial Intelligence in Medicine*, vol. 105, p. 101854, may 2020.
- [68] J. Zuluaga-Gomez, Z. Al Masry, K. Benagoune, S. Meraghni, and N. Zerhouni, "A CNN-based methodology for breast cancer diagnosis using thermal images," oct 2019.
- [69] B. J. Papež, M. Palfy, M. Mertik, Turk, and Z, "Infrared Thermography Based on Artificial Intelligence as a Screening Method for Carpal Tunnel Syndrome Diagnosis," tech. rep., 2009.
- [70] G. M. dos Santos, R. R. de Aquino, and M. M. Lira, "Thermography and artificial intelligence in transformer fault detection," *Electrical Engineering*, vol. 100, pp. 1317–1325, sep 2018.
- [71] T. Sato and M. Fujita, "A Data-Driven Automatic Design Method for Electric Machines Based on Reinforcement Learning and Evolutionary Optimization," *IEEE Access*, vol. 9, pp. 71284–71294, may 2021.
- [72] H. Zhang, P. Verberne, S. A. Meguid, C. Ibarra-Castanedo, and X. P. Maldague, "Autonomous high resolution inspection of kiss-bonds skins of carbon nanotube reinforced nanocomposites using novel dynamic line-scan thermography approach," *Composites Science and Technology*, vol. 192, p. 108111, may 2020.
- [73] G. Pei and D. Rim, "Quality control of computational fluid dynamics (CFD) model of ozone reaction with human surface: Effects of mesh size and turbulence model," *Building and Environment*, vol. 189, p. 107513, feb 2021.
- [74] J. Peeters, S. Verspeek, S. Sels, B. Bogaerts, and G. Steenackers, "Optimised dynamic line scanning thermography for aircraft structures," in *14TH QUANTITATIVE INFRARED THERMOGRAPHY CONFERENCE*, Quantitative Infrared Thermography, pp. 687–695, Fed Inst Mat Res Testing; German Soc Non Destruct Testing, 2018.

- [75] H. I. Ringermacher, D. L. Mayton, and D. R. Howard, "Towards a flat-bottom hole standard for thermal imaging," *Review of Progress in Quantitative Non-destructive Evaluation*, vol. 17, pp. 425–429, 1998.
- [76] M. Frendberg Beemer and S. Shepard, "Aspect Ratio Considerations for Flat Bottom Hole Defects in Active Thermography," *Quantitative InfraRed Thermography Conference*, no. January 2016, 2016.
- [77] A. Paleyes, M. Pullin, M. Mahsereci, C. McCollum, N. D. Lawrence, and J. Gonzalez, "Emulation of physical processes with emukit," *arXiv preprint arXiv:2110.13293*, 2021.
- [78] C. E. Rasmussen and C. K. I. Williams, *Gaussian processes for machine learning*, vol. 38. 2006.
- [79] T. K. Ho, "Random decision forests," *Proceedings of the International Conference on Document Analysis and Recognition, ICDAR*, vol. 1, pp. 278–282, 1995.
- [80] T. Lim and K. Wang, "Comparison of machine learning algorithms for emulation of a gridded hydrological model given spatially explicit inputs," *Computers Geosciences*, vol. 159, p. 105025, feb 2022.
- [81] U. Noè, A. Lazarus, H. Gao, V. Davies, B. MacDonald, K. Mangion, C. Berry, X. Luo, and D. Husmeier, "Gaussian process emulation to accelerate parameter estimation in a mechanical model of the left ventricle: a critical step towards clinical end-user relevance," *Journal of the Royal Society Interface*, vol. 16, no. 156, 2019.
- [82] T. Pan, Y. Cai, and S. Chen, "Development of an Engine Calibration Model Using Gaussian Process Regression," *International Journal of Automotive Technology 2021 22:2*, vol. 22, pp. 327–334, mar 2021.
- [83] D. C. Liu and J. Nocedal, "On the limited memory BFGS method for large scale optimization," *Mathematical programming*, vol. 45, no. 1, pp. 503–528, 1989.
- [84] D. Kristjanson Duvenaud and P. College, "Automatic Model Construction with Gaussian Processes Declaration," 2014.
- [85] K.-T. Fang, R. Li, and A. Sudjianto, *Design and modeling for computer experiments*. Chapman and Hall/CRC, 2005.
- [86] D. R. Jones, M. Schonlau, and W. J. Welch, "Efficient Global Optimization of Expensive Black-Box Functions," *Journal of Global Optimization*, vol. 13, no. 4, pp. 455–492, 1998.
- [87] J. Sacks, W. J. Welch, T. J. Mitchell, and H. P. Wynn, "Design and Analysis of Computer Experiments," <https://doi.org/10.1214/ss/1177012413>, vol. 4, pp. 409–423, nov 1989.

- [88] M. Buisson-Fenet, F. Solowjow, and S. Trimpe, “Actively learning gaussian process dynamics,” in *Learning for dynamics and control*, pp. 5–15, PMLR, 2020.
- [89] E. Pasolli and F. Melgani, “Gaussian process regression within an active learning scheme,” in *2011 IEEE International Geoscience and Remote Sensing Symposium*, pp. 3574–3577, 2011.
- [90] A. Gessner, J. Gonzalez, and M. Mahsereci, “Active multi-information source Bayesian quadrature,” in *Uncertainty in Artificial Intelligence*, pp. 712–721, PMLR, 2020.
- [91] S. Oladyszhkin, F. Mohammadi, I. Kroeker, and W. Nowak, “Bayesian3 Active Learning for the Gaussian Process Emulator Using Information Theory,” *Entropy 2020*, Vol. 22, Page 890, vol. 22, p. 890, aug 2020.
- [92] L. P. Swiler, M. Gulian, A. L. Frankel, C. Safta, and J. D. Jakeman, “A survey of constrained Gaussian process regression: Approaches and implementation challenges,” *Journal of Machine Learning for Modeling and Computing*, vol. 1, no. 2, pp. 119–156, 2020.
- [93] D. J. Eisenmann, D. Enyart, C. Lo, and L. Brasche, “Review of progress in magnetic particle inspection,” *AIP Conference Proceedings*, vol. 1581 33, pp. 1505–1510, 2014.
- [94] N. P. Avdelidis and T. H. Gan, “Non-destructive evaluation (NDE) of Composites: Infrared (IR) thermography of wind turbine blades,” *Non-Destructive Eval. Polym. Matrix Compos. Tech. Appl.*, pp. 634–648, 2013.
- [95] W. Nsengiyumva, S. Zhong, J. Lin, Q. Zhang, J. Zhong, and Y. Huang, “Advances, limitations and prospects of nondestructive testing and evaluation of thick composites and sandwich structures: A state-of-the-art review,” *COMPOSITE STRUCTURES*, vol. 256, jan 2021.
- [96] F. Khodayar, S. Sojasi, and X. Maldague, “Infrared thermography and NDT: 2050 horizon,” *QUANTITATIVE INFRARED THERMOGRAPHY JOURNAL*, vol. 13, pp. 210–231, dec 2016.
- [97] F. E. F. Thiessen, T. Tondu, B. Cloostermans, Y. A. L. Dirkx, D. Auman, S. Cox, V. Verhoeven, G. Hubens, G. Steenackers, and W. A. A. Tjalma, “Dynamic InfraRed Thermography (DIRT) in DIEP-flap breast reconstruction: A review of the literature,” *European Journal of Obstetrics Gynecology and Reproductive Biology*, vol. 242, pp. 47–55, 2019.
- [98] M. Hillen, S. Legrand, Y. Dirkx, K. Janssens, G. Van der Snickt, J. Caen, and G. Steenackers, “Cluster Analysis of IR Thermography Data for Differentiating Glass Types in Historical Leaded-Glass Windows,” *Appl. Sci. 2020*, Vol. 10, Page 4255, vol. 10, p. 4255, jun 2020.
- [99] B. Lu, P. D. Dao, J. Liu, Y. He, and J. Shang, “Recent Advances of Hyperspectral Imaging Technology and Applications in Agriculture,” *REMOTE SENSING*, vol. 12, aug 2020.

- [100] T. Adao, J. Hruska, L. Padua, J. Bessa, E. Peres, R. Morais, and J. J. Sousa, "Hyperspectral Imaging: A Review on UAV-Based Sensors, Data Processing and Applications for Agriculture and Forestry," *REMOTE SENSING*, vol. 9, nov 2017.
- [101] G. J. Edelman, E. Gaston, T. G. van Leeuwen, P. J. Cullen, and M. C. G. Aalders, "Hyperspectral imaging for non-contact analysis of forensic traces," *Forensic Science International*, vol. 223, no. 1, pp. 28–39, 2012.
- [102] J. Kuula, I. Plnen, H.-H. Puupponen, T. Selander, T. Reinikainen, T. Kalenius, and H. Saari, "Using VIS/NIR and IR spectral cameras for detecting and separating crime scene details," in *Sensors, and Command, Control, Communications, and Intelligence (C3I) Technologies for Homeland Security and Homeland Defense XI* (E. M. Carapezza, ed.), vol. 8359, pp. 150–160, International Society for Optics and Photonics, SPIE, 2012.
- [103] S. Wilczynski, R. Koprowski, M. Marmion, P. Duda, and B. Blonska-Fajfrowska, "The use of hyperspectral imaging in the VNIR (4001000nm) and SWIR range (10002500nm) for detecting counterfeit drugs with identical API composition," *Talanta*, vol. 160, pp. 1–8, 2016.
- [104] J. Wang, E. Krieger, L. Zbur, J. Gilligan, R. Beideman, J. Beckstead, O. Klueva, M. Conner, E. Maney, and P. Treado, "Sprayed or Soaked Concealed Drug Detection using SWIR Hyperspectral Imaging," in *ALGORITHMS, TECHNOLOGIES, AND APPLICATIONS FOR MULTISPECTRAL AND HYPERSPECTRAL IMAGERY XXVI* (VelezReyes, M and Messinger, DW, ed.), vol. 11392 of *Proceedings of SPIE*, SPIE, 2020.
- [105] Y. Yan, J. Ren, S. Member, H. Zhao, J. F. C. Windmill, W. Ijomah, J. D. Wit, J. V. Freeden, and N. S. Centre, "Non-destructive Testing of Composite Fibre Materials with Hyperspectral Imaging Evaluative Studies in the EU H2020 FibreEUUse Project,"
- [106] T. De Kerf, G. Pipintakos, Z. Zahiri, S. Vanlanduit, and P. Scheunders, "Identification of Corrosion Minerals Using Shortwave Infrared Hyperspectral Imaging," *Sensors*, vol. 22, no. 1, 2022.
- [107] F. D. van der Meer, H. M. A. van der Werff, F. J. A. van Ruitenbeek, C. A. Hecker, W. H. Bakker, M. F. Noomen, M. van der Meijde, E. J. M. Carranza, J. B. de Smeth, and T. Woldai, "Multi- and hyperspectral geologic remote sensing: A review," *INTERNATIONAL JOURNAL OF APPLIED EARTH OBSERVATION AND GEOINFORMATION*, vol. 14, pp. 112–128, feb 2012.
- [108] B. Geelen, N. Tack, and A. Lambrechts, "A compact snapshot multispectral imager with a monolithically integrated per-pixel filter mosaic," in *Advanced Fabrication Technologies for Micro/Nano Optics and Photonics VII* (G. von Freymann, W. V. Schoenfeld, and R. C. Rumpf, eds.), vol. 8974, pp. 80–87, International Society for Optics and Photonics, SPIE, 2014.

- [109] N. Tack, A. Lambrechts, P. Soussan, and L. Haspeslagh, "A compact, high-speed, and low-cost hyperspectral imager," in *Silicon Photonics VII* (J. Kubby and G. T. Reed, eds.), vol. 8266, pp. 126–138, International Society for Optics and Photonics, SPIE, 2012.
- [110] N. Ben Yosef, J. Almog, A. Frank, E. Springer, and A. A. Cantu, "Short UV luminescence for forensic applications: Design of a real-time observation system for detection of latent fingerprints and body fluids," *JOURNAL OF FORENSIC SCIENCES*, vol. 43, no. 2, pp. 299–304, 1998.
- [111] D. De Angelis, G. Mapelli, F. L. Mazzullo, M. T. Lorenz, and C. Cattaneo, "Possible applications of reflected UV photography in forensic odontology: Food for thought," *LEGAL MEDICINE*, vol. 42, feb 2020.
- [112] S. Sfarra, C. Ibarra-Castanedo, D. Ambrosini, D. Paoletti, A. Bendada, and X. Maldague, "Discovering the Defects in Paintings Using Non-destructive Testing (NDT) Techniques and Passing Through Measurements of Deformation," *JOURNAL OF NONDESTRUCTIVE EVALUATION*, vol. 33, pp. 358–383, sep 2014.
- [113] G. C. Nisulescu, I. Ionel, B. Malan, and M. Dobrin, "Remote SO₂ Monitoring with UV Cameras for Stack Emissions," *REVISTA DE CHIMIE*, vol. 63, pp. 940–944, sep 2012.
- [114] S. E. Cantor, "Non-destructive inspection of coatings based on enhanced fluorescent response," *Metal Finishing*, vol. 107, no. 4, pp. 58–61, 2009.
- [115] Z. Zhong, L. Zhao, and L. Wang, "Investigation of light scattering for scratch detection," *Proc SPIE*, vol. 7155, 2008.
- [116] F. Khodayar, F. Lopez, C. Ibarra-Castanedo, and X. Maldague, "Optimization of the Inspection of Large Composite Materials Using Robotized Line Scan Thermography," *Journal of Nondestructive Evaluation*, vol. 36, no. 2, pp. 1–15, 2017.
- [117] A. Geiger, F. Moosmann, O. Car, and B. Schuster, "Automatic Calibration of Range and Camera Sensors using a single Shot," in *International Conference on Robotics and Automation (ICRA)*, 2012.
- [118] J. Peeters, *Optimised failure detection and advanced Non-destructive inspection using active IR thermography and numerical modelling*. 2017.

Active thermography is a non-destructive inspection technique which is praised for its fast, reliable and non-contact manner of working. The technique is being utilized more and more in a variety of domains such as industrial applications, art inspections, during medical interventions, etc. The inspection principle is based on the infrared radiation emitted by every object above absolute zero. A thermal wave is induced in the sample to be inspected and afterwards the heat dissipation is recorded. Commonly the technique is performed in a static manner in which the heating source, sample and thermal camera remain stationary during the measurement. However this limits the dimensions of the sample since it must fit in the field of view of the thermal camera. Hail can be found in performing Dynamic Line Scan Thermography to remove this restriction. Dynamic Line Scan Thermography is a way of performing pulse thermography where the sample moves relatively to a heating source - thermal camera tandem.

Dynamic Line Scan Thermography is depending on multiple measurement parameters and therefore until now an expert skilled in the art had to prescribe the best parameter set or the parameters had to be found using trial and error. This doctoral thesis provides several techniques to enable a layman to optimize the needed measurement parameters based on the application. This optimization is performed in three methods, firstly based on the premise of detecting a specific hole, secondly to find all defects in the least amount of inspections and thirdly to minimise the needed input data and to answer industrial relevant questions. A novel processing algorithm for Dynamic Line Scan Thermography is proposed and prior to optimizing the measurement parameters, an optimization of the line heating source is performed in order to exploit the heating power as efficient as possible.

This doctoral dissertation enables the use of Dynamic Line Scan Thermography in a more accessible manner in industrial and scientific inspections. An insight in the working principle and correlation between the different parameters is provided.